# Hemodynamic Response Function Modeling

Wenjie Chen

A dissertation submitted to the faculty of the University of North Carolina at Chapel Hill in partial fulfillment of the requirements for the degree of Doctor of Philosophy in the Department of Statistics and Operations Research (Statistics).

Chapel Hill
2012

Approved by:

Young K. Truong

Haipeng Shen

J. S. Marron

Aysenil Belger

Sreekalyani Shankar Bhamidi

# Abstract

WENJIE CHEN: Hemodynamic Response Function Modeling.
(Under the direction of Young K. Truong and Haipeng Shen.)

*Functional Magnetic Resonance Imaging* (fMRI) is a medical-imaging technique for studying brain function. It can be used to capture the response of the brain to various tasks. The response to a brief, intense period of neural stimulation is called the *hemodynamic response function* (HRF). Modeling HRF is essential to identifying the brain activation by exploring the relationship between the experimental stimulus and the response.

In this dissertation, we discuss three research problems related to HRF estimation. First, when multiple types of stimuli are present, how can we capture the characteristic HRF for each stimulus? Second, is there any difference among the HRFs corresponding to multiple stimuli? Third, how can we improve the HRF estimator's efficiency?

We propose a nonparametric method, *transfer function estimate* (TFE), to answer these three questions. Building on existing work, we extend the nonparametric approach to a multivariate form, which adapts to the multiple types of stimuli, and we develop hypothesis testing to identify the brain activation and to compare the HRFs under different stimuli. In order to improve estimation efficiency, we propose using *weighted least square* (WLS) in a multiple system of regression by spectral methods.

The finite-sample performance of the TFE is illustrated through several simulation studies and real fRMI data sets. We also establish the asymptotic normality of the TFE, as well as the efficiency of the WLS estimator.

# Acknowledgments

I would like to pay tribute to my advisors, Drs. Shen and Truong, for their enthusiasm, vision, and immense knowledge. I treasure their guidance in the past five years of my Ph.D. study and research.

I would like to thank as well my other committee members: Dr. Belger, Dr. Bhamidi, and Dr. Marron for their support and helpful comments.

Dr. Huang created an invaluable research environment. Her encouragement, passion, and advice motivated me to better myself and my work.

I wish to thank Mechelle and Suman for the consistent support they gave me during the years. Their kindness, patience, and help in the lab bolstered my research and warmed my heart.

I thank Dr. Belger and Joshua for the chance to work with them, and for the scientific and psychiatric interpretations they provided.

My memory of fMRI is with Seonjoo. And the computation platform would have been a hard bump without Gu.

To my collaborators, families and friends, thanks for fulfilling my life at Chapel Hill.

# Contents

# List of Figures

# List of Abbreviations

| | |
|---|---|
| **AFNI** | Analysis of Functional NeroImages |
| **BOLD** | Blood Oxygenation Level Dependent |
| **FIR** | Finite Impulse Response |
| **fMRI** | functional Magnetic Resonance Imaging |
| **FSL** | FMRIB Software Library |
| **GLM** | General Linear Model |
| **HRF** | Hemodynamic Response Function |
| **ITI** | Inter-trial Interval |
| **MCMC** | Markov chain Monte Carlo |
| **MCV** | Modified Cross Validation |
| **MR** | Magnetic Resonance |
| **OLS** | Ordinary Least Square |
| **RMSE** | Root Mean Squared Error |
| **ROI** | Region of Interest |
| **SPM** | Statistical Parametric Mapping |
| **SVD** | Singular Value Decomposition |
| **TFE** | Transfer Function Estimate |
| **WLS** | Weighted Least Square |

# Chapter 1

# Introduction

A brief background of *functional Magnetic Resonance Imaging* (fMRI) and the modeling of *hemodynamic response function* (HRF) will be described along with our research projects. Section 1.1 introduces a powerful tool, fMRI, widely used in neuromedical imaging studies. Two categories are suggested in Section 1.2 for classifying the experimental designs in terms of stimulus presentation. Section 1.3 describes HRF in fMRI and its application under two types of experimental designs. Section 1.4 gives motivation and discusses the contribution of our research in HRF modeling.

## 1.1 Functional Magnetic Resonance Imaging

While studying the human brain 200 years ago, phrenologists introduced the idea of *localization of function*: the brain may have distinct regions that support particular mental processes, that is, different aspects of the human mind may be represented in different brain regions (Huettel, Song, and McCarthy, 2004). This localization idea inspires modern-day explorers to map the human brain by localizing different mental processes to different parts of the brain; one popular analysis tool is fMRI, which is used to take images of the active brain in both clinical and research settings.

Functional neuroimaging studies are necessary to understand how the human brain works. The MRI has been a powerful clinical tool in the study of the brain's structure;

moreover, it can also reveal short-term physiological changes associated with the active functions of the brain. FMRI is a leading technique in creating the maps of human brain function by using standard *magnetic resonance* (MR) scanners.

Functional MRI is a measure of metabolic activity, instead of neural activity. It is well established that energy metabolism and neural activity are tightly coupled. The activity of neuron requires energy from the metabolism which is provided sufficiently by blood flow in the brain. A small neuronal activity could cause a large increase in local energy demand. The energy comes from the consumption of glucose and oxygen in the blood. The oxygen is attached to hemoglobin molecules. The *oxygenated hemoglobin* (Hb) and *deoxygenated hemoglobin* (dHb) have different magnetic properties in MR scanner. There are more MR signal when Hb is at a high level and less MR signal when dHb is at a high level. The changes of the dHb level can be captured in a strong static magnetic field from MR scanner.

FMRI is able to measure the signal of the delivery of oxygen and glucose to active neurons. The *blood-oxygen-level dependent* (BOLD) signal from the MR scanner has been shown to be closely linked to neural activity. Through a process called the *hemodynamic response*, blood releases oxygen to active neurons at a greater rate than to inactive ones. Most fMRI studies measure changes in blood oxygenation over time. Because blood oxygen levels change rapidly following the activity of neurons in a brain region, fMRI allows researchers to localize brain activity on a second-by-second basis and within millimeters of its origin. The brain activity is mapped onto a structural brain image highlighting the activation regions, called *brain mapping*. The spatial resolution of the cubic-millimeter-volume units (the basic three-dimension sampling units are known as *voxels*) forms the brain mapping; the temporal resolution of seconds improves the precision of the hemodynamic response study.

Most current fMRI studies model the BOLD signal in a voxelwise fashion, that

is, with respect to a volume unit voxel, data in the form of time series are analyzed in a proper model to obtain the brain mapping. The time series data, which we will denote later as $\{Y(t); t = 0, \ldots, T-1\}$, come from one voxel; as the brain is composed of millions of voxels, for the whole brain, millions of time series can be detected in the MR scanner during the experiment. The experimental stimuli $\{s(t); t = 0, \ldots, T-1\}$ will be designed in a particular way for the MR scanner to detect the corresponding changes in the brain. When the stimulus is present, $s(t)$ is 1; otherwise, it is 0.

A typical neuropsychological test in fMRI is the finger-tapping experiment: the participant is signaled to perform finger tapping in the MR scanner according to the experimental paradigm $\{s(0), \ldots, s(T-1)\}$, and at each voxel, the fMRI data $Y(t)$ is recorded during both finger-tapping $\{t : s(t) = 1\}$ and rest $\{t : s(t) = 0\}$ periods. The signal received by the subject is the *stimulus*. In one voxel from the brain, we can start the analysis from the two series: the fMRI data $Y(t)$ and its known stimulus function $s(t)$. The relationship between $Y(t)$ and $s(t)$ is used for detecting whether the voxel is responsive to the stimulus or not.

The experimenters are interested in detecting the brain regions activated by the stimulus, as well as understanding the mechanism by which the brain responds to the stimulus.

## 1.2 Experimental Design

In this section, we discuss the stimulus function $s(t)$ from two typical experimental designs for fMRI.

There are two basic types of fMRI studies: *event-related design* and *block design*. An event-related design presents discrete, short-duration stimuli, called *event*, whose timing and order may be randomized. For instance, the event can be designed as a scary picture, a short sound, a gesture, etc. Figure 1.1a offers a graphic illustration

of one event-related design, where the locations of the peaks correspond to the event times. A block design separates experimental conditions into distinct blocks, and each experimental condition is presented for an extended period of time. For example, see Figure 1.1b, where each block corresponds to the duration of the experiment stimulus.


(a) Event-Related Design


(b) Block Design

Figure 1.1: Two major types of experimental designs. (a) illustrates a random event-related design. Each vertical line over time represents one event (a single stimulus). (b) illustrates a block design. Each block represents a period of stimulus presentation. There is a certain amount of resting periods between them.

For a simple example, there is only one kind of stimulus in the experiment. Figure 1.1a and 1.1b can be regarded as an illustration of the time series of the stimulus function $\{s(t) : t = 1, \ldots, T\}$, where $s(t)$ equals 1 for stimulus presentation and 0 for resting.

In practice, one experimental design may contain more than one type of stimuli. The multiple stimuli in an experimental design are of more benefit to design efficiency than a single stimulus repetition. First, if the subjects get used to the repetition of the single stimulus, their responses may fade in several minutes. Second, the multiple-stimulus design makes comparison among the types of stimuli much easier. Thus researchers often put more than one type of stimulus in one scanning session of fMRI.

In a multiple-stimulus experimental design, we pay attention to both the effects of a single stimulus and the comparison among the stimuli. Note that there are more than one type of stimulus functions in the multiple-stimulus experimental design.

Thus, the relationship between the multiple stimulus functions and the fMRI response is much more complicated than in the simple one-stimulus design.

## 1.3 Hemodynamic Response Function and Its Application

The change in the MR signal triggered by neural activity is known as the *hemodynamic response*. The relationship between the stimulus $s(t)$ and the BOLD signal $Y(t)$ involves hemodynamic response function (HRF). Estimating or determining the HRF is important for the correct interpretation of neurological studies.

The HRF is the response to a brief, intense period of neural stimulation. The shape of the HRF varies according to the properties of the stimulus and, presumably, the underlying neuronal activity. The components of the typical HRF include a peak and a post-dip (undershoot) as shown in Figure 1.2. The peak is the maximum amplitude of the HRF, occurring typically about 4 to 6 seconds following a short-duration event. The undershoot is the decrease in MR signal amplitude below baseline due to the combination of reduced blood flow and increased blood volume.

Hemodynamic response varies from region to region in the brain and from subject to subject during the same experiment. Increasing the rate of neural firing increases HRF amplitude, whereas increasing the duration of neural activity increases HRF width (latency).

### 1.3.1 HRF

As hemodynamic response is the MR signal evoked by a short, single stimulus, it results from three factors during the neutral and metabolic activity: oxygen consumption, blood flow, and blood volume. It has three major components: initial dip,

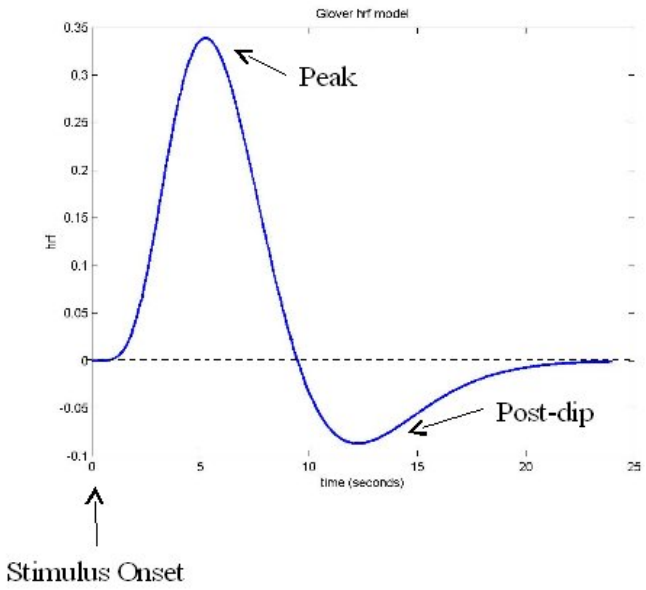


Figure 1.2: This is a typical HRF as double gamma functions, called Glover's HRF (Glover, 1999). It is composed by the peak and the post-dip indicated in the plot. Its $x$-axis refers to time, and its $y$-axis refers to the intensity of HRF. Usually a HRF lasts 20 to 30 seconds.

peak and undershoot.

### Initial Dip

At the first 1 to 2 seconds after stimulus, an initial dip is reported by many studies. While neuronal activities start in a neuron region, the transient energy demand is satisfied by the oxygen extraction in local Hb. This results an increase of dHb, and therefore the decrease of MR signal, called initial dip.

### Peak

After a short latency of initial dip, the blood flow come in with increasing blood volume. The blood flow brings more oxygen than its needs in the neuron region, which results the decrease of dHb and the increase of MR signal. The increase keeps about 5 seconds to reach a maximum value in MR signal, called peak.

**Undershoot**

After the peak, the blood flow decreased more rapidly than the blood volume to the baseline. During the period that the blood flow returns to baseline and the blood volume is still above the baseline, a greater amount of dHb is present, and therefore the MR signal is below the baseline for a prolonged period, called undershoot.

The typical shape of HRF contains an initial dip, a rise to peak, a fall to baseline, and a prolonged post-stimulus undershoot. As the initial dip lasts only 1 to 2 seconds, it may not be detected without finer temporal resolution of MR signal. Different persons may have different HRF shapes including the timings of rise and fall, the amplitude of the peak, and the HRF latency. However, the connection from neuronal activity to energy metabolism is about the same. BOLD signal is regarded as a detector of the neural activity and the functions of the brain.

### 1.3.2 Application

A single stimulus can evoke a hemodynamic response in the brain that spans a 20-second or greater latency. For each trial, the duration of the BOLD response matches well with the subject's response time (Richter, Ugurbil, Georgopoulos, and Kim, 1997). The shape and intensity of the hemodynamic response varies across brain regions and across individuals. Thus, when investigating the activity using fMRI, we must consider its spatial and temporal properties.

The HRF typically is closely linked to the event-related stimulus in fMRI, because the design paradigm allows the HRF to return to baseline or to recover after every trial. By characterizing the precise timing and waveform of the hemodynamic response, researchers can make inferences about the relative timing of neuronal activity, neuronal feedback processes, and sustained activity within a brain region.

The HRF modeling is usually carried out under the event-related design. It has

been demonstrated that the areas of BOLD activity can be detected using even very short-duration stimuli and interstimulus intervals. In event-related designs, stimuli that generate short bursts of neural activity are known as *events* or *trials*. The different conditions are usually presented in random order rather than an alternating pattern. Event-related studies measure transient changes in brain activity associated with discrete stimuli. The pattern of changes over time becomes critical for experimental analysis. The characteristics of the event-related designs make the precise estimation of the timing and the waveform of a given HRF achievable. On the other hand, block designs are good for detecting brain activation regions, but are not widely used in estimating the HRF. Most existing HRF estimators have been developed under event-related design. We propose a procedure for estimating the HRF that works under both event-related and block designs.

A basic assumption for estimating HRF is *linearity*. In the event-related design, we consider the hemodynamic response to be evoked by a single, isolated stimulus; in the block design, the stimuli are presented in succession, and it is possible to assume that the same HRF is evoked for every stimulus, independently of the other stimuli presented. If the stimuli are sufficiently close together so that their hemodynamic responses overlap, then the measured total change in MRI signal will be the sum of the individual processes, known as a *linear system* (Boynton, Engel, Glover, and Heeger, 1996; Friston, Worsley, Frackowiak, Mazziotta, and Evans, 1993).

Modeling the HRF is essential to exploring the relationship between the experimental stimulus and the fMRI signal. If an estimated HRF does not accurately reflect the way the brain responds to stimulus, any follow-up statistical inference will unlikely be valid.

## 1.4 Overview

Estimating HRF is our initial inspiration for improving fMRI analysis. In the process of building up the theorems and the methodology for HRF, we developed several ways to generate function maps. As the final goal of fMRI study is to give human brain mapping, the methodology we present in this dissertation is an analyzing system about dealing with fMRI data based on HRF estimation.

In our work, we investigate frequency domain approaches for estimating the HRF in fMRI. We first extend the approach of Bai, Huang, and Truong (2009) from event-related designs to block designs. Then we improve estimation efficiency. For the application purpose, we also develop an estimation approach that can incorporate multiple stimuli in one experimental design. A hypothesis-testing procedure is developed to identify the voxels activated by a certain stimulus and to compare the effects from different stimuli. In the following chapters, we illustrate the performance of our estimators and the testing procedure using simulation studies and real fMRI applications. Finally, we prove the sampling properties of the HRF estimation: consistency and efficiency.

The rest of the dissertation is structured as follows. Chapter 2 reviews the existing estimators for the HRF. Chapter 3 presents our methodology. Chapter 4 reports numerical studies to illustrate our methods and compares them with the existing methods. Chapter 5 contains data sets and examples in the practical data analysis. Chapter 6 states and proves theorems about the sampling properties of our methodology.

# Chapter 2

# Literature Review

In this chapter, we review a few popular methods for fMRI data analysis and the HRF modeling.

## 2.1 A Model for BOLD Signals

In an experiment design with a single type of stimulus, the BOLD response $Y(t)$ acquired from the scanner is supposed to fluctuate with the stimulus activated at times $\tau_1 < \tau_2 < \cdots$. A popular model for the BOLD response (Friston et al., 1993) is the *linear time invariant system*:

$$Y(t) = \sum_u h(t - \tau_u) + \epsilon(t), \tag{2.1.1}$$

where $h(\cdot)$ is the HRF and $\epsilon(t), t = 0, 1, \ldots, T-1$ is a stationary, 0-mean noise series. Typically, a hemodynamic response lasts for 20 to 30 seconds, that is, $h(u) = 0$ when $u < 0$ and $u > d$ for some positive constant $d$.

Model (2.1.1) can also be written as

$$Y(t) = \sum_{u=1}^{d} h(t - u)s(t) + \epsilon(t), \quad t = 0, \ldots, T-1, \tag{2.1.2}$$

where $s(\cdot)$ is the 0-1 (0=off and 1=on) time series of the stimulus. This is called the

*convolution model*, where the BOLD response is modeled as the convolution of HRF and the stimulus function $s(\cdot)$. When there are $n$ stimuli, then model (2.1.2) can be extended to

$$Y(t) = \sum_{u=1}^{d} h_1(t-u)s_1(t) + \cdots + \sum_{u=1}^{d} h_n(t-u)s_n(t) + \epsilon(t), \quad t = 0, \ldots, T-1. \quad (2.1.3)$$

**The General Linear Model Framework**

As one of the most popular approaches, the *general linear model* (GLM) models the BOLD signal as a linear combination of several different component predictors. It is used to test whether the activity in a brain region is systematically related to any of those known input functions (Lindquist, 2008). The data input for fMRI analysis includes the response $Y(t)$ of the voxel at time $t$, and also the stimulus function $s(t)$. Considering the relationship between the stimulus and the response, the GLM was first elucidated by Friston, Holmes, Worsley, Poline, Frith, Frackowiak, et al. (1995b). It may be expressed as

$$\mathbf{Y} = \mathbf{X}\beta + \epsilon \quad (2.1.4)$$

where $\mathbf{Y} = (Y(0), Y(1), \ldots, Y(T-1))^\tau$ is the vector of the time series data, $\mathbf{X}$ is the $T \times p$ design matrix, and $\epsilon$ is the error vector. Each column of $\mathbf{X}$ represents one of the experimental BOLD response predictors. Their corresponding parameters are represented by $\beta$ as a $p \times 1$ vector. In most studies, the predictor is obtained by the convolution model (2.1.2) of the pre-specified HRF $h(\cdot)$ (see Figure 1.2) and a single stimulus $s(\cdot)$ (Figure 1.1a, 1.1b). The GLM also adapts to the multi-stimuli design based on the linearity assumption. When there are $n$ stimuli, there will be at least $n$ columns of $\mathbf{X}$ with each column corresponding to one stimulus (sometimes multiple basis functions may be used to represent the HRF for a particular stimulus, so there is more than one column to represent the effect caused by one stimulus).

The parameter vector $\beta$ will be estimated in each voxel to weigh the effect of each experimental predictor.

As the HRF $h(\cdot)$ is involved as part of the predictor from the design matrix $\mathbf{X}$, an accurate hemodynamic response can improve the statistical power of the fMRI modeling analysis. Under the GLM framework, many studies looked into the design matrix $\mathbf{X}$ and tried to capture the characteristics of the hemodynamic response, and to come up with valid predictors. Mumford and Nichols (2006) summarized the GLM framework and its implementation in various fMRI softwares. Some studies (Zhang, Lu, Johnstone, Oakes, and Davidson, 2008; Casanova, Ryali, Serences, Yang, Kraft, Laurienti, and Maldjian, 2008) also explore the error correlation structure to improve the efficiency of the estimation. Lindquist, Meng Loh, Atlas, and Wager (2009) furthermore propose some consequent statistical inference after estimating HRF.

When multiple stimuli are presented in succession, the hemodynamic response is often assumed to be the summation of the individual responses generated by the each stimulus respectively (Dale and Buckner, 1997). Under certain conditions, the fMRI response has been found to be approximately linear (Hykin, Bowtell, Glover, Coxon, Blumhardt, and Mansfield, 1995; Boynton et al., 1996), and this has been the basis for most of the event-related fMRI analysis to date (Buckner, Bandettini, OCraven, Savoy, Petersen, Raichle, and Rosen, 1996; Cohen, 1997; Friston, Fletcher, Josephs, Holmes, Rugg, and Turner, 1998a). GLM adapts to multiple-stimulus through the cooperation of multiple columns in the design matrix $\mathbf{X}$ based on the linearity assumption.

## 2.2 HRF Modeling

In early fMRI studies, researchers simply regarded the HRF $h(\cdot)$ as a *priori*, that is, the HRFs are assumed to be known, and then the predictor of BOLD response

is easily obtained from the convolution model (2.1.2). Most studies in the GLM framework obtain predictors based on known HRFs, and plug them into the design matrix $\mathbf{X}$, so as to test whether the predictors are able to detect the activities. A variety of fixed HRFs has been used in early studies, such as the Poisson function (Friston, Jezzard, and Turner, 1994), the Gamma function (Cohen, 1997; Lange and Zeger, 1997; Friston, Josephs, Rees, and Turner, 1998b) and the Gaussian function (Rajapakse, Kruggel, Maisog, and Von Cramon, 1998; Kruggel and von Cramon, 1999; Dale and Buckner, 1997). After Glover (1999) intensively investigated the shape of the HRF, the typical HRF shape (Figure 1.2) is suggested in the form of a double Gamma function. Since then the double Gamma function has been widely used in fMRI studies and popular fMRI data analysis packages, such as Statistical Parametric Mapping (SPM), FMRIB Software Library (FSL), and Analysis of Functional NeuroImages (AFNI). For example, the double Gamma function is the canonical HRF in SPM, which is the default choice.

Because the HRF varies across individuals and across brain regions, there exists no fixed "standard" form of HRF. It is crucial to allow flexibility in the exact HRF form while analyzing fMRI data; otherwise, even minor mismodeling of the HRF can result in severe power loss, and can inflate the false positive rate beyond the nominal level.

There is a list of literature on estimating HRF using fMRI data. Below we have organized the literature into two major categories: time domain and frequency domain, which will be reviewed in sections 2.2.1 and 2.2.2.

### 2.2.1 Time Domain Methods

Plenty of HRF studies use a basis function approach under the GLM framework. Friston, Frith, Turner, and Frackowiak (1995a) choose two basis functions with the

form of a product of a sine function and exponential functions, which model the early and late components of an evoked hemodynamic response. Bullmore, Brammer, Williams, Rabe-Hesketh, Janot, David, Mellers, Howard, and Sham (1996) and Zarahn (2000) choose the sinusoidal orthogonal basis functions. Josephs, Turner, and Friston (1997) use two sine basis functions. Lindquist and Wager (2007) model the HRF using a superposition of three inverse logit functions. Jacobs, Hawco, Kobayashi, Boor, LeVan, Stephani, Siniatchkin, and Gotman (2008) and Steffener, Tabert, and Stern (2009) employ Fourier basis sets to model the HRF. In general, the more basis functions are used in a linear model, the more flexible the model is in estimating the parameters of the GLM. However, flexibility relies on the cost of more free parameters, which means more error in estimating HRF, fewer degrees of freedom, and less statistical power due to potential collinearity.

Several Bayesian methods have also been developed in HRF modeling. Genovese (2000) uses the polynomial "bell" function to indicate the rise, fall, decay, and dip parts of the HRF. Gössl, Fahrmeir, and Auer (2001) derive the method based on physiological assumptions with the posterior estimated by numerical or Markov chain Monte Carlo (MCMC) methods. In Friston, Penny, Phillips, Kiebel, Hinton, and Ashburner (2002), an empirical Bayesian approach is taken to model the HRF with basis functions under constraints. Woolrich, Jenkinson, Brady, and Smith (2004) present a fully Bayesian approach using the addition of four half-period cosines with six constrained parameters to account for the variation of HRF. All these Bayesian approaches require imposing restrictions on the HRF parameters.

Many other time-domain approaches have been proposed in recent years. Ward and Revision (2000) propose the deconvolution model for HRF estimation without any specific assumptions on the HRF. It is implemented in a popular fMRI analysis software, AFNI (Analysis of Functional NeuroImage), to estimate HRF. The

time-domain deconvolution method still has the collinearity problem, especially for the periodic experimental designs. Lu, Bagshaw, Grova, Kobayashi, Dubeau, and Gotman (2006; 2007) compare the performance between three fixed HRFs (Gamma HRF, Glover HRF, and SPM canonical HRF) and the deconvolution method under the framework of GLM. Goutte, Nielsen, and Hansen (2000) propose a semiparametric approach based on *finite impulse response* (FIR) filters, which have more flexibility in modeling HRF. Zhang, Jiang, and Yu (2007; 2008) propose a semiparametric method that uses smoothing splines to estimate the drift function and the HRF while carefully taking into account the covariance structure within the BOLD signal. However, the semiparametric methods of Goutte et al. (2000) and Zhang et al. (2007; 2008) require some specific assumption of the covariance structure, which might not be correct. And both methods are computationally expensive. More recently Lindquist et al. (2009) compare several HRF estimating methods based on simulation and real data analysis, including SPM (Statistical Parametric Mapping) canonical HRF with or without its temporal or dispersion derivatives, FIR, semiparametric FIR, and the inverse logit model. So far, we can see that the "standard" HRF estimation lacks the natural spatial variability of HRF, and the model-driven approach generally has collinearity problems.

### 2.2.2 Frequency Domain Methods

Currently some fMRI analyses use frequency domain methods. Mitra, Ogawa, Hu, and Ugurbil (1997) consider spatiotemporal changes in the cerebral hemodynamics and verify that the white-noise assumption is inadequate. Lange and Zeger (1997) propose a non-linear parametric model for brain-activation detection. The model, including both temporal and spatial statistical inferences, recasts in the frequency

domain to simplify convolution evaluations and for easier accommodation of temporal and spatial autocorrelation. Marchini and Ripley (2000) offer a frequency domain method for the periodic stimuli with self-calibrating. It detects activation on the fundamental (stimulus-related) frequency and harmonics of the stimulus design per voxel with the information from other frequencies to calibrate its statistic. For HRF modeling, Makni, Beckmann, Smith, and Woolrich (2008) propose a nonparametric HRF estimate using fully Bayesian inference through Markov Chain Monte Carlo (MCMC) at the price of a high computational demand. Another frequency-domain method is Wink, Hoogduin, and Roerdink (2008) based on the Fourier-wavelet regularized deconvolution technique. Bai et al. (2009) implement a nonparametric model for estimating the HRF using fast Fourier transformation of event-related fMRI data. We describe the technical details in the next chapter, as our work builds upon their method.

### 2.2.3 Comparison of the Current Methods

Most existing analytical techniques for fMRI data need specific assumptions about the HRF. These assumptions may not be appropriate when the HRF varies from subject to subject or from region to region, especially for the pre-specified HRF methods. Sometimes the experiment contains more than one type of stimulus, and the application for the parametric methods may not be adapted for the multiple stimuli. Additionally, it is unlikely that the fMRI data is homogeneous from the whole scanning session, so the error correlation structure should be considered in the analysis, the estimation of which could be another difficulty in fMRI modeling.

Based on a periodic stimulus design, the frequency-domain approaches simplify the analysis by determining a few parameters related to the stimulus frequency information without considering the correlation structure in the noise series. Lange and

Zeger (1997) and Marchini and Ripley (2000) both outline the frequency approaches depending on the pre-defined HRF. They lack the ability to specify the HRF variation or adapt to the different types of stimulus design (Figure 1b, 1c). Bai et al. (2009) implement a nonparametric model of estimating HRF in the event-related experimental design. Their method exploits the experimental designs by modeling the stimulus sequences using a stochastic point process and accounts for the variability of HRFs across regions of brain. The method is proposed only in a single event-related design, and we extend this method to block design and the design that allows the multiple, overlapping events throughout an experiment, such as rapid event-related design. We describes their method in the following section for future reference.

### 2.2.4 Nonparametric HRF Modeling

In order to understand our method better in terms of terminology, such as the derivation of its name, we first define the *system transfer function* by

$$H(r) = \sum_{\upsilon} h(\upsilon) \exp(-\mathrm{i}\upsilon r), \quad r \in \mathbb{R} \tag{2.2.1}$$

where $r$ is the radian frequency. Practically, we use the finite Fourier transform

$$\varphi_Y(r) \equiv \varphi_Y^{\tau}(r) = \sum_{t=0}^{T-1} \exp(-\mathrm{i}rt) Y(t) \tag{2.2.2}$$

with a similar definition for $\varphi_X(r)$ and $\varphi_\epsilon(r)$, $r \in \mathbb{R}$. It follows from (2.1.2) that

$$\varphi_Y(r) = H(r)\varphi_X(r) + \varphi_\epsilon(r), \quad r \in \mathbb{R}. \tag{2.2.3}$$

By fast Fourier transform, $\varphi_Y(\cdot)$ and $\varphi_X(\cdot)$ are obtained on the Fourier frequencies $2\pi k/T$, $k = 0, \ldots, T-1$. Here $X(t)$ is the same as the stimulus function $s(t)$ in (2.1.2).

Bai et al. (2009) exploits the experimental designs by modeling the stimulus sequences using point process and accounts for the variability of HRFs across regions of brain. Here we describe some details given in Bai et al. (2009) to help understand our methodology. Note that this method is in a univariate form.

Let $m_r$ denote the integer $m \in \{0, \ldots, T-1\}$ such that $2\pi m_r/T$ is closest to the angular frequency $r \in (0, \pi/2)$. Then for the smooth $H(\cdot)$,

$$\varphi_Y(\frac{2\pi}{T}(m_r+k)) \approx H(r)\varphi_X(\frac{2\pi}{T}(m_r+k)) + \varphi_\epsilon(\frac{2\pi}{T}(m_r+k)) \tag{2.2.4}$$

for all $k = 0, \pm 1, \ldots, \pm K$, where $K$ is a positive integer. As we can see, $\{\frac{2\pi}{T}(m_r+k)\}_k$ are the nearest $2K+1$ frequencies around $r$ among the Fourier frequencies. Equation (2.2.4) is a linear regression system which can offer a reasonable estimate of $H(r)$, denoted by $\hat{H}(r)$.

$$\hat{H}(r) = \hat{f}_{YX}(r)/\hat{f}_{XX}(r) \tag{2.2.5}$$

where

$$\begin{aligned}
\hat{f}_{XX}(r) &= (2K+1)^{-1} \sum_{k=-K}^{K} I_{XX}(\frac{2\pi}{T}(m_r+k)), && (2.2.6)\\
\hat{f}_{YX}(r) &= (2K+1)^{-1} \sum_{k=-K}^{K} I_{YX}(\frac{2\pi}{T}(m_r+k)), && (2.2.7)\\
I_{XX}(r) &= (2\pi T)^{-1}\varphi_X(r)\overline{\varphi_X(r)}, && (2.2.8)\\
I_{YX}(r) &= (2\pi T)^{-1}\varphi_Y(r)\overline{\varphi_X(r)}, && (2.2.9)
\end{aligned}$$

where $\overline{A}$ is the conjugate of $A$. In practice, a smoother estimate known as the window estimate is used by observing that (2.2.6) and (2.2.7) can be written as

$$\hat{s}_{XX}(r) = \sum_{k\neq 0} b^{-1}W(b^{-1}(r - \frac{2\pi k}{T}))I_{XX}(\frac{2\pi k}{T}), \tag{2.2.10}$$

$$\hat{s}_{YX}(r) \quad = \quad \sum_{k \neq 0} b^{-1} W(b^{-1}(r - \frac{2\pi k}{T})) I_{YX}(\frac{2\pi k}{T}), \tag{2.2.11}$$

where $W(\cdot)$ is a weight function called a (spectral) window, and $b$ is the smoothing parameter. $\hat{s}_{XX}(r)$ is called *power spectrums* and $\hat{s}_{YX}(r)$ is *cross-spectrum*. It has been shown that the window estimate has better sampling properties than (2.2.8) and (2.2.9) as an estimate of the cross-spectrum of the bivariate time series.

With the defined smoothed power spectrums, $\hat{s}_{XX}(\cdot)$ and $\hat{s}_{YY}(\cdot)$, the stimulus point process $X(t)$ and the stationary time series $Y(t)$, and the estimate of the cross-spectrum $\hat{s}_{YX}(\cdot)$, the estimation of $H(\cdot)$ is

$$\hat{H}(r) = \hat{s}_{YX}(r)/\hat{s}_{XX}(r). \tag{2.2.12}$$

Consequently the estimate of the impulse response function $h(\cdot)$ is then given by the inverse Fourier transform.

For the statistical inference for detecting the activity, Bai et al. (2009) define the squared coherence as

$$|\hat{R}_{XY}(r)|^2 = \frac{|\hat{s}_{XY}(r)|^2}{\hat{s}_{XX}(r)\hat{s}_{YY}(r)}, \quad r \in \mathbb{R}. \tag{2.2.13}$$

Under certain conditions, $\hat{R}_{XY}(r)$ is asymptotically normal with a mean $R_{XY}(f)$ and variance proportional to the constant $(1 - R^2_{XY}(r))/T$. Moreover, if $R_{XY}(r) = 0$, then

$$F(r) = \frac{c|\hat{R}_{XY}(r)|^2}{1 - |\hat{R}_{XY}(r)|^2} \quad \sim \quad F_{2,2c}, \tag{2.2.14}$$

where $c$ is a constant that depends on the smoothing parameters. The $F$ statistic can then be used to test whether there is any response at the task-related frequency $r_0$. Under the null hypothesis of no activation, $F(r)$ has an $F$ distribution with 2 and

$2c$ degrees of freedom. An $F(r)$ value, which is larger than the presumed threshold, indicates a significant effect at the task-related frequency.

## 2.3 Popular Softwares in FMRI

SPM, FSL (FMRIB Software Library) , and AFNI are the three popular software packages in fMRI analysis. All of them contain important features of the hemodynamic response in GLM framework, such as detecting activation and generating an activation map. They implement the GLM framework in three steps: pre-processing the fMRI data, approaching the design matrix, and estimating the error structure. In these three steps for fMRI analysis, SPM, FSL, and AFNI may analyze the data differently, but their purpose and philosophy are basically the same. The pre-process for fMRI data includes realignment; co-registration; segmentation; normalization; and smoothing, which removes the effects of motion, noise, and intersubject variation of neuroanatomy. The error estimation is based on an autocorrelation model to whiten the model temporally and spatially. As our concern is about hemodynamic response, we compare the ways to obtain hemodynamic response in the three software packages.

SPM takes the basis-function approach to model the hemodynamic response. The most common choice is the "Canonical HRF" with or without time and dispersion derivatives. The incorporation of the derivative terms allows for variations in subject-to-subject and voxel-to-voxel responses. Other basis sets include Fourier set, gamma functions, and FIR. For each of these options, the number of basis functions must be specified. Alternatively, the canonical HRF is a special case for choosing double Gamma basis functions. The FIR method is considered a selective averaging method.

By using FIR, SPM gives fitted hemodynamic response and PSTH (peristimulus time histogram) on ROI (region of interest), called peristimulus time (PST) averaging. That is, SPM calls the HRF estimator a fitted response. PSTH is the histogram of

the times at which neurons fire. (To make a PSTH, a spike train recorded from a single neuron is aligned with the onset, or a fixed phase point, of an identical stimulus repeatedly presented to an animal. The aligned sequences are superimposed in time, and then used to construct a histogram.)

FSL (Woolrich, Jbabdi, Patenaude, Chappell, Makni, Behrens, Beckmann, Jenkinson, and Smith, 2009; Smith, Jenkinson, Woolrich, Beckmann, Behrens, Johansen-Berg, Bannister, De Luca, Drobnjak, Flitney, et al., 2004) also applies GLM to data. By default, FSL uses a single gamma function with temporal derivatives as HRF. It also has options on convolving with Gaussian function, double gamma function, and basis functions such as gamma, sine, and FIR. Furthermore, FSL has another approach to directly tune the HRF to make the optimal basis functions with four half-period cosine components. Also when the constraints for the HRF parameters are chosen, the basis function is automatically generated in FSL using singular value decomposition (SVD).

AFNI uses deconvolution analysis of fMRI time series data (Ward and Revision, 2000), which has two primary applications: (1) estimation of the system impulse response function (HRF, as we call it), and (2) multiple linear regression analysis of time series data. Even though the deconvolution analysis is less biased than the basis-function approach, it has the high requirement of the experimental design, that is, the periodic design is barely processed to get the HRF estimation by deconvolution methods here.

# Chapter 3

# Methodology: Three New Developments in HRF Modeling

This chapter focuses on the methodology of our developments in HRF modeling. Section 3.1 presents our first development: transfer function estimate (TFE), an HRF estimating method which incorporates the multiple stimuli in fMRI study. Following the multiple stimuli discussion, the multivariate tests are introduced in Section 3.2. In Section 3.3, we propose an efficient HRF estimator. To estimate the smooth parameter included in the computing process, Section 3.4 discusses our proposal for the analysis of fMRI time series.

## 3.1 Multivariate Form of HRF Modeling: Transfer Function Estimate

In order to obtain the efficient fMRI response in a limited scanning time, multiple types of stimuli are in high demand. The direct advantage in using multiple stimuli is that the BOLD fMRI refractory effect is avoided (Friston et al., 1998b). Subjects get bored easily if only one stimulus is shown repeatedly in a session. This refractory effect causes nonlinearity in the response, which will make later analyses more complex. Also, the scanner has limits on operation time, so multiple stimuli are helpful in making an efficient design in a limited time. Thus the stimulus attributes changing

over successive trials is beneficial for experiment design.

The method used by Bai et al. (2009) reviewed in Chapter 2 is set up for the types of stimulus with the univariate HRF involved in the experiment design; however, different stimuli may evoke varying HRFs even in the same location of the brain. For instance, there are two types of stimulus, A and B, in one scanning session. Stimulus A may stir up a much higher (or lower) response than Stimulus B; in terms of HRF shapes, it means a larger (or smaller) amplitude. Also the brain may have a quicker reaction to Stimulus A; in terms of HRF shapes, it proposes a different timing estimation for the lag. In brief, it is possible for stimuli A and B to have totally different HRF shapes. Additionally, more than two types of stimuli can be applied in the scanning session, making the analysis even more complicated.

Note that linearity assumption also works in multiple stimuli sessions. BOLD signal is basically the summation of all the HRFs evoked by any kind of stimulus.

The multivariate form of HRF modeling, called *transfer function estimate* (TFE), provided the statistical inference between different types of stimuli.Its name comes from the definition of Equation (2.2.1). Not only does the multivariate form give separate estimates of HRFs from different stimuli, but also the hypotheses on the same shape of HRFs among different stimuli are built on the multivariate model. Comparing the shapes of HRF is also of high interest in fMRI research. The hypotheses support some assumptions in fMRI, such as varying responses to the multiple specified stimuli. After the hypothesis testing, if it is acceptable to conclude that two kinds of stimuli have the same HRF shapes in the voxel of one subject, then the number of variates in the model decreases, which increases the statistical power for estimating HRF.

As the extension to the convolution model (2.1.2), the multivariate HRF model is

$$Y(t) = h_1 \otimes x_1(t) + h_2 \otimes x_2(t) + \cdots + h_n \otimes x_n(t) + \epsilon(t), \quad t = 0, \ldots, T-1 \quad (3.1.1)$$

where $x_i(\cdot)$ represents the $i$th stimulus function and $h_i$ is the corresponding HRF.

Let $\mathbf{X}(t)$ be an $n$ vector-valued series, that is, $\mathbf{X}(t) = (x_1(t), x_2(t), \ldots, x_n(t))^\tau$. Then suppose that $\mathbf{h}(u)$ is a $1 \times n$ filter as $\mathbf{h}(u) = (h_1(u), h_2(u), \ldots, h_n(u))$. The HRF model (3.1.1) we are concerned with have the form

$$Y(t) = \sum_u \mathbf{h}(u)\mathbf{X}(t-u) + \epsilon(t). \tag{3.1.2}$$

We assume that the error series, $\epsilon(t)$, is stationary with 0 mean and power spectrum $s_{\epsilon\epsilon}(r)$, and that the HRF $\mathbf{h}(u)$ is 0 when $u < 0$ or $u > d$, where $d$ is the length of HRF determined by underlying neural activity.

We can calculate the finite Fourier transform

$$\varphi_{\mathbf{X}}(r) \equiv \varphi_{\mathbf{X}}^{(T)}(r) = \sum_{t=0}^{T-1} \mathbf{X}(t) \exp(-\mathrm{i}rt). \tag{3.1.3}$$

Let $K$ be an integer with $2\pi K/T$ near radian frequency $r$. Suppose $T$ is large. From the asymptotic property of finite Fourier transform,

$$\varphi_Y(\frac{2\pi(K+k)}{T}) \doteq \mathbf{H}(r)\varphi_{\mathbf{X}}(\frac{2\pi(K+k)}{T}) + \varphi_\epsilon(\frac{2\pi(K+k)}{T}), \qquad k = 0, \pm 1, \ldots, \pm m. \tag{3.1.4}$$

Relation (3.1.4) is seen to have the form of a multiple regression involving complex-valued variates. In a matrix form, the linear system (3.1.4) is

$$\Phi_Y(r) = \begin{bmatrix} \varphi_Y(\frac{2\pi}{T}(K-m)) \\ \varphi_Y(\frac{2\pi}{T}(K-m+1)) \\ \vdots \\ \varphi_Y(\frac{2\pi}{T}K) \\ \vdots \\ \varphi_Y(\frac{2\pi}{T}(K+m)) \end{bmatrix}, \Phi_{\mathbf{X}}(r) = \begin{bmatrix} \varphi_{\mathbf{X}}(\frac{2\pi}{T}(K-m))^\tau \\ \varphi_{\mathbf{X}}(\frac{2\pi}{T}(K-m+1))^\tau \\ \vdots \\ \varphi_{\mathbf{X}}(\frac{2\pi}{T}K)^\tau \\ \vdots \\ \varphi_{\mathbf{X}}(\frac{2\pi}{T}(K+m))^\tau \end{bmatrix}^\tau,$$

$$\Phi_\epsilon(r) = \begin{bmatrix} \varphi_\epsilon(\frac{2\pi}{T}(K-m)) \\ \varphi_\epsilon(\frac{2\pi}{T}(K-m+1)) \\ \vdots \\ \varphi_\epsilon(\frac{2\pi}{T}K) \\ \vdots \\ \varphi_\epsilon(\frac{2\pi}{T}(K+m)) \end{bmatrix},$$

then we use ordinary least square (OLS) to estimate $\mathbf{H}(\cdot)$,

$$\hat{\mathbf{H}}(r) = (\Phi_{\mathbf{X}}(r)\overline{\Phi_{\mathbf{X}}(r)^\tau})^{-1}\Phi_{\mathbf{X}}(r)\overline{\Phi_Y(r)^\tau}. \tag{3.1.5}$$

We call (3.1.5) *uniform* estimate of $\hat{\mathbf{H}}(\cdot)$ as later we will define window estimate.

To make an easy extension in notation, alternatively we define

$$\mathbf{I}_{Y\mathbf{X}}(r) = (2\pi T)^{-1}\varphi_Y(r)\overline{\varphi_{\mathbf{X}}(r)}^\tau, \tag{3.1.6}$$

$$\mathbf{I}_{\mathbf{X}\mathbf{X}}(r) = (2\pi T)^{-1}\varphi_{\mathbf{X}}(r)\overline{\varphi_{\mathbf{X}}(r)}^\tau, \tag{3.1.7}$$

$$\hat{\mathbf{f}}_{Y\mathbf{X}}(r) = (2m+1)^{-1}\sum_{k=-m}^{m}\mathbf{I}_{Y\mathbf{X}}(\frac{2\pi(K+k)}{T}), \tag{3.1.8}$$

$$\hat{\mathbf{f}}_{\mathbf{XX}}(r) = (2m+1)^{-1} \sum_{k=-m}^{m} \mathbf{I}_{\mathbf{XX}}(\frac{2\pi(K+k)}{T}). \tag{3.1.9}$$

Suppose that the $n \times n$ matrix $\hat{\mathbf{f}}_{\mathbf{XX}}(r)$ is non-singular. We now write (3.1.5) as

$$\hat{\mathbf{H}}(r) = \hat{\mathbf{f}}_{Y\mathbf{X}}(r)\hat{\mathbf{f}}_{\mathbf{XX}}(r)^{-1} \tag{3.1.10}$$

and estimate $f_{\epsilon\epsilon}(r)$ by

$$\hat{f}_{\epsilon\epsilon}(r) = \frac{2m+1}{2m+1-r}[\hat{f}_{YY}(r) - \hat{\mathbf{f}}_{Y\mathbf{X}}(r)\hat{\mathbf{f}}_{\mathbf{XX}}(r)^{-1}\hat{\mathbf{f}}_{\mathbf{X}Y}(r)]. \tag{3.1.11}$$

The transfer function $\mathbf{H}(r)$ is estimated by expression (3.1.10). And the estimate of $\mathbf{h}(u)$ we consider

$$\hat{\mathbf{h}}(u) = \frac{1}{T}\sum_{t=0}^{T-1} \hat{\mathbf{H}}(\frac{2\pi t}{T}) \exp(\mathrm{i}2\pi tu/T). \tag{3.1.12}$$

Thus, $\hat{h}$ is the final HRF estimate from TFE.

### 3.1.1 Window Estimate

The window estimate has a good sampling property compared to the previous least square. Actually, the uniform estimate (3.1.8) and (3.1.9) is a special case of window estimate with the uniform window $W(\frac{2\pi k}{T}) = (2m+1)^{-1}$ as $k = 0, \pm 1, \ldots, \pm m$. By

observing (3.1.8) and (3.1.9), the window estimate can be written as

$$\begin{aligned}\hat{\mathbf{s}}_{Y\mathbf{X}}(r) &= \sum_{k=-m}^{m} W(\frac{2\pi k}{T})\mathbf{I}_{Y\mathbf{X}}(\frac{2\pi}{T}(K+k)) \\ &= \sum_{k=K-m}^{K+m} W(\frac{2\pi(k-K)}{T})\mathbf{I}_{Y\mathbf{X}}(\frac{2\pi k}{T}) \\ &= \sum_{k=K-m}^{K+m} W(\frac{2\pi k}{T}-r)\mathbf{I}_{Y\mathbf{X}}(\frac{2\pi k}{T}) \\ &= \sum_{k=K-m}^{K+m} W(r-\frac{2\pi k}{T})\mathbf{I}_{Y\mathbf{X}}(\frac{2\pi k}{T})\end{aligned}$$

where $W(\cdot)$ is a non-negative function called the *weight* or *window function*. Since the estimation process is required to be symmetric, we extend the weight function periodically.

$$W(\alpha+2\pi) = W(\alpha),$$

Note that $\mathbf{I}_{Y\mathbf{X}}(0) = 0$. In order to reflect the notion that the weight function should become more concentrated as the sample size $T$ tends to $\infty$, we introduce a bandwidth parameter $b$ that depends on $T$ (Brillinger, 1981) such that $b \to 0$ as $T \to \infty$, then for sufficiently large $T$,

$$\int_0^{2\pi} b^{-1}W(b^{-1\alpha})d\alpha = 1. \tag{3.1.13}$$

We therefore consider the following general window estimates:

$$\hat{\mathbf{s}}_{Y\mathbf{X}}(r) = \sum_{k\neq 0} b^{-1}W(b^{-1}(r-\frac{2\pi k}{T}))\mathbf{I}_{Y\mathbf{X}}(\frac{2\pi k}{T}), \tag{3.1.14}$$

$$\hat{\mathbf{s}}_{\mathbf{XX}}(r) = \sum_{k\neq 0} b^{-1}W(b^{-1}(r-\frac{2\pi k}{T}))\mathbf{I}_{\mathbf{XX}}(\frac{2\pi k}{T}), \tag{3.1.15}$$

and estimate $\mathbf{H}(r)$ by

$$\hat{\mathbf{H}}(r) = \hat{\mathbf{s}}_{Y\mathbf{X}}(r)\hat{\mathbf{s}}_{\mathbf{XX}}(r)^{-1}. \tag{3.1.16}$$

Then we have

$$\hat{\mathbf{h}}(u) = \frac{1}{T}\sum_{t=0}^{T-1} \hat{\mathbf{H}}(\frac{2\pi t}{T}) \exp(\mathrm{i}\frac{2\pi t u}{T}). \tag{3.1.17}$$

### 3.1.2 Multiple Smoothing Parameters

We can write down (3.1.14) and (3.1.15) as

$$\hat{\mathbf{s}}_{Y\mathbf{X}}(r) = \sum_{k\neq 0} \mathbf{W}((r - \frac{2\pi k}{T}), b)\mathbf{I}_{Y\mathbf{X}}(\frac{2\pi k}{T}), \tag{3.1.18}$$

$$\hat{\mathbf{s}}_{\mathbf{XX}}(r) = \sum_{k\neq 0} \mathbf{W}((r - \frac{2\pi k}{T}), b)\mathbf{I}_{\mathbf{XX}}(\frac{2\pi k}{T}), \tag{3.1.19}$$

where $\mathbf{W}(u, b)$ is an $n \times n$ weight matrix with $\{\mathbf{W}(u, b)\}_{ij} = W(u, b), i, j \in \{1, \ldots, n\}$.

The $n$ HRFs corresponding to the $n$ types of stimuli may have different smoothness, which requires different smoothing parameters for each HRF estimation. The proposed way to perform the multiple smoothing is to specify different $b_i$ in the weight matrix $\mathbf{W}(s, b)$. We can simply extend (3.1.18) and (3.1.19) to use $\mathbf{W}(u, b)$, an $n \times n$ weight matrix with $\{\mathbf{W}(u, b)\}_{ij} = W(u, b_i), \quad i, j \in \{1, \ldots, r\}$. The matrix forms are

$$\hat{\mathbf{s}}_{Y\mathbf{X}}(r) = \begin{pmatrix} \sum_{k\neq 0} b_1^{-1} W(b_1^{-1}(r - \frac{2\pi k}{T}))I_{Yx_1}(\frac{2\pi k}{T}) \\ \sum_{k\neq 0} b_2^{-1} W(b_2^{-1}(r - \frac{2\pi k}{T}))I_{Yx_2}(\frac{2\pi k}{T}) \\ \vdots \\ \sum_{k\neq 0} b_r^{-1} W(b_n^{-1}(r - \frac{2\pi k}{T}))I_{Yx_3}(\frac{2\pi k}{T}) \end{pmatrix}^{\tau}, \tag{3.1.20}$$

$$\hat{\mathbf{s}}_{\mathbf{XX}}(r) = \begin{pmatrix} \sum_{k\neq 0} b_1^{-1} W(b_1^{-1}(r - \frac{2\pi k}{T}))\mathbf{I}^{[1]}_{\mathbf{XX}}(\frac{2\pi k}{T}) \\ \sum_{k\neq 0} b_2^{-1} W(b_2^{-1}(r - \frac{2\pi k}{T}))\mathbf{I}^{[2]}_{\mathbf{XX}}(\frac{2\pi k}{T}) \\ \vdots \\ \sum_{k\neq 0} b_r^{-1} W(b_n^{-1}(r - \frac{2\pi k}{T}))\mathbf{I}^{[r]}_{\mathbf{XX}}(\frac{2\pi k}{T}) \end{pmatrix}, \tag{3.1.21}$$

where $(b_1, b_2, \ldots, b_n)$ are the smoothing parameters for HRFs $(h_1(\cdot), h_2(\cdot), \ldots, h_n(\cdot))$,

and $\mathbf{I}_{\mathbf{XX}}^{[i]}(\cdot)$ denotes the $i$th row of the matrix $\mathbf{I}_{\mathbf{XX}}(\cdot)$. The smoothing parameters for HRFs $(h_1(\cdot), h_2(\cdot), \ldots, h_n(\cdot))$ are $(m_1, m_2, \ldots, m_n)$.

When the smoothing parameters are different, the $\hat{\mathbf{s}}_{\mathbf{XX}}(r)$ may not be positive-definite. In practice, the task sequences of many experiments vary little, and so it seems reasonable to apply our procedure using the same smoothing parameters.

### 3.1.3 Coherence

Coherence is an important statistic that provides a measure of the strength of a linear time invariant relation between the series $Y(t)$ and the series $\mathbf{X}(t)$; that is, it indicates whether there is a strongly linear relationship between the BOLD response and the stimulus. From a statistical view, we can test the linear time invariant assumption for the convolution model; for the fMRI exploration, we can choose the voxels with significantly large coherence where the BOLD series have functional responses to the stimulus, and then estimate the HRF in those voxels.

Coherence is defined as

$$|R_{Y\mathbf{X}}(r)|^2 = \mathbf{s}_{Y\mathbf{X}}(r)\mathbf{s}_{\mathbf{XX}}(r)^{-1}\mathbf{s}_{\mathbf{X}Y}(r)/s_{YY}(r). \tag{3.1.22}$$

Coherence is seen as a form of correlation coefficient, bounded by 0 and 1. The closer to 1, the stronger linear time invariant relation between $Y(t)$ and $\mathbf{X}(t)$.

### 3.1.4 Partial Coherence

If we look at the stimuli individually, it is interesting to consider the complex analogues of the partial correlations, or *partial coherence*. The estimated *partial cross-spectrum* of $Y(t)$ and $X_i(t)$ after removing the linear effects of $\mathbf{X_j}(t)$ is given by

$$s_{Y\mathbf{X}_i\cdot\mathbf{X}_j}(r) = s_{Y\mathbf{X}_i}(r) - \mathbf{s}_{Y\mathbf{X}_j}(r)\mathbf{s}_{\mathbf{X}_j\mathbf{X}_j}(r)^{-1}\mathbf{s}_{\mathbf{X}_j\mathbf{X}_i}(r). \tag{3.1.23}$$

Usually, the point of interest is the relationship between the response and a single stimulus after other stimuli are accounted for; that is, $X_i$ is the single stimulus of interest, and $\mathbf{X}_j$ is the other stimuli involved in the design paradigm.

The partial coherence of $Y(t)$ and $X_i(t)$ after removing the linear effects of $\mathbf{X_j}(t)$ is given by

$$\left|R_{YX_i\cdot\mathbf{X}_j}(r)\right|^2 = \frac{s_{YX_i\cdot\mathbf{X}_j}(r)^2}{s_{YY\cdot\mathbf{X}_j}(r)s_{X_iX_i\cdot\mathbf{X}_j}(r)}. \tag{3.1.24}$$

If $n = 2$, that is, if there are two kinds of stimuli in the experiment, it can be written as

$$\left|R_{YX_i\cdot X_j}(r)\right|^2 = \frac{\left|R_{YX_i}(r) - R_{YX_j}(r)R_{X_iX_j}(r)\right|^2}{[1 - \left|R_{YX_j}(r)\right|^2][1 - \left|R_{X_iX_j}(r)\right|^2]}. \tag{3.1.25}$$

Partial coherence is especially important when we focus on a specific stimulus. Not all stimuli are considered in equal measure. Stimuli such as the heart beat and breathing, which cannot be avoided in any experiment involving humans, are of secondary concern. Furthermore, as each type of stimulus has its own characteristics, it is natural to perform an individual statistical analysis to see how each one affects the overall fMRI response.

## 3.2 Hypothesis Testing

### Testing Linearity

The linearity assumption functions as the essential basis of the convolution model. As we know, any nonlinearity in the fMRI data may be caused by the scanner system or the human physical capability such as *refractory*. Refractory effects refer to the reductions in hemodynamic amplitude after several stimuli presented. If refractory effects are present, then a linear model will overestimate the hemodynamic response to closely spaced stimuli, potentially reducing the effectiveness of experimental analyses. It is critical, therefore, to consider the evidence for and against the linearity of the

fMRI hemodynamic response.

It is possible that the nonlinearity is overwhelmed during scanning. Consequently, it is crucial to make sure that the linearity assumption is acceptable. The advantage of our method is that we can first determine whether the linearity assumption is acceptable before using the convolution model for analysis.

The value of coherence, between 0 and 1, reflects the strength of the linear relation between fMRI response and the stimuli. Under certain conditions, $\hat{R}_{Y\mathbf{X}}(r)$ is asymptotically normal with mean $R_{Y\mathbf{X}}(r)$ and variance proportional to constant $(1 - R^2_{Y\mathbf{X}}(r))/Tb$. Moreover, if $R_{Y\mathbf{X}} = 0$, then

$$F(r) = \frac{(c-n)|\hat{R}_{Y\mathbf{X}}(r)|^2}{n(1-|\hat{R}_{Y\mathbf{X}}(r)^2|)} \quad \sim \quad F_{2n,2(c-n)} \tag{3.2.1}$$

where $c = bT/\gamma$ and $\gamma = \int \kappa^2$ with $\kappa$ being the lag-window generator depending on the choice of window function. If the $F$ statistic on coherence is significant, it is reasonable to accept the linearity assumption.

**Testing the Effect from a Specific Stimulus**

For each brain area, stimuli have varying effects. For the motor cortex in the left hemisphere, right-hand motion causes much more neural activities than left-hand motion. Partial coherence is able to distinguish between right- and left-hand effects, determine whether left-hand motion evokes neural activity, and identify which motion has greater effect. The following test is applied for these kinds of research questions.

For partial coherence, if $R_{YX_i \cdot \mathbf{X}_j} = 0$, then

$$F(r) = \frac{c'|\hat{R}_{YX_i \cdot \mathbf{X}_j}(r)|^2}{1-|\hat{R}_{YX_i \cdot \mathbf{X}_j}(r)^2|} \quad \sim \quad F_{2,2(c'-1)} \tag{3.2.2}$$

where $c' = bT/\gamma - n + 1$ and $\gamma = \int \kappa^2$ with $\kappa$ being the lag-window generator.

### Detecting the Activation

HRF in fMRI indicates the arising neural activity. If there is activation evoked by the stimulus, then the corresponding HRF cannot be ignored. If there is no HRF in a brain region, there is no going-on neuronal activity. To detect activation in the brain region is to see whether there is underlying HRF. For our frequency method, we test $\mathbf{H}(r_0) = 0$ at stimulus-related frequency $r_0$.

We are interested in testing the hypothesis $\mathbf{H}(r) = 0$. This is carried out by means of analogs of the statistic (3.1.22). In the case of $\mathbf{H}(r) = 0$,

$$\frac{(bT/\gamma)\hat{\mathbf{H}}(r)\hat{\mathbf{s}}_{\mathbf{XX}}(r)\overline{\hat{\mathbf{H}}(r)^{\tau}}}{n\hat{s}_{\epsilon\epsilon}(r)} \tag{3.2.3}$$

is distributed asymptotically as $\mathbf{F}_{2;2(bT/\gamma-n)}$.

### Testing the Difference between HRFs

The multiple-stimulus method simplifies the functional hypothesis testing by comparing the corresponding Fourier coefficients at frequency r in order to see whether there is any discrepancy between HRF curves corresponding to different stimuli. HRFs curves are functions, but when we focus just on Fourier coefficients at frequency r, we look at a common hypothesis testing on points. To see the difference between the two HRFs, it is enough to consider the hypothesis that the two Fourier coefficients at task-related frequency $r_0$ are equivalent.

As we know, $\mathbf{H}(\cdot)$ is the Fourier transform of the form

$$\mathbf{H}(r) = \sum_{t=0}^{T-1} \mathbf{h}(t) \exp(-\mathrm{i}rt) \tag{3.2.4}$$

with the $\mathbf{h}(\cdot)$ real-valued. For the contrast hypothesis to compare HRF functions $\mathbf{c}^{\tau}\mathbf{h} = 0$, we have the equavalent hypothesis $\mathbf{c}^{\tau}\mathbf{H}(r) = 0$ by the form (3.2.4), where $r$

is usually the task-related frequency $r_0$.

In OLS method, we know the distribution of $\hat{\mathbf{H}}(r)^\tau$ is asymptotically

$$N_r^C(\mathbf{H}(r)^\tau, s_{\epsilon\epsilon}(r)\mathbf{\Sigma}) \quad \mathbf{H}(\lambda) \in \mathbb{C}^n \tag{3.2.5}$$

where

$$\mathbf{\Sigma} = \begin{cases} (bT/\gamma)^{-1}\hat{\mathbf{s}}_{\mathbf{XX}}(r)^{-1} & r \neq 0 \mod \pi \\ (bT/\gamma - 1)^{-1}\hat{\mathbf{s}}_{\mathbf{XX}}(r)^{-1} & r = 0 \mod \pi \end{cases}$$

$N_r^C(\cdot,\cdot)$ is the complex multivariate normal distribution for the $r$ vector-valued random variable.

**Definition 3.2.1.** The Complex Multivariate Normal Distribution. If $\mathbf{\Sigma} = \mathbf{\Sigma}_1 + \mathrm{i}\mathbf{\Sigma}_2$ is a complex-valued $m \times m$ matrix such that $\mathbf{\Sigma} = \mathbf{\Sigma}^\tau$ and $\mathbf{a}^\tau\mathbf{\Sigma}\mathbf{a} \geq 0$ for all $\mathbf{a} \in \mathbb{C}^m$, then we say that $\mathbf{Y} = \mathbf{Y}_1 + \mathrm{i}\mathbf{Y}_2$ is a complex-valued multivariate normal random vector with mean $\mu = \mu_1 + \mathrm{i}\mu_2$ and covariance matrix $\mathbf{\Sigma}$ if

$$\begin{bmatrix} \mathbf{Y}_1 \\ \mathbf{Y}_2 \end{bmatrix} \sim N\left(\begin{bmatrix} \mu_1 \\ \mu_2 \end{bmatrix}, \frac{1}{2}\begin{bmatrix} \mathbf{\Sigma}_1 & -\mathbf{\Sigma}_2 \\ \mathbf{\Sigma}_2 & \mathbf{\Sigma}_1 \end{bmatrix}\right). \tag{3.2.6}$$

We then write $\mathbf{Y} \sim N_m^C(\mu, \mathbf{\Sigma})$.

By the definition of complex normal distribution, then we have

$$\begin{bmatrix} \mathrm{Re}\ \hat{\mathbf{H}}(r)^\tau \\ \mathrm{Im}\ \hat{\mathbf{H}}(r)^\tau \end{bmatrix} \sim N\left(\begin{bmatrix} \mathrm{Re}\ \mathbf{H}(r)^\tau \\ \mathrm{Im}\ \mathbf{H}(r)^\tau \end{bmatrix}, \frac{1}{2}s_{\epsilon\epsilon}(r)\begin{bmatrix} \mathrm{Re}\ \mathbf{\Sigma} & -\mathrm{Im}\ \mathbf{\Sigma} \\ \mathrm{Im}\ \mathbf{\Sigma} & \mathrm{Re}\ \mathbf{\Sigma} \end{bmatrix}\right). \tag{3.2.7}$$

Simply notate the multivariate normal as

$$\hat{\mathbf{H}}_v^\tau \sim N(\mathbf{H}_v, \frac{1}{2}s_{\epsilon\epsilon}(r)\mathbf{\Sigma}_v) \tag{3.2.8}$$

where $\mathbf{H}_v$ is in a $2n$-dimensional real vector space, $\mathbf{H}_v = \begin{bmatrix} \text{Re } \mathbf{H}(r)^\tau \\ \text{Im } \mathbf{H}(r)^\tau \end{bmatrix}$ and $\mathbf{\Sigma}_v$ is a $2n \times 2n$ real matrix, $\mathbf{\Sigma}_v = \begin{bmatrix} \text{Re } \mathbf{\Sigma} & -\text{Im } \mathbf{\Sigma} \\ \text{Im } \mathbf{\Sigma} & \text{Re } \mathbf{\Sigma} \end{bmatrix}$.

The contrast between different HRF estimates can be represented by $\mathbf{c}^\tau \hat{\mathbf{H}}(r)^\tau$, where $\mathbf{c} = (c_1, c_2, \ldots, c_n)^\tau$ which satisfies that $\sum_{i=1}^n c_i = 0$. For the complex number $\mathbf{c}^\tau \hat{\mathbf{H}}(r)^\tau$, the hypothesis testing can be conducted by the definition of complex normal distribution, which converts complex normal to multivariate normal distribution.

Under the hypothesis $\mathbf{c}^\tau \mathbf{H}(r) = 0$, $(\mathbf{c} \quad \mathbf{c}) \begin{bmatrix} \text{Re } \hat{\mathbf{H}}(r)^\tau \\ \text{Im } \hat{\mathbf{H}}(r)^\tau \end{bmatrix}$, denoted by $\mathbf{c}_v^\tau \hat{\mathbf{H}}_v$, where $\mathbf{c}_v^\tau = (c_1, \ldots, c_n, c_1, \ldots, c_n)$, is distributed asymptotically as

$$N\left(0, \frac{1}{2} s_{\epsilon\epsilon}(r) \mathbf{c}_v^\tau \mathbf{\Sigma}_v \mathbf{c}_v\right). \tag{3.2.9}$$

At the same time the distribution of $\hat{s}_{\epsilon\epsilon}(r)$ is approximated by an independent

$$\frac{s_{\epsilon\epsilon}(r) \chi^2_{2(bT/\gamma - n)}}{2(bT/\gamma - n)} \quad r \neq 0 \mod \pi. \tag{3.2.10}$$

Thus, the $t$ statistic for the contrast between different HRF estimates is

$$\frac{\mathbf{c}_v^\tau \hat{\mathbf{H}}_v(r)^\tau}{\sqrt{\frac{2(bT/\gamma - n)}{bT/\gamma} \hat{s}_{\epsilon\epsilon}(r) \mathbf{c}_v^\tau \mathbf{\Sigma}_v^{-1} \mathbf{c}_v}} \quad \sim \quad t_{2(bT/\gamma - n)} \tag{3.2.11}$$

when $r \neq 0 \mod \pi$.

The contrast is highly utilized in fMRI to point out the discrepancy of responses in different conditions. In the fMRI softwares SPM and FSL, first we specify "conditions," which is analogous to types of stimuli here. For example, if we have two types of stimuli from the right and left hands, there are two conditions: Right and

Left. Then we need to set up the contrast of conditions according to our interest. For testing whether the right hand has greater effect than the left hand, the contrast should be Right>Left, equivalent to Right−Left> 0. So we state the contrast in a vector $\mathbf{c} = (1, -1)$, 1 for condition Right and $-1$ for condition Left. After settling the contrast, SPM and FSL will continue their general linear model, using parameters to conduct the $t$ statistic.

The hypothesis of comparing the HRF similarity here equates the contrasts in SPM and FSL. We have two types of stimuli: Right and Left. Then we have respective HRF estimates for Right and Left. To test whether Right>Left, we specify $\mathbf{c} = (1, -1)^\tau$ in $\mathbf{c}^\tau \hat{\mathbf{H}}(r)^\tau$. As the result, $t$ statistic in (3.2.11) is used for testing their difference.

## 3.3 Weighted Least Square

As shown in (3.1.5), we applied OLS to obtain the estimate of $\mathbf{H}(\cdot)$. The estimate (3.1.10) will be near an optimal estimate if $s_{\epsilon\epsilon}(r)$ is uniform. This is perhaps not likely in fMRI data, since the BOLD response is not homogeneous throughout the whole experiment. The efficient estimate is given by WLS (its proof can be found in Chapter 6), where we used, in practice and in theory, the estimate $\hat{s}_{\epsilon\epsilon}(r)$ obtained by the use of the same formulas given in (3.1.11) as the weight in the uniform estimate

$$\hat{f}_{\epsilon\epsilon}(r) = \frac{2m+1}{2m+1-r}[\hat{f}_{YY}(r) - \hat{\mathbf{f}}_{Y\mathbf{X}}(r)\hat{\mathbf{f}}_{\mathbf{XX}}(r)^{-1}\hat{\mathbf{f}}_{\mathbf{X}Y}(r)].$$

The WLS estimate of the linear system (3.1.4) is

$$\hat{\mathbf{H}}(r) = (\varphi^\tau_{\mathbf{X}}(r)\mathbf{\Sigma}(r)\overline{\varphi_{\mathbf{X}}(r)})^{-1}\varphi^\tau_{\mathbf{X}}(r)\mathbf{\Sigma}\overline{\varphi_Y(r)}, \tag{3.3.1}$$

where

$$\mathbf{\Sigma}(r) =$$

$$\begin{bmatrix} \hat{f}_{\epsilon\epsilon}^{-1}(\frac{2\pi}{T}(K-m)) & & & & & & \\ & \hat{f}_{\epsilon\epsilon}^{-1}(\frac{2\pi}{T}(K-m+1)) & & & & & \\ & & \ddots & & & & \\ & & & \hat{f}_{\epsilon\epsilon}^{-1}(\frac{2\pi}{T}K) & & & \\ & & & & \ddots & & \\ & & & & & \hat{f}_{\epsilon\epsilon}^{-1}(\frac{2\pi}{T}(K+m)) & \end{bmatrix}.$$

Then (3.1.8) and (3.1.9) are updated as

$$\hat{\mathbf{f}}_{Y\mathbf{X}}(r) = (2m+1)^{-1} \sum_{k=-m}^{m} \hat{f}_{\epsilon\epsilon}^{-1}(\frac{2\pi(K+k)}{T}) \mathbf{I}_{Y\mathbf{X}}(\frac{2\pi(K+k)}{T}), \tag{3.3.2}$$

$$\hat{\mathbf{f}}_{\mathbf{XX}}(r) = (2m+1)^{-1} \sum_{k=-m}^{m} \hat{f}_{\epsilon\epsilon}^{-1}(\frac{2\pi(K+k)}{T}) \mathbf{I}_{\mathbf{XX}}(\frac{2\pi(K+k)}{T}). \tag{3.3.3}$$

For the general window estimate, the weight in WLS is

$$\hat{s}_{\epsilon\epsilon}(r) = \frac{bT/\gamma}{bT/\gamma - r} [\hat{s}_{YY}(r) - \hat{\mathbf{s}}_{Y\mathbf{X}}(r) \hat{\mathbf{s}}_{\mathbf{XX}}(r)^{-1} \hat{\mathbf{s}}_{\mathbf{X}Y}(r)]. \tag{3.3.4}$$

Then the weighted spectrum is defined as

$$\tilde{\mathbf{s}}_{Y\mathbf{X}}(r) = \sum_{k \neq 0} b^{-1} W(b^{-1}(r - \frac{2\pi k}{T})) \hat{s}_{\epsilon\epsilon}^{-1}(\frac{2\pi k}{T}) \hat{\mathbf{s}}_{Y\mathbf{X}}(\frac{2\pi k}{T}), \tag{3.3.5}$$

$$\tilde{\mathbf{s}}_{\mathbf{XX}}(r) = \sum_{k \neq 0} b^{-1} W(b^{-1}(r - \frac{2\pi k}{T})) \hat{s}_{\epsilon\epsilon}^{-1}(\frac{2\pi k}{T}) \hat{\mathbf{s}}_{\mathbf{XX}}(\frac{2\pi k}{T}). \tag{3.3.6}$$

The transfer function estimate is generally given by

$$\tilde{\mathbf{H}}(r) = \tilde{\mathbf{s}}_{Y\mathbf{X}}(r)\tilde{\mathbf{s}}_{\mathbf{XX}}(r)^{-1} \tag{3.3.7}$$

## 3.4 Introduction of Modified Cross Validation

We now describe one procedure for choosing the bandwidth (that is the window size) needed in our HRF estimation method. We refer to it as *modified cross validation* (MCV). MCV is basically a technique for assessing how well the results of statistical analysis in a time series can be generalized to an independent time series. For fMRI data, we use MCV for selecting the bandwidth in the spectrum smoothing during the procedure of TFE. For us, MCV is designed for HRF modeling to select the proper smoothing parameter $M$ during the estimating procedure. The algorithm of MCV partitions a time series into consecutive subintervals, performing the analysis on one subinterval (called the *training set*), and validating the analysis on the other subinterval (called the *testing set*). To reduce variability, multiple rounds of MCV are performed by using different partitions, and the validation results are averaged over the rounds.

MCV is applied to the time series evoked by the stimulus sequence of fMRI data. Usually the stimulus sequence is an event-related design, which contains events over time. The basic initiation of MCV is partitioning all the events into two groups, one group for training and the other for testing. Dealing with time-related data groups, we use the first part of a time series (training interval) to estimate the HRF and the second part of a time series (testing interval) to validate it. Moreover, multiple rounds of cross validation are needed to reduce the variability. Therefore, the testing intervals may be divided into subintervals, using one within a round. The way of partitioning the time series depends on two variables, $Q$ and $w$, where $Q$ is the number of rounds

(that is, the number of testing subintervals), and $w$ is the length of the testing interval.

If a time series has length $n$, the algorithm of MCV is as follows.

1. Use the first $n - qw$ time points as a training interval to estimate HRF, $q = Q, Q-1, \ldots, 1$.

2. Predict the next $w$ time points by convolving the estimate HRF with the known stimulus sequence.

3. Calculate the Root Mean Squared Error (RMSE) on the predicted $w$ time points.

4. Sum up the RMSE over the $Q$ sequences, and select the smoothing parameter $M$ that minimizes the total RMSE.

The above procedure depends on the choice of $Q$ and $w$. By default, we use $Q = 10$ and $w = 0.05n$, which means 10 rounds of cross validation in the later half of the time series.

When two data sets—one set from theoretical prediction and the other from the actual measurement of some physical variable—are compared, the RMSE of the pair-wise differences in the two data sets can serve as a measure of how far on average the error is from 0. (The RMSE in the algorithm is to measure the expected level of fit of the model and here to determine the appropriate use of the smoothing parameter $M$. ) The methods proposed here will be investigated and justified based on the simulation and the real data application in the next two chapters.

# Chapter 4

# Simulation Study

We have several simulation studies corresponding to the three developments on HRF modeling. Section 4.1 applies the nonparametric method under rapid event-related design and block design. Section 4.2 is the simulation study of HRF estimate under a multiple-stimulus experiment. Section 4.3 validates the bandwidth selection method MCV in the simulation study. Then the multivariate hypothesis is tested in Section 4.4. The third development of estimation efficiency is verified in Section 4.5 through the comparison of WLS and OLS. Section 4.6 gives a comparison study on the specific experiment design called face data design among five current HRF modeling methods. By the end of the simulation study, we discuss the advantages of our method in Section 4.7.

## 4.1 Simulation 1: Various Experimental Designs

As mentioned in Section 1.2, the two common experimental designs in fMRI are event-related (Figure 1.1a) and block (Figure 1.1b) design. The event-related design includes *single event-related* and *rapid event-related* (Dale and Buckner, 1997). In block design fMRI, the stimulus exists for a longer duration of time compared to the event-related design, which becomes a challenge in assessing BOLD signal magnitude differences between conditions. The length of the blocks of stimulation allows for the HRF to reach maximal values, while the inter-stimulus intervals (ITI) may be long

enough for the HRF to return completely to the baseline during non-stimulation. In common sense, the block design is not powerful at estimating the shape of the hemodynamic response (aside from its magnitude). However, TFE is powerful enough to be applied to all types of experimental designs.

The simulation here follows the convolution model (2.1.2), where $h$ is the Glover HRF (Glover, 1999), and $\epsilon(t)$ is white noise; that is, $\epsilon \sim N(0, .25)$. The various experimental designs that follow are denoted by $x(\cdot)$.

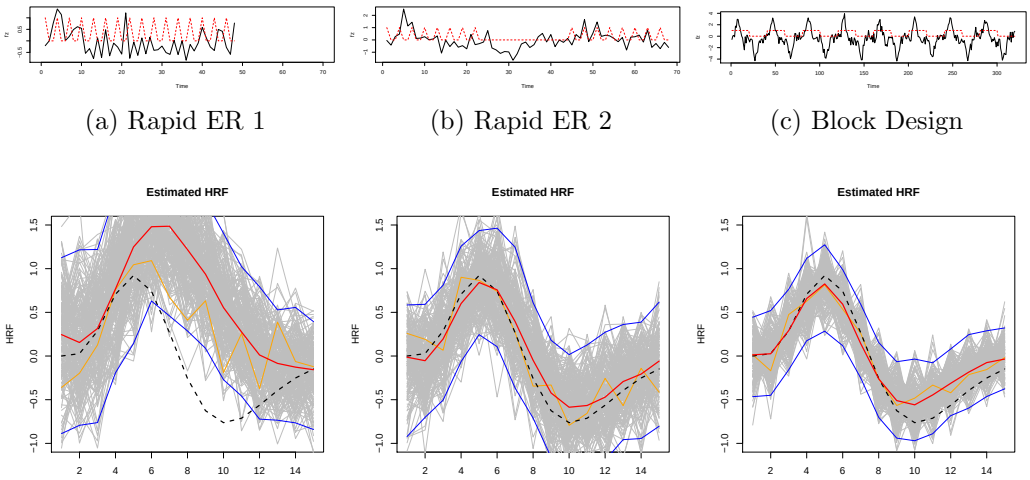


(a) Rapid ER 1 (b) Rapid ER 2 (c) Block Design

(d) Rapid ER 1 (e) Rapid ER 2 (f) Block Design

Figure 4.1: HRF modeling with three different experimental designs. In (a),(b), and (c) of the upper row, the red lines show the respective stimulus functions, that is, the presence of stimulus along time, and the black line shows the time series of the simulated fMRI response, which is the convolution between the stimulus function and the Glovers HRF (shown as the black dashed line in (e), (f) and (g)); the bottom row shows the HRF estimates for each design. We obtained 200 HRF estimates from 200 simulations, which are shown in grey. The thick red line shows the average of them, and the two, thin blue lines show the 2.5% and 97.5% quantile. The simulation result shows the HRF estimation is affected by the experimental designs. For example, for the rapid event-related design as (a) shows, adding an extra resting period (in (b)) improves its HRF estimates dramatically.

### 4.1.1 Event-Related Design

In Bai et al. (2009), the authors have shown that the method is successful in the single event-related design. Here we applied their method to the rapid event-related design.

The first simulation was the rapid ER-fMRI with a fixed ITI of 2 seconds (Figure 4.1a). We applied the method to the simulated data, obtaining 200 HRF estimates from the 200 simulations we ran. The results are shown in Figure 4.1d. The application of the method to the simulated rapid event-related design data resulted in HRF estimates that captured the original shape of HRF, represented by the dark red line in Figure 4.1d. The average of the estimates captured the shape of the true HRF, but it is above the true HRF dash line. The bias of the estimates comes from the experimental design: the stimulus frequency is so high that it keeps the HRF from reaching maximal values without returning to its baseline. Thus the estimates have a much higher peak than the true one without the post-dip. The results from this simulation led us to consider how to optimize the method and data to better estimate the HRF in rapid ER-fMRI. The second simulation gave us more information on experimental design parameters and improved estimation of the HRF.

The second simulation was also a rapid ER-fMRI with a fixed ITI of 2 seconds. In addition, we included an extra rest period in the middle that was 20 seconds in duration (see Figure 4.1b for a schematic). The extra rest period is long enough for the HRF to return completely to baseline during non-stimulation. We again applied the method of Bai et al. (2009) to this simulated data set, and the results are shown in Figure 4.1e. Whereas in this second simulation only one extra rest period was added compared to the previous simulation, we obtained HRF estimates that were dramatically improved compared to the results from the first simulated data. In contrast to the results from the first stimulation, the best estimate of the HRF (shown

by the thin original line) was now approximately superimposed on the average HRF and the experimental design. In this data analysis, the bias was largely removed and the estimate of the HRF shifted down to the correct position.

The improved results from the second simulation showed that the rest period was a crucial component of the experimental design. Even in the case when the stimulus frequency was high, we demonstrated that as long as there was one relatively long rest, we could still obtain good estimates of the hemodynamic response using our method. In summary, the advantages of this second experimental design include improved HRF estimates in rapid ER-fMRI.

### 4.1.2 Block Design

Block designs are very good at detecting significant fMRI activity. While their detection power can be very good as long as the difference in BOLD signal between conditions is larger, block designs are relatively insensitive to the shape of the hemodynamic response. With a task block of about 10 seconds or longer, which are greater than the latency of the HRF to a single stimulus, every time point within the block contains a cumulative contribution from the continuous stimuli. Thus, the combined hemodynamic response rises rapidly at the onset of the task, thereafter remaining at a plateau value until the cessation of the block. Since the plateau value represents contributions from all phases of the hemodynamic response, the particular shape of the response does not matter. Although block design is insensitive to the shape and timing of the HRF, its primary advantage is that it makes experimental analysis simpler, since the requirement on the shape of HRF is reduced as long as HRF consists of a rise, plateau, and fall. However, if we use the convolution model later, the shape of HRF is still needed in a block design, and its timing also affects the statistical power in the experimental analysis.

Even though block design is relatively insensitive to the HRF's exact shape, in this section we apply our method under block experimental design to get the exact estimation of HRF. The simulation was set up with runs consisting of 16 blocks, with each block having a duration of 20 seconds. The block alternated between the stimuli and rest (Figure 4.1c). Based on the fact that the common hemodynamic response usually lasts around 15 seconds (as in the Glover HRF), we chose a block period of 20 seconds so that each block would not have any carry-over effect from the previous block. We then applied the method to this simulated data, obtaining 200 HRF estimates from the 200 simulations we ran. The results are shown in Figure 4.1f. The application of the method from Bai et al. (2009) to the simulated block design data resulted in HRF estimates that captured the original shape of HRF, represented by the dark red line in Figure 4.1c, with the 95% confidence interval designated by the blue lines above and below the red line. These data demonstrate that our adjusted method can extract the hemodynamic response pattern not only from event-related data (as in Bai et al. (2009)), but also from block design data. According to the estimates of the average HRF, however, we could see the relatively small bias in the estimates (the true HRF is the dashed line). The true HRF, however, is covered by the upper and lower bounds of the estimates.

## 4.2 Simulation 2: Multiple Stimuli

We proposed the multiple-stimulus method as a multivariate extension from the method of Bai et al. (2009). In this section, we illustrate its usefulness in simulation studies. As we have two types of stimuli involved in the experiment, in reality there are three possible results: two different HRFs are provoked by the two types of stimulus, two similar HRFs are evoked, or the brain region does not respond to one of the stimuli. To test whether the multiple-stimulus method can be used in all the

situations, we did the simulation in each situation.

The simulations were built on the block design with two types of block interchanging (Figure 4.2a). There were enough rest periods for HRF so it would not affect the successive blocks. The first simulation was to estimate two different shapes of HRF, using Glover's HRF and function

$$\frac{\sin(2\pi x)}{2x} \quad x = -2, -1.9, -1.8, \ldots, -.6. \tag{4.2.1}$$

In Figure 4.2b, the dashed lines are the true HRFs, and the solid lines are the mean of estimates from 200 simulations with 95% gray band. As we can see, there is a large gap between the timing for peaks of Glover and $\sin(x)/x$ HRFs. Furthermore, the amplitudes of the two HRFs are not the same. As a result of dissimilar HRFs, the estimates from multivariate method fit the original HRFs well, separating the peaks and the amplitude from each other.

The second simulation (Figure 4.2c) had two similar HRFs functions: two cubic functions. The difference between the two cubic functions was subtle, from which we could only see a little difference in the starting point and undershoot period. Even though the difference was slight, the estimates still clearly identified the small difference between the two HRFs.

The third simulation (Figure 4.2d) states the possibility that there is no response to a stimulus. In Figure 4.2d, the second HRF is 0, which means no response exists for the second stimulus. The HRF estimates are consistent with the original ones, which confirms the confidence of using a multivariate method to estimate multiple HRFs.

TFE does not depend on the actual length of HRF. Most of the current parametric and nonparametric HRF modeling methods require the input of the length of HRF. However, in practice, the length of HRF is unknown, and the results are sensitive

to the input length. TFE has the advantage that it does not assume the length of HRF a *priori*, so the length of HRF does not affect the estimation performance of TFE, as shown empirically in Figure 4.3. In addition, the estimation results can give some suggestion about the support of the HRF. Furthermore, its result could give an estimate of the length of HRF. Figure 4.3 shows that the wrong HRF length could not affect the conducting result in TFE.

## 4.3 Simulation 3: Modified Cross Validation

As discussed in Section 3.4, MCV is used to choose bandwidth during the HRF estimating process. In Section 4.2, the smoothing parameter is chosen by hand or observation, which may not be efficient when dealing with noisy data or large data sets, since it is time consuming. In order to quickly choose a proper bandwidth in TFE, we introduced MCV and propose to use it in TFE.

In the simulations, we first set a standard way to select the smoothing parameter $M$, which directly minimizes RMSE between the true HRF used in the simulation and the estimated HRF conducted by TFE.

We denote $h$ as a vector of true HRF (vector length is $d$) and $\hat{h}$(M) as a vector of the estimated HRF using smoothing parameter $M$

$$RMSE(M) = \frac{1}{d}(\hat{h}(M) - h)^T(\hat{h}(M) - h).$$

For a single simulation, define $M_{opt}$ as

$$MSE(M_{opt}) = min(MSE(M)).$$

In order to evaluate $M$ obtained by MCV, we compare the HRF estimates generated by $M_{opt}$ and $M$ from MCV. The comparison on the random event-related design with low Signal-to-Noise Ratio (SNR) is shown in Figure 4.4. The HRF estimates by using MCV is sustaining.

In addition, we illustrate the performance of the MCV procedure on the three simulation studies performed in Section 4.2. The true HRFs have different combinations. As we can see from Figure 4.5, the window sizes chosen by MCV give very nice HRF estimates, and in all three cases, they are close to the results corresponding to the subjectively chosen bandwidths in Figure 4.2.

## 4.4 Simulation 4: Hypothesis Testing

The simulation study was based on a multiple stimuli experiment design and a simulated brain. The experiment in the section included two types of stimuli, called *left* and *right*. The simulated brain had $8 \times 8$ voxels, which was designed to have various brain functions in the left and right experiment design. The brain was divided into four regions: One only responded to left, one only responded to right, one can respond to both left and right, and the remaining one had no response in the experiment.

The fMRI data was simulated based on the convolution model (3.1.1): the convolution of the pre-specified left HRF $h_1(\cdot)$ and right HRF $h_2(\cdot)$, and the known experiment paradigm for left stimulus $x_1(t)$ and right stimulus $x_2(t)$. The response was given by

$$Y(t) = h_1 \otimes x_1(t) + h_2 \otimes x_2(t) + \epsilon(t), \quad t = 0, \ldots, T-1 \tag{4.4.1}$$

with $T = 600$. The noise was generated from an ARMA(2, 2):

$$\epsilon(t) - 0.8897\epsilon(t-1) + 0.4858\epsilon(t-2) = z(t) - 0.2279z(t-1) + 0.2488z(t-2),$$

$$z(t) \sim N(0, 0.2^2).$$

The ARMA was chosen to test the strength of our method under other types of correlated structures, and the coefficients were selected to illustrate the performance of the procedure under moderate, serially correlated noise.

The illustrated experiment paradigm and the brain map is shown in Figure 4.6. This was an event-related design with left and right interchanging, where the green stands for the left, and the purple stands for the right. The left and right stimuli came periodically. The stimulus-related frequency for each was 1/40, and the overall task-related frequency for the experiment was 1/20. The brain map shows the brain function in each region (Figure 4.6b).

The first simulation was to detect the activation regions in the brain. We assumed both of the original HRFs for left and right were Glover's HRF. At the experiment frequency 1/20, the coherence and $F$ statistic map shows in Figure 4.7. The lighter the color is, the higher the values are. The high value of coherence in the responsive region implies a strong linear relation in the simulation. Also, the $F$ statistic represents the strength of activation in the voxel. As expected, there were three activation regions: Left (L), Right (R), Left and Right (L&R), which was selected at $\alpha = 0.01$ level.

At the stimulus-related frequency 1/40 level, we compared the similarity of left and right HRFs. The true left and right HRFs are the same Glover's HRF. The HRF discrepancy region are only two regions: Left (L) and Right (R), where we regarded no response as zero HRF. The simulation result is displayed in Figure 4.8. The rejection region for L>R is the region L; the rejection region for L<R is the region R; the

rejection region for L≠R is L&R at level $\alpha = .05$. As we can see, if the voxel has the same response to different stimuli, it shows in the result that there is no difference in the HRFs.

The second simulation was built on different HRFs. The left HRF kept Glover's HRF, and the right HRF reduced Glover's HRF to half. As we can see, the left and right HRFs had different amplitudes. The left was larger than the right one. At the experiment frequency 1/20, the activation region is accurately spotted in Figure 4.9.

At the individual-stimulus-related frequency 1/40, the difference between left and right HRF was detected, as shown in Figure 4.10. The rejection region for L>R contains the regions that respond to both L and R. The hypothesis testing of similar HRFs clearly separated different HRFs.

## 4.5 Simulation 5: Weighted Least Squares

WLS estimate is the extension of OLS proposed in Chapter 3 and is preferred. The simulation described in this section is based on the comprehensive methodology we proposed in Chapter 3. To have a clear idea about the advantage of the multivariate method and WLS, we compared the simulation results of univariate and multivariate, OLS and WLS in Figure 4.11. And we discuss the comparison of the following five methods: naive, univariate method with OLS/WLS, and multivariate method with OLS/WLS.

When we conduct the statistical analysis for a fixed experiment design with multiple types of stimuli, we usually have assumptions on the HRFs. One simple assumption is that all HRFs share the same shape, that is, the brain has the same response to any kind of stimuli. We call this assumption "naive." The brain has, however, varying responses to different types of stimuli. To separate the stimuli and estimate HRFs for each, we consider one type of stimuli at a time, that is we use one stimulus

function at a time without considering the other existing stimuli. This method is called "univariate" since just one of the stimuli is used. Moreover, the ideal case is that we consider the multivariate analysis including all the stimuli, and estimate the HRFs for each of them simultaneously. We use the multivariate method here.

Considering the OLS and WLS methods on estimating HRF, the five methods are following.

(i) Naive method (Naive)

(ii) Univariate method with OLS (OLSu)

(iii) Univariate method with WLS (WLSu)

(iv) Multivariate method with OLS (OLSm)

(v) Multivariate method with WLS (OLSm)

It should be noted that the naive method used OLS estimation.

The fMRI response is simulated as the sum of the convolutions of the HRF $h_i(\cdot)$ and the stimulus function $x_i(\cdot)$.

$$Y(t) = h_1 \otimes x_1(t) + h_2 \otimes x_2(t) + \epsilon(t), t = 0, \ldots, T-1 \tag{4.5.1}$$

The noise $\epsilon(\cdot)$ is heterogeneous as for each time point. It follows normal distribution with parameters $(0, \sigma^2)$, where $\sigma$ follows uniform distribution.

The Figure 4.12 shows the simulation on block design. We used two types of stimuli (the purple and green lines in Figure 4.12a) and two different HRFs. The two HRFs have the same smoothness since they are cubic functions: $(x-2)(x-11)(x-15)$ and $(x-1)(x-9)(x-15)$. Two hundred simulations were generated with the noise $N(0, \sigma^2)$, where $\sigma \sim U(0, 0.5)$, as denoted above. Figure 4.12b shows the HRF estimates from the five methods: the upper row is the HRF estimates for the purple

stimulus, and the bottom row for the green. In each estimating result, the gray lines are the 200 HRF estimates from the 200 simulations. The black curve is the true HRF, and the bold red dashed line is the average of the 200 HRF estimates. The gray band is between the 2.5% and 97.5% quantile of the 200 estimates.

In Figure 4.12b, the naive method (the 1st column) gave biased estimates, since it incorrectly assumes that the two types of stimuli have the same HRF estimates. The univariate method (the 2nd and 3rd columns) gave two different HRF estimates with lower variation. However, the bias is very large. The univariate method hardly distinguished the two HRFs. The multivariate method (the 4th and 5th columns) examined the two types of HRF at the same time, so the bias has been dramatically reduced in both HRF estimates. The average of 200 estimates is almost consistent with the true HRF. The variance, however, increased from the univariate method due to the additional covariates in the model, which leads to more variable estimates. Lower variation in estimation could be approached by increasing the number of block trials.

The improvement from OLS to WLS is obvious in Figure 4.12. Comparing the 2nd and 3rd column, or the 4th and 5th column, the WLS reduces the variation in estimation in the heterogeneous noise simulation. The multivariate method with WLS estimation is robust and consistent.

The estimation result in Figure 4.12 demonstrates that the multivariate method gives admirable estimates even though the HRFs from different types of stimuli are very similar to each other. What if the HRFs are very different? One extreme and possible case is that there is no response to one of the stimuli, that is, this HRF is zero. The simulation is shown in Figure 4.13. When we look at the zero HRF estimates, the multivariate method shows its robustness. It concludes that the average of the estimates is almost zero, while the univariate method shows there is still some small

perturbation for the zero HRFs.

Although with fixed number of trials the more variable estimate is generated by multivariate method, the conducted hypothesis testing from the multivariate method is more efficient. If we wish to compare the HRFs (that is, the null hypothesis is $H_1(\mathrm{r}_0) = H_2(\mathrm{r}_0)$ where $\mathrm{r}_0$ is the task-related radian frequency), the multivariate method will reduce the variance for estimating the $t$ statistic. After hypothesis testing on activation, if there is no significant evidence about HRF existing for one stimulus, then we should reduce the number of variables in the model in order to have more accurate HRF estimates for the other stimuli.

## 4.6 Simulation 6: Face Data Design

Face fMRI data set is an event-related design in Henson, Shallice, Gorno-Tempini, and Dolan (2002), where famous and non-famous faces were presented twice against a checkerboard baseline. There are thus four event-types of interest: the first and second presentations of non-famous and famous faces, which we denote as N1, N2, F1 and F2, respectively. The experimental stimuli and timings of events are shown in Figure 4.14a. According to the description of the study (Henson et al., 2002), the subject was required to push a button when he/she saw the second presentation of any face. Thus, the first and second presentations of a particular face are different types of stimuli. There were 52 faces presented in the experiment design, 26 famous and 26 non-famous. Also, the famous and non-famous faces may evoke different responses in the subject's brain. Considering the two factors, fame and repetition, in total we had four kinds of stimuli during the whole experiment session.

For the simulation here, we used the face data design but simulated the fMRI

data by using the convolution model of BOLD signal

$$Y(t) = \sum_u s_1(t-u)h_1(u) + \sum_u s_2(t-u)h_2(u) + \sum_u s_3(t-u)h_3(u) + \sum_u s_4(t-u)h_4(u).$$

The four summations responded to the four types of stimuli. For each one type of the stimuli, it had its own unique HRF such as $h_1(\cdot), h_2(\cdot), h_3(\cdot), h_4(\cdot)$. The simulation study was conducted by convolving the above stimulus function (experiment design) with HRFs. Since there are four event-types, four different HRFs were put to use for each, as shown in Figure 4.14b. The white noise was added over time with SNR=3. As shown in Figure 4.14b, the four true HRFs have different peak timings and the amplitudes. The simulation here was to see whether the HRF modeling method could distinguish them and give an unbiased estimate.

Using the simulation data, we applied five HRF modeling methods and plotted their estimates. The four methods in HRF modeling are *transfer function estimate* (TFE), *3dDeconvolution* (AFNI), *smooth finite impulse response* (sFIR), *inverse logit* (IL), and *SPM canonical HRF* (SPM). For the consistency study, we simulated 200 face data sets, applied the four methods for each set, and drew the 200 estimates in one plot.

TFE estimates (Figure 4.15a) show consistency in estimating the HRF by looking at the 200 estimates. We will prove its asymptotic property later. The 200 estimates do not show large variation, but we see the zig-zag on the upper and lower boundaries. To improve the individual TFE estimates, we smoothed each HRF estimate from TFE through LOESS, which is a classic local regression method. The LOESS-smoothed TFE estimates are shown in Figure 4.15b. Compared to Figure 4.15a, the HRF individual did show a smoother estimate, and the consistency still keeps.

Figure 4.16a illustrates the performance of 3dDeconvolution methods in the neuroimaging software AFNI. It is an ordinary linear regression method to estimate HRF

by specifying the length of HRF. Compared to TFE, it has more variation in the HRF estimates. Additionally it has bias in the average estimate.

SFIR is similar to AFNI with penalty on the smoothness.. Figure 4.16b illustrates the performance of sFIR. It captured each shape of the four HRFs but might not be able to distinguish them very well. For each HRF, its estimates are biased. The reason sFIR could not capture the exact shape of each HRF might be due to the comparably large number of types of stimulus involved in the simulation and/or its fixed smooth penalty for any kinds of HRF.

Figures 4.17a and 4.17b are the results from IL and SPM. Both of them are basis function method, which means their results are the linear combinations of their basis functions. For instance, IL's estimates belongs to the Inverse Logit family, and SPM's estimates, to the Gamma family. As the true HRF was not included in any of the two families, their results were biased.

Based on the simulation results of the five methods, TFE was the method that conducts more unbiased and efficient estimate. If the data is too noisy, smoothing the individual HRF is the strategy to use for a more efficient and unbiased estimate.

## 4.7 Advantages of TFE

The TFE, based on the method of Bai et al. (2009), complete the fMRI data analysis procedure: from adapting to various experimental design, through estimating HRF, to detecting the activation region.

The first benefit is the experiment design. TFE can be applied for any type of experimental design, including multiple stimulus design, event-related design, and block design. Our nonparametric method can be applied to the multiple stimulus experiment paradigm. From the property of HRF, different stimuli may cause different hemodynamic responses even in one specific region. Consequently, the corresponding

HRF estimates to each stimulus will be given in our method, and furthermore we carry out the statistical testing to see whether they are equivalent to each other.

Our method can also be applied to block design and some rapid event-related design. Most of the existing HRF estimation methods are only applied to event-related design. With our method's adaptability to various experimental design, we extended the application to rapid event-related design and to block design by adding an extra rest period. In fact, as long as there is a resting period during the design, our method is better in estimating HRF.

The second benefit is reducing the noise. Noises might come from multiple sources, such as the various types of scanners with systematic errors in use, the background noise in the environment, and differences in the individual subjects' heart beats and breathing. These noises would lead to heterogeneity of the records of fMRI data. By using TFE, the heterogeneity is considered in the frequency domain, which simplifies the error structure estimation process. Such simplicity comes from the asymptotic independence of the spectrum in different Fourier frequencies when we transfer the time series analysis to the frequency domain. In addition, for efficiency, we use the WLS method to estimate the error spectrum. Unlike the existing work (Zhang et al., 2007; Brillinger, 1981) based on the WLS method, which is implemented by a computationally costly high-dimentional-matrix operation, our method shows higher performance, since the dimension of our matrix operation depends only on the number of stimulus types in the experiment design.

The third benefit is HRF estimation. TFE does not require the length of HRF, which is also called the latency (width) of HRF. As in most HRF modeling methods, the length of HRF is the input as a *priori* to start the analysis. In practice, however, the latency of HRF is unknown for the researchers. If the length of HRF is assumed as known, such as in smooth FIR or the two-level method in Zhang et al. (2007), the

final result may be very sensitive to the input lengths. For TFE, the latency of HRF is not a factor that affects the estimates. Additionally, the TFE estimates gives us a rough idea about the latency of HRF by looking at how the estimates go to zero eventually over time.

One of the most important benefits is that TFE is able to generate the brain activation map without using the general linear method (GLM). In fact, it simplified the analysis by reducing the number of steps from two to one. The typical fMRI analysis (SPM, FSL) requires two steps to customize HRF in the analysis. The first step estimates HRF, and the second step applies the GLM to study the detection of activation. In TFE, however, activation detection is generalized by testing the hypothesis for the HRF estimates, which does not require additional GLM.

Also, the unique feature of using TFE is being able to test the linearity assumption. As the linearity assumption is the foundation of the convolution model we used, our method is able to test its validity before estimation, which is definitely important for further analysis. As the linearity assumption is valid for the fMRI data after testing, we are then able to use our nonparametric method to perform the analysis, or any analysis tool based on the linearity assumption. If the linearity testing fails, nonlinearity dominates the fMRI data, and the nonlinear estimation method might be used (Friston et al., 1998b; Vazquez and Noll, 1998; Glover, 1999).

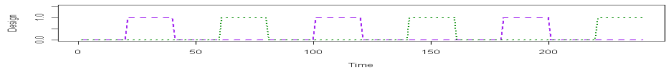


(a) Block design

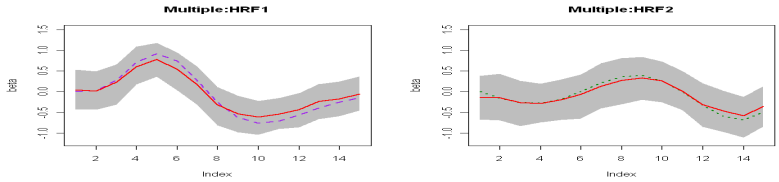


(b) Glover vs $\sin(x)/x$

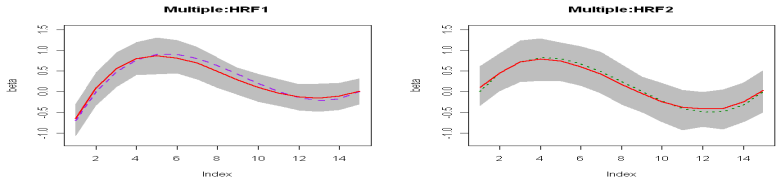


(c) Two cubic functions

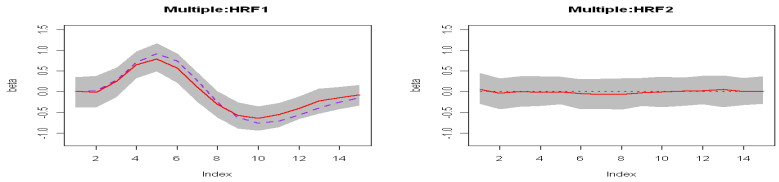


(d) Glover vs 0

Figure 4.2: The multivariate HRF estimation from the regular block design. (a) shows the experiment design paradigm, in which two types (shown in green and purple dashed lines respectively) of stimuli were involved. (b) (c) and (d) are HRF estimates from three different simulation situations: different HRFs , similar HRFs, and the one with no response. The left and right plots show the HRF estimation for green and purple stimuli respectively. The dashed line is the true HRF used in the simulation. The solid line is the mean of estimates from 200 simulations. The gray band shows the 95% interval for the estimates. The result shows the TFE is able to identify multiple HRF shapes simultaneously in an experimental design with multiple stimuli.

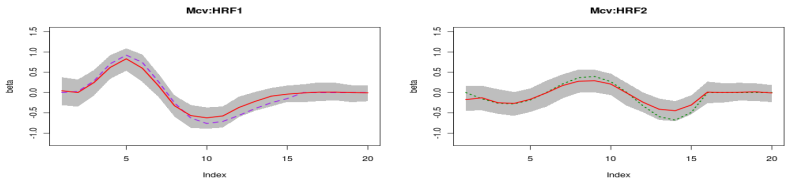


(a) Greater length

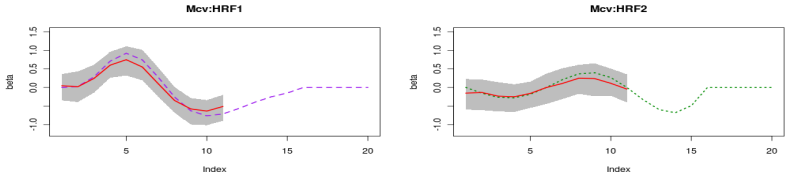


(b) Less length

Figure 4.3: The HRF estimation result of TFE by using different (longer or shorter than the true value) input length. The dashed line shows the true value, and the red solid line shows the average estimates of 200 simulations. As shown by the plots, if the specified length is shorter than the true value, the graph is the truncated version of the longer one. That means, the input length of HRF does not affect the final estimates in TFE.

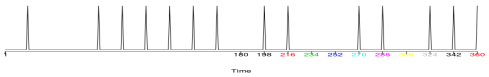


(a) Random event-related design

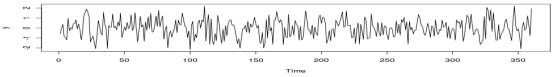


(b) Simulated time series with low SNR

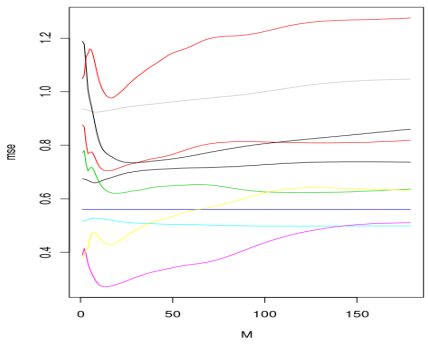


(c) 10 rounds of cross validation

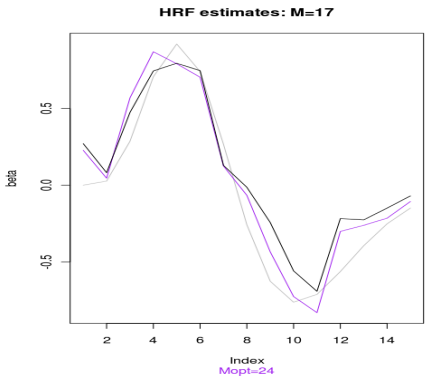


(d) HRF estimates

Figure 4.4: The MCV simulation study on one random event-related design. (a) shows the stimulus function of the experimental design. (b) shows the simulated signal with high level of noise (low SNR). (c) shows 10 RMSE values obtained by using the possible values of the smoothing parameter $M$ in 10 training sets (its color corresponds to the subinterval indicated in (a)). There are three functions shown in (d): the gray line is the true HRF in the simulation; the black line is the estimated HRF by using the smoothing parameter $M = 17$ given in MCV; the purple line is obtained by using $M_{opt} = 24$ which minimizes the total MSE in Section 4.3. Even with high level of noise, by using MCV we obtain the smoothing parameter to the optimized one.

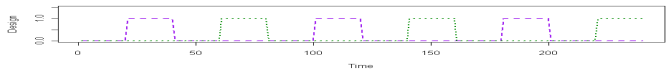


(a) Block design

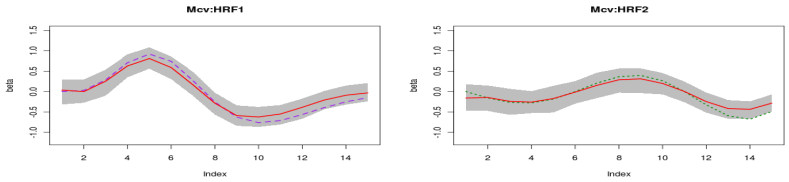


(b) Glover vs $\sin(x)/x$

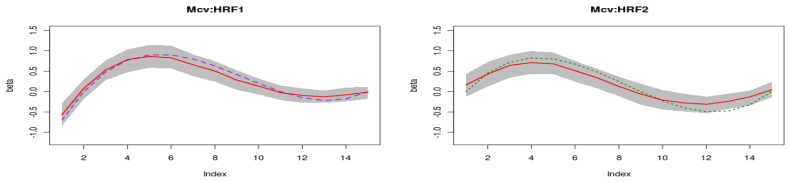


(c) Two cubic functions

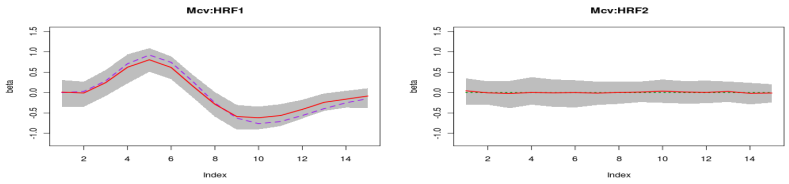


(d) Glover vs 0

Figure 4.5: The multivariate HRF estimation from the regular block design by using MCV. This is the same simulation as shown in Figure 4.2. The only difference between the two figures is the usage of different smoothing parameters. Comparing the two figures, we can clearly see that MCV reduces the estimation variation.

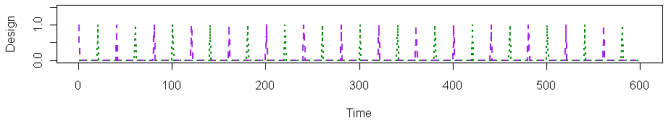


(a) Event-related design

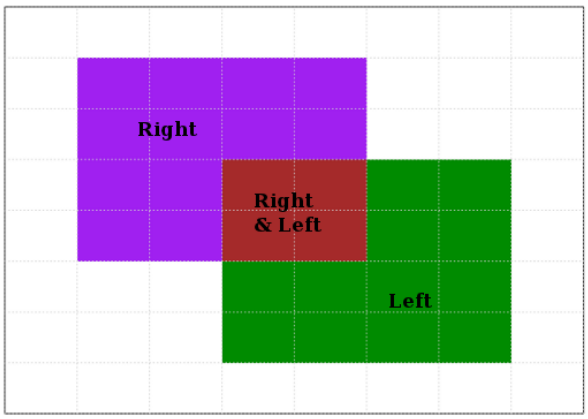


(b) Simulated brain map.

Figure 4.6: The simulated brain map in Simulation 4. (a) shows the experiment design of the simulation with two kinds of stimuli, which are finger taping on the right (shown in purple) and on the left (shown in green). (b) is the simulated brain map: the purple region only responds to the right-hand stimulus; the green region only responds to the left-hand stimulus; the brown region responds to both left and right; and the white region has only noise.

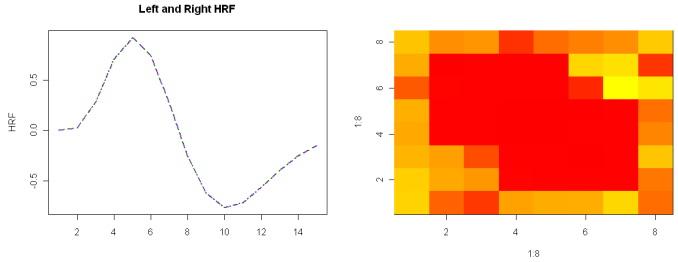


(a) HRF (b) Coherence

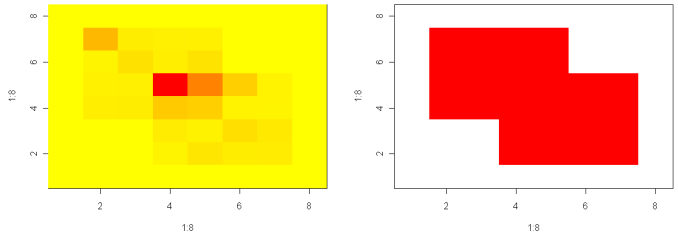


(c) $F$ statistic (d) Activation region

Figure 4.7: Detecting the activation regions by TFE. The activation region is where the brain has response to the experiment stimulus. (a) shows that the true HRFs for both left and right are the same. (b) shows the coherence value obtained in voxels (the red color means high intensity, and the yellow indicates low intensity). (c ) shows the corresponding $F$ statistic, called $F$ map. As shown in (d), both right and left activated regions (marked in red) are detected.

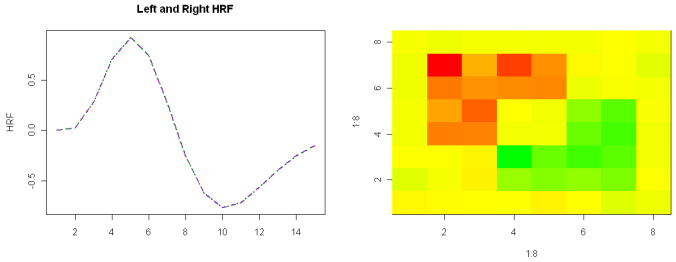


(a) HRF (b) $t$ statistic

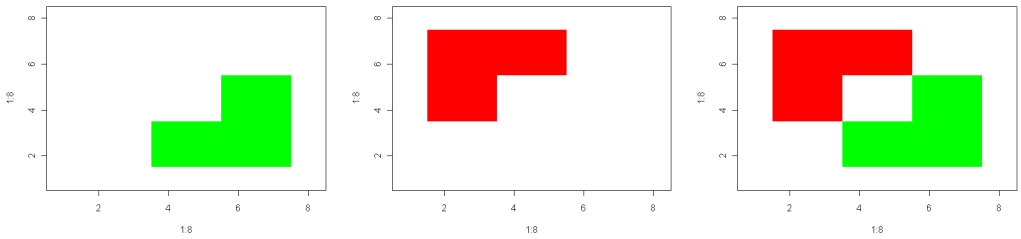


(c) Acceptance region: L>R (d) Acceptance region: L<R (e) Acceptance region: L≠R

Figure 4.8: Hypothesis testing with two identical HRFs in the simulated brain. (a) shows the Glovers HRF for both left and right. (b) shows the overall t statistic over the brain map, where red color means high positive values, green color means negative values, and yellow means near 0. (c) shows the rejection region for the test: left≤right; (d) shows the rejection region for left≥right; (e) shows the rejection region for left=right.

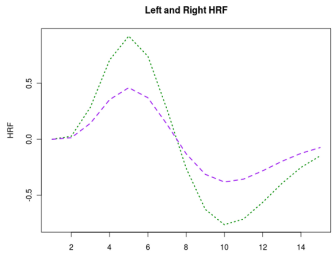


(a) Left and Right HRF

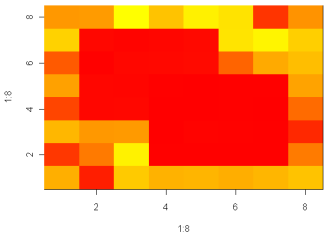


(b) Coherence

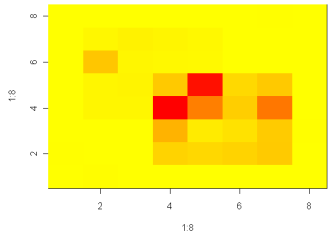


(c) $F$ statistic

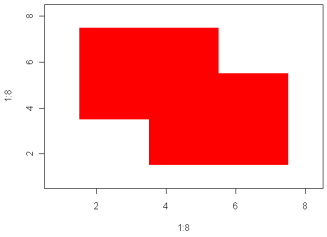


(d) Activation region

Figure 4.9: Detecting the activation regions by TFE with non-identical HRFs. The activation region is where the brain has response to the experiment stimulus. (a) shows the true HRFs for both left (green) and right (purple). (b) shows the coherence obtained in voxels (the red color means high intensity, and the yellow indicates low intensity). (c) shows the corresponding $F$ statistic, $F$ map. As shown in (d), both right and left activated regions (marked in red) are detected.

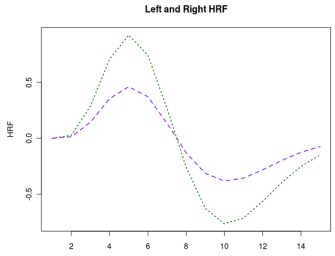


(a) Left and Right HRF

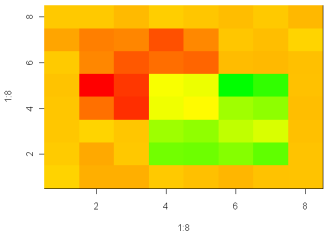

(b) $t$ statistic

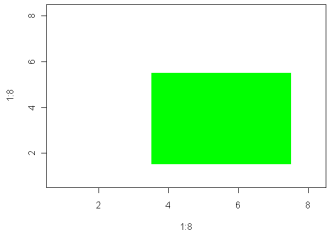

(c) Acceptance region: L>R

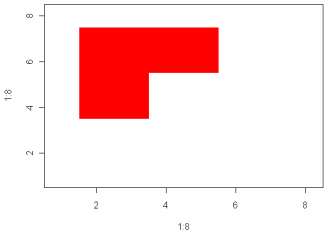

(d) Acceptance region: L<R

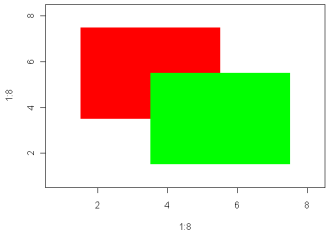

(e) Acceptance region: L≠R

Figure 4.10: Hypothesis testing with two non-identical HRFs in the simulated brain. (a) shows the Glovers HRF for left (green) and half Glovers HRF for right (purple). (b) shows the overall t statistic over the brain map, where red color means high positive values, green color means negative values, and yellow means near 0. (c) shows the rejection region for the test: left≤right; as the left HRF has much higher amplitude than the right one, the rejection region for the test left≤right is the two regions that response to left-hand stimulus. (d) shows the rejection region for right≥left; (e) shows the rejection region for left=right.

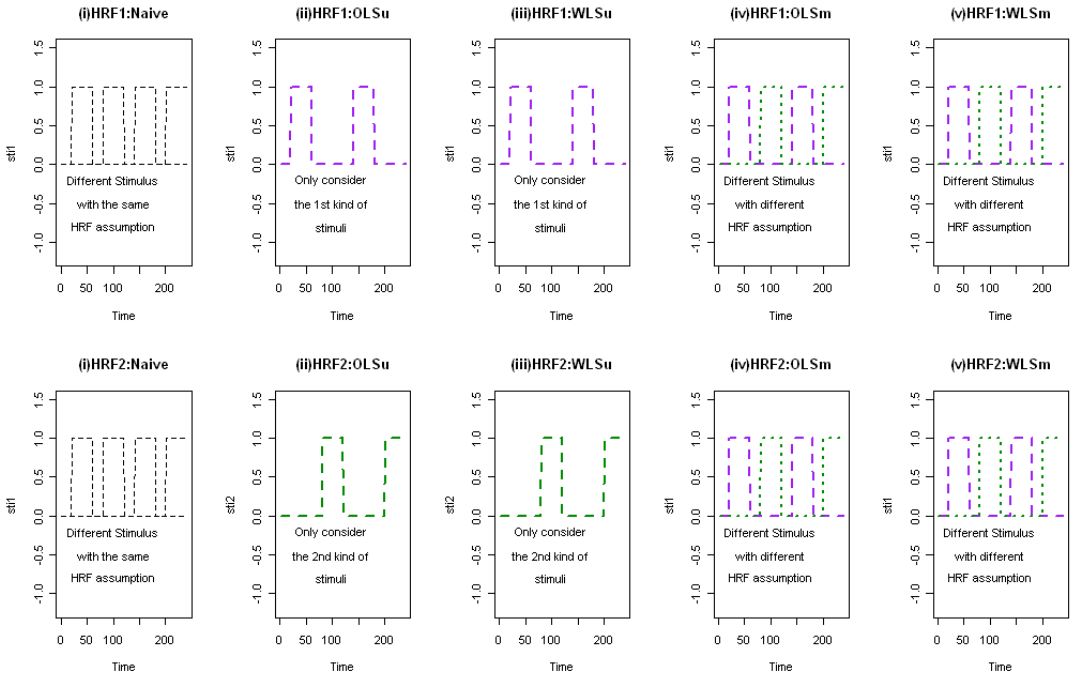


Figure 4.11: The experimental design for the five-method comparison. This is the plot arrangement for Figure 4.12 - 4.13. The five columns indicates five different methods: Naive, OLSu, WLSu, OLSm, WLSm, respectively. The two rows are for two types of HRFs respectively.

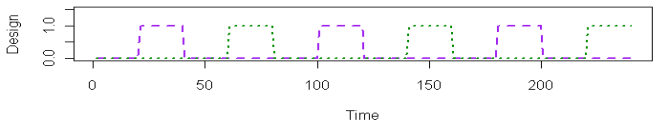


(a) Block design

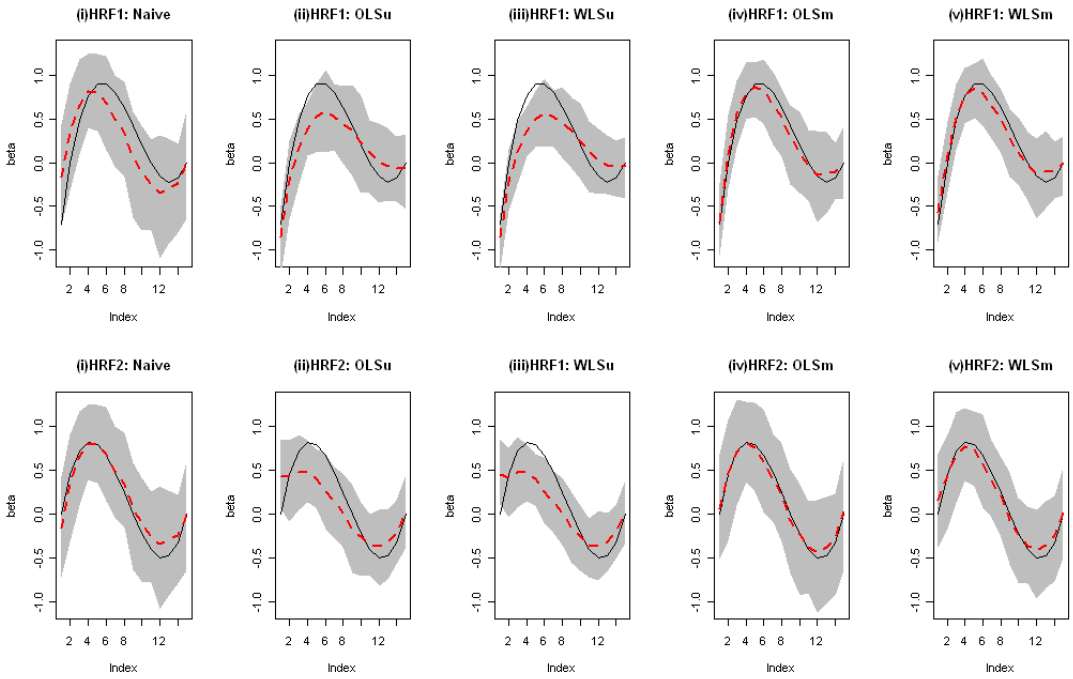


(b) Simulation result

Figure 4.12: HRF estimates from typical block design. The multivariate method using WLS has substantially reduced the bias associated with the univariate method in both HRFs estimate.

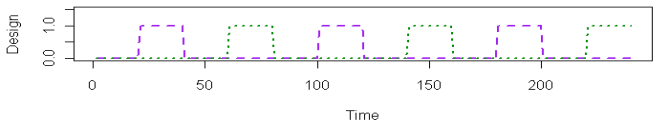


(a) Block design

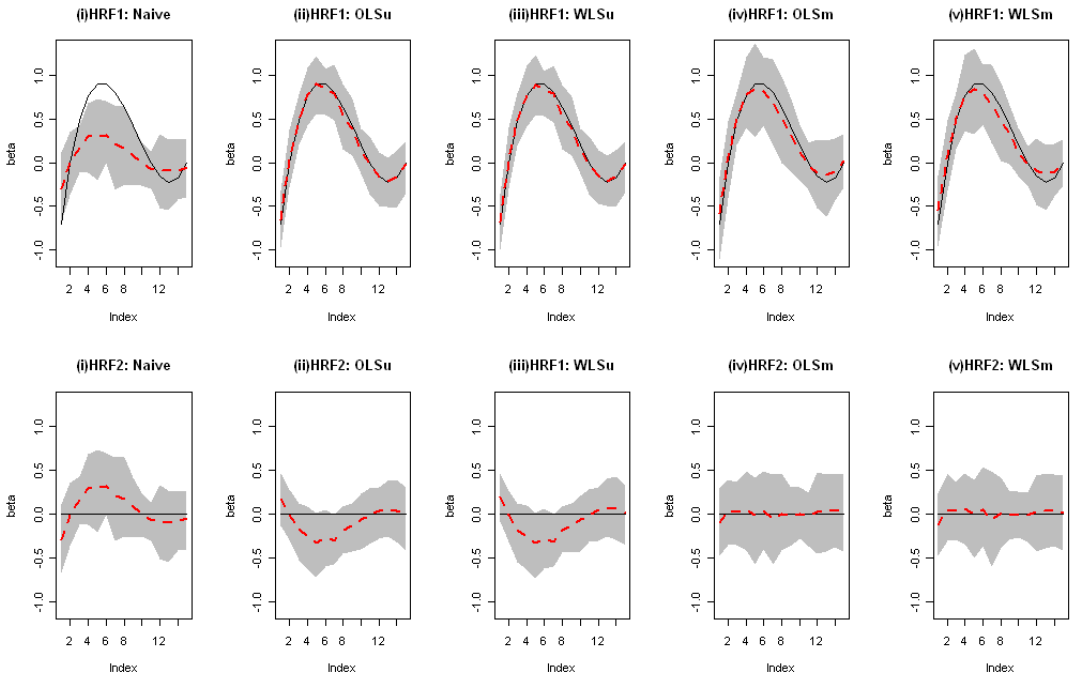


(b) Simulation result

Figure 4.13: HRF estimates from the simulation that only show response to one of the stimuli in block design. The multivariate method demonstrates its robustness by giving consistent estimate.

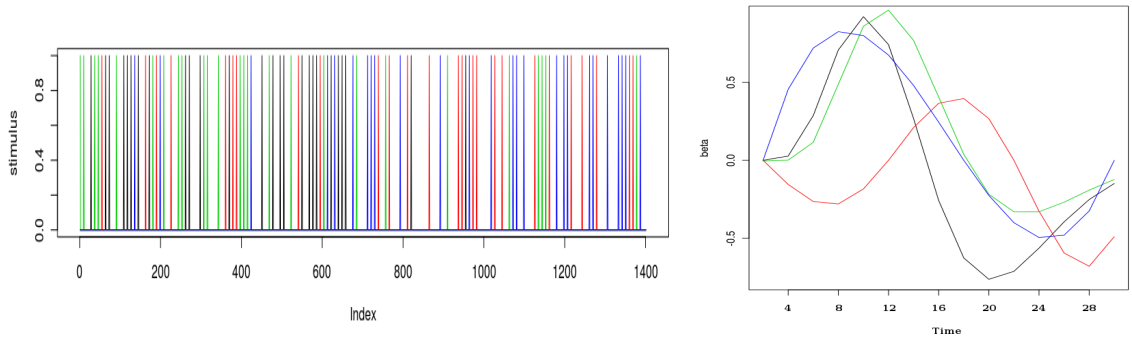


(a) face data design

(b) True HRFs

Figure 4.14: Face data design. There are four event-types of interest; the first and second presentations of non-famous and famous faces, which we denote as N1 (in black), N2 (in red), F1 (in green) and F2 (in blue), respectively. (a) shows the timing of the events in the experiment, and (b) shows the respective True HRFs, with which we will compare the estimate results in Figure 4.15, 4.16 and 4.17.

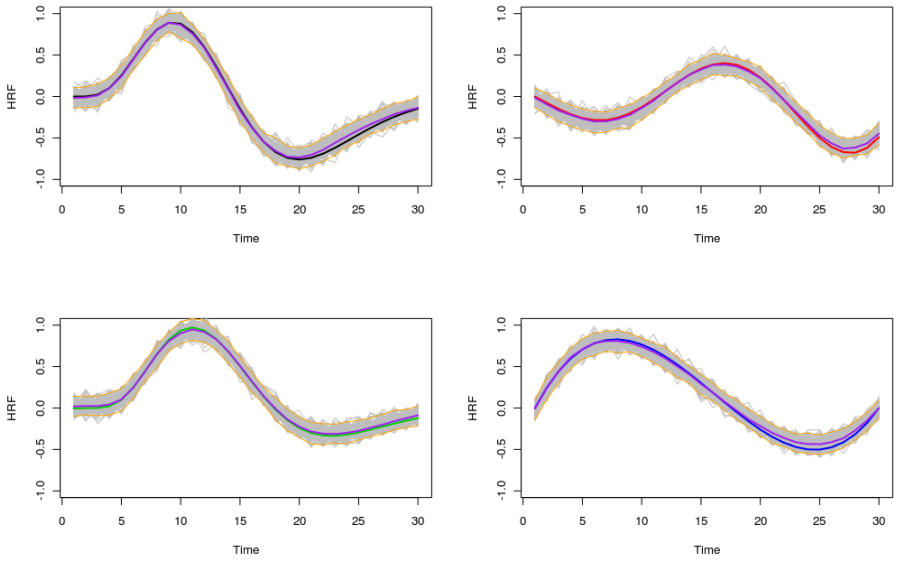


(a) TFE estimates

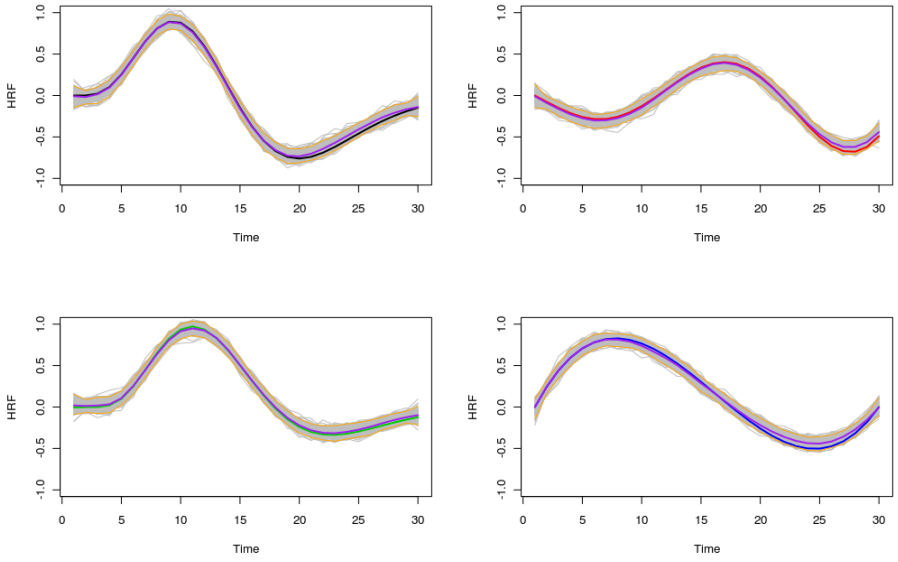


(b) TFE estimates after loess

Figure 4.15: TFE estimates of 200 face data simulations for the experiment shown in Figure 4.14. The 200 TFE estimates are gray lines, and the average of them is purple. The true HRF of four different events shows in color (black, red, green, and blue in respective plots). There are two thin orange lines close to the upper and low boundaries indicating the 95% confidence band. You may not see the average line clearly if the average fits the true HRF very well.

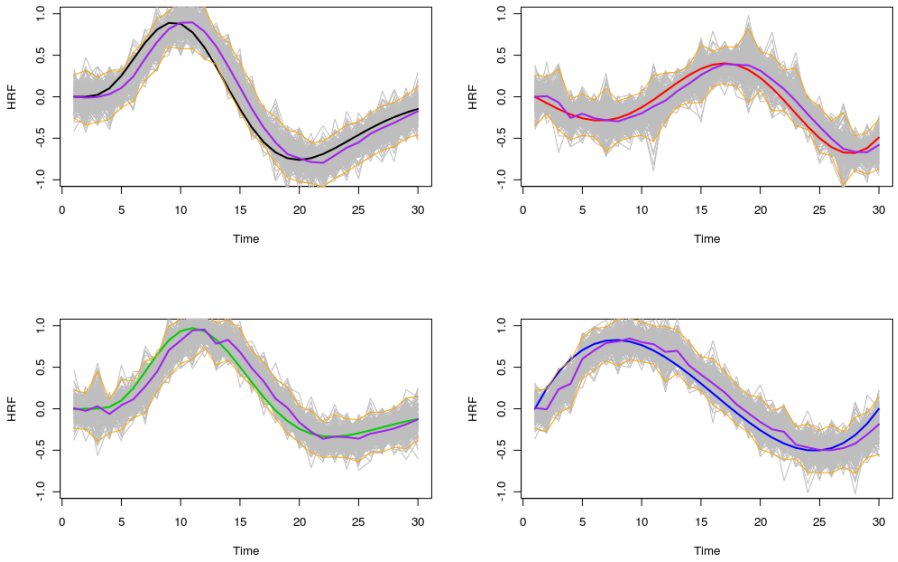


(a) AFNI estimates

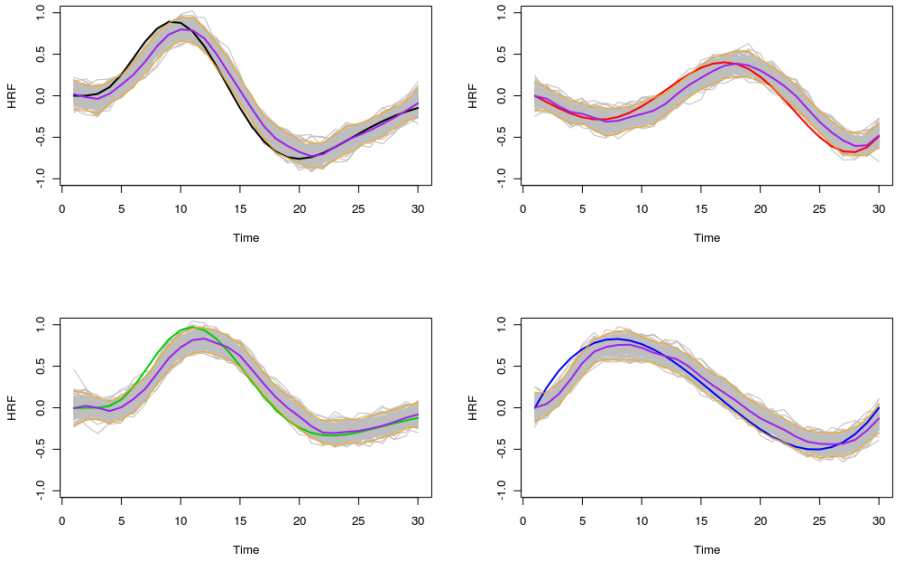


(b) sFIR estimates

Figure 4.16: AFNI and sFIR estimates of 200 face data simulations for the experiment shown in Figure 4.14. The 200 TFE estimates are gray lines, and the average of them is purple. The true HRF of four different events shows in color (black, red, green, and blue in respective plots). There are two thin orange lines close to the upper and low boundaries indicating the 95% confidence band.

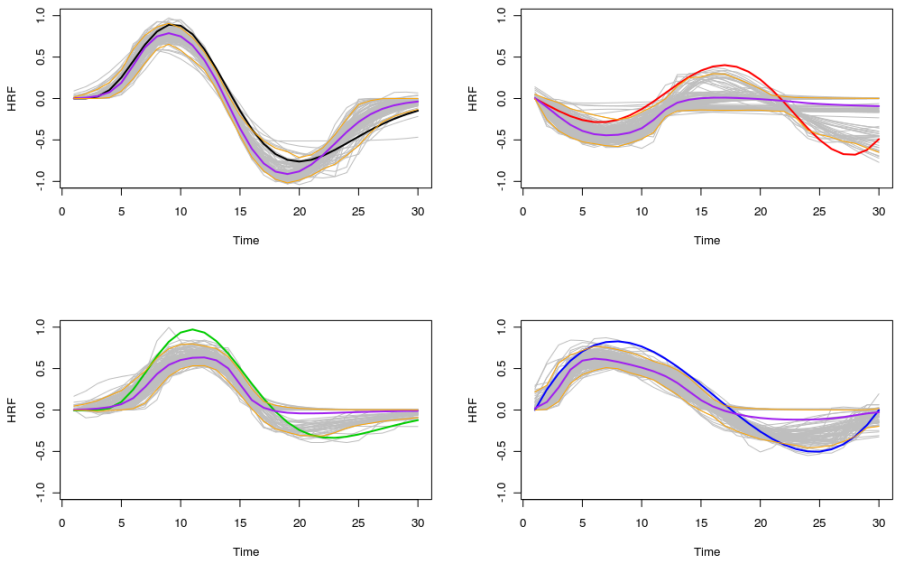


(a) Inverse logit estimates

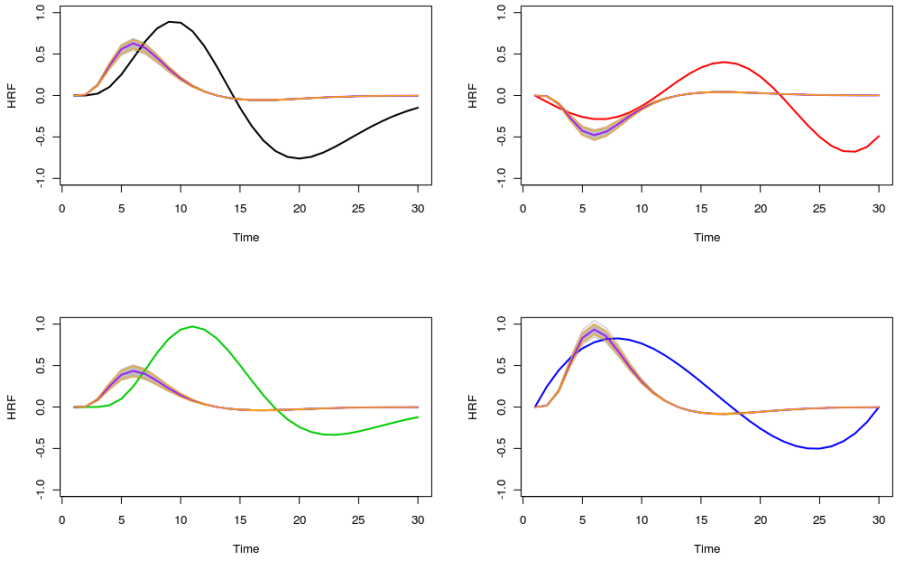


(b) SPM Cannonical HRF estimates

Figure 4.17: Basis function estimates of 200 face data simulations for the experiment shown in Figure 4.14. The 200 TFE estimates are gray lines, and the average of them is purple. The true HRF of four different events shows in color (black, red, green, and blue in respective plots). There are two thin orange lines close to the upper and low boundaries indicating the 95% confidence band. IL and SPM are two of the basis function methods, which has their own basis function family. If the true HRF does not belongs to the family, the estimates are biased.

# Chapter 5

# Real Data Application

We apply the nonparametric HRF modeling method to four data sets: auditory data, finger-tapping data, face data and event-related visual data.

## 5.1 Detecting Activation in Auditory Data

In order to test whether the method of Bai et al. (2009) is applicable to real data and detect fMRI activation, we applied the nonparametric method to the published auditory data set on the Statistical Parametric Mapping website (`http://www.fil.ion.ucl.ac.uk/spm/data/auditory/`). According to the information listed on the website, these whole brain BOLD/EPI images were acquired on a modified 2T Siemens MAGNETOM Vision system. Each acquisition consisted of 64 contiguous slices (64x64x64 3mm x 3mm x 3mm voxels). Acquisition took 6.05s, with the scan to scan repeat time (TR) set arbitrarily to 7s. During the experiment 96 acquisitions were made in blocks of 6 that resulted in 16 42-second blocks. The blocks alternated between rest and the auditory stimulation. We included 8 trials in our dataset, with the first 6 images acquired in the first run discarded due to T1 effects. The data was preprocessed using SPM5, and included realignment, slice timing correction, coregistration, and spatial smoothing.

Figure 5.1a shows the time course data from the one voxel that had the greatest F value in equation (2.2.14). The voxel time series depicted in Figure 5.1a has been

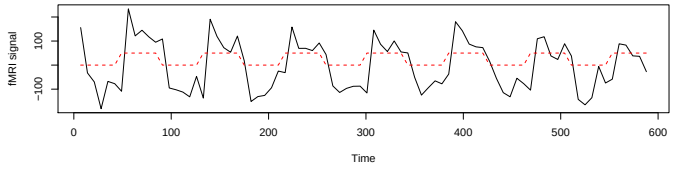


(a) Auditory data and its design

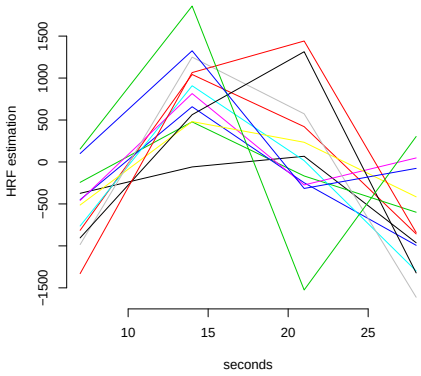


(b) HRF estimation

Figure 5.1: HRF estimation for auditory data. (a) is the experimental design paradigm (the red dashed line) for the auditory data. The solid line is fMRI response from an activated voxel over time; (b) is the HRF estimates from the 12 highly-activated voxels found by using TFE in the brain. Due to the large TR (7s), there is a limitation on showing the HRF estimate in finer temporal resolution. In (b), we still can see the different shapes of HRF.

detrended as suggested by Marchini and Ripley (2000) because the trends may result in false-positive activations if they are not accounted for in the model. Since the voxel has a high F value, its time series has a good relationship to the task, similar to the pattern we obtained in our second simulation. Figure 5.1b shows several HRF estimates from the 12 voxels with the highest F-values. The majority of the HRF estimates closely match the HRF shape, showing the increase in the signal that corresponds to the HRF peak and some even depicting the post-dip after the peak signal. The TR for this dataset is 7 seconds, which corresponds to the time interval between the acquisition of data points. This leads to a very low temporal resolution

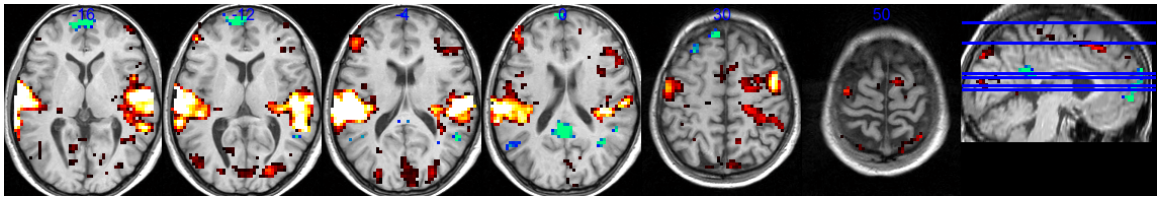


(a) T map

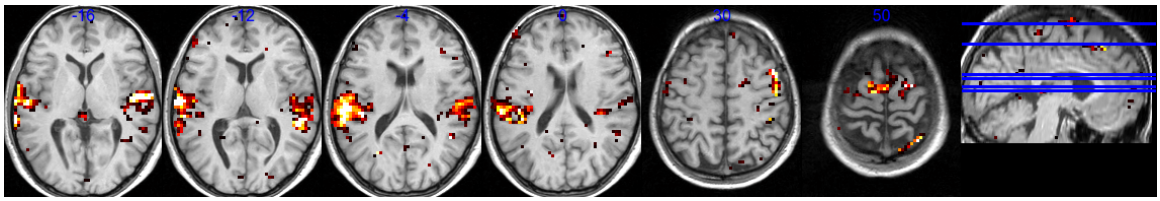


(b) F map

Figure 5.2: F map and T map of the activation by using TFE and SPM. T maps contain blue and hot colors which respectively indicates negative and positive factor. The F map generated by TFE (bottom row) appears to have less noise compared to the SPM-generated T map (upper row).

with which to measure the hemodynamic response. As a result, we could only see the framework of the HRF and approximate its value. Despite this limitation, the resulting framework gave us evidence that our method does indeed capture the various HRFs in the voxels. In addition, it establishes that our HRF-based analysis can be applied to real data and may be improved with correspondingly refined temporal resolution.

In the experimental design of this study, there are 7 stimulus blocks in the time series data that have a total duration of 90 acquisitions. As a result, the task-related frequency is $7/90 = 0.0778$. Using this information, we can apply our method in order to generate an F-statistic map to show the activation in the brain that is triggered by the stimuli (Bottom row in Figure 5.2). For comparison, we also generated a T map using SPM5 (the SPM T map) that is shown in the upper row of Figure 5.2. The SPM T map is a contrast image that obtains the activation triggered by the stimulus by applying the canonical SPM HRF uniformly throughout the brain. As a result, it does not take into account any HRF variation that might occur in the different

regions of the brain.

In both rows of Figure 5.2, increased activation is depicted by increased hot color, such that the bright yellow regions represent more activation. As expected from an auditory study, both the F map generated using our method and the SPM-generated T map display activation in the temporal lobe. The F map from our analysis shows increased activation almost exclusively in the temporal lobe, again as would be expected from an auditory study. Whereas the contrast map generated using SPM also displays the activation in the temporal lobe, there is also significant activation in other regions of the brain, including parietal and prefrontal cortical areas. In addition, the activation in the temporal lobe is more diffuse using SPM compared to that seen using our F method. We conclude that the map generated using our method appears to display less noise, such that there is less activation in regions other than the primary auditory cortex. In addition, our method displayed a less diffuse activation area in the auditory region, which may be interpreted as either a more focused activation pattern or there may be some loss of sensitivity for detecting the actual activation. Despite this possible limitation associated with our method, it does have the additional benefit of being a test for the linearity assumption.

## 5.2 HRF Modeling in Finger-Tapping Data

The study used a modified activation paradigm based on previous studies in control and PD subjects (Lewis, Slagle, Smith, Truong, Bai, McKeown, Mailman, Belger, and Huang, 2007). Briefly, the paradigm consists of sequential finger-tapping movements (SFM) at 0.5 tap/sec using either the right or left hands. The sequences were presented with instructions that first asked the subject to follow the finger sequence presented on the screen during an externally guided training session, and then asked the subject to continue the finger-tapping sequence (internally guided task). Each

SFM block was 60 seconds long, and each block was preceded and followed by a 30 second rest (R) period. Each run consisted of four blocks of rest, externally guided training, and internally guided tasks (total 10 minutes). The finger-tapping sequences of each block were alternative to prevent memorization from previous blocks. All subjects practiced the task with both hands for about 20 minutes prior to scanning in order to obtain adequate performance on the tasks. The experiment design is in Figure 5.3. Image were acquired using a 3.0 Tesle Siemens scanner. TR is 3 seconds.

We have obtained the preliminary analysis from applying the weighted least squares (WLS) estimation method (Section 3.4) to some data. The data are from a normal subject performing finger tapping under the lab design (Figure 5.3). We estimated HRF corresponding to the right hand stimulus in three brain regions: left primary motor cortex (PMC, 398 voxels), left supplementary motor area (SMA, 294 voxels), and right Cerebellum (1254 voxels).

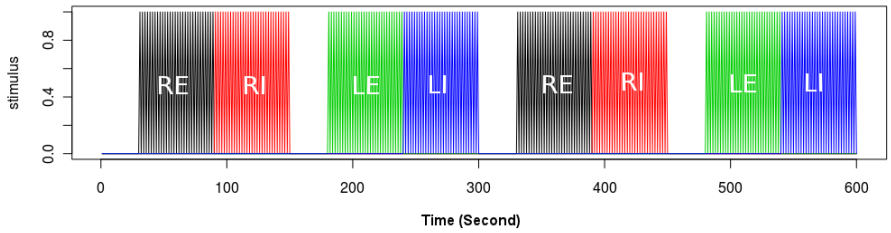


Figure 5.3: Finger-tapping design includes four kinds of stimulus: Right External (RE), Right Internal (RI), Left External (LE), Left Internal (LI). The total design lasts for 10 minutes.

We first preprocessed the region of interest (ROI) data, and used the local linear regression method (Marchini and Ripley, 2000) to remove the trend in the data (Figure 5.4). We then used the F-test developed in Section 3.2 to determine whether a particular voxel in the ROIs is activated by the right-hand finger tapping. Finally, we applied the WLS estimator to the activated voxels to estimate the corresponding HRFs, which are plotted in Figures 5.5 to 5.7, respectively for *left PMC*, *left SMA*,

and *right Cerebellum*.

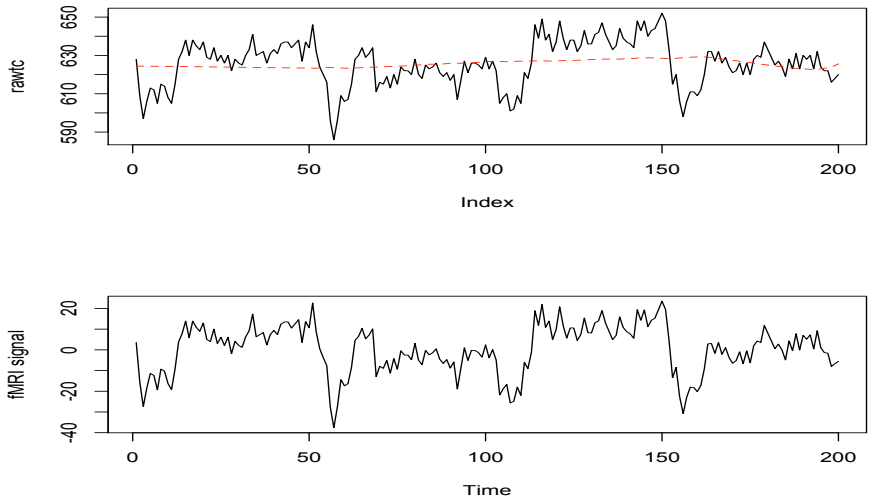


Figure 5.4: The upper time series is the preprocessed data from one voxel in finger-tapping data, and the red dashed line is the fitted trend of the preprocessed time series. The bottom time series is the detrended data which is obtained by the trend deduction from the preprocessed time series in the upper plot.

### 5.2.1 TR Issues

As the HRF estimates shown in left PMC, left SMA, and right Cerebellum, the HRF points estimates is every 2 seconds as TR=2 seconds. In order to the exact HRF triggered by every event, TR is an issue considering the experiment design we have here.

There is a real data analysis issue caused by TR, the repetition time for finishing a whole brain volume scan. As an event shows up every 2 seconds, the fMRI data in one voxel is recorded every 3 seconds. If we still regard stimulus function $x(t)$ and the response $y(t)$ have the same length, that is,

$$x(1), \quad x(4), \quad x(7), \quad \dots$$
$$y(1), \quad y(4), \quad y(7), \quad \dots$$

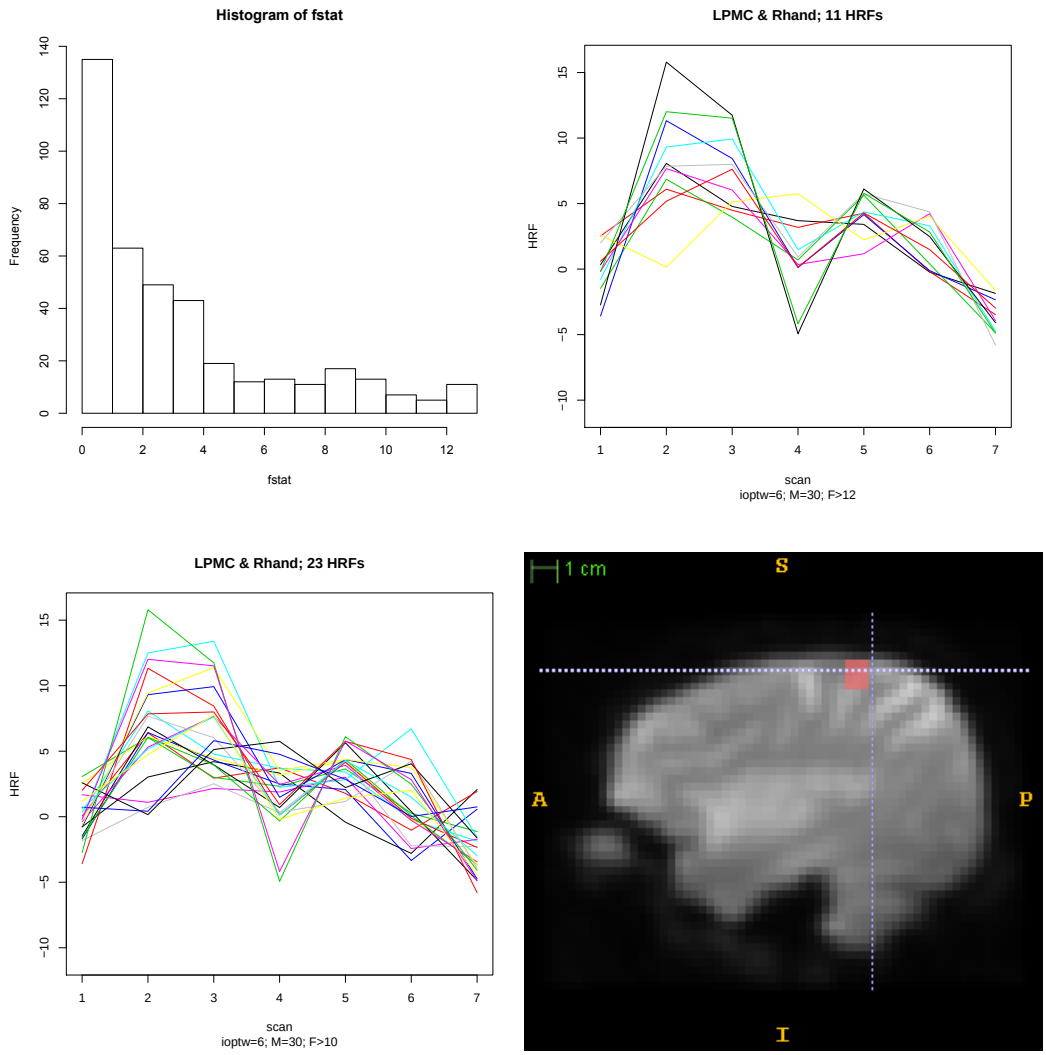


Figure 5.5: TFE in the left primary motor cortex (PMC) from finger-tapping data. (a) shows the histogram for the F-stat in the left PMC. (b) and (c) show the HRF estimates in the activated voxels thresholded at different level as $F > 12$ (b) and $F > 10$ (c) in the left PMC area, and (d) is the sagittal image of the activated voxels with $F > 10$ in the left PMC.

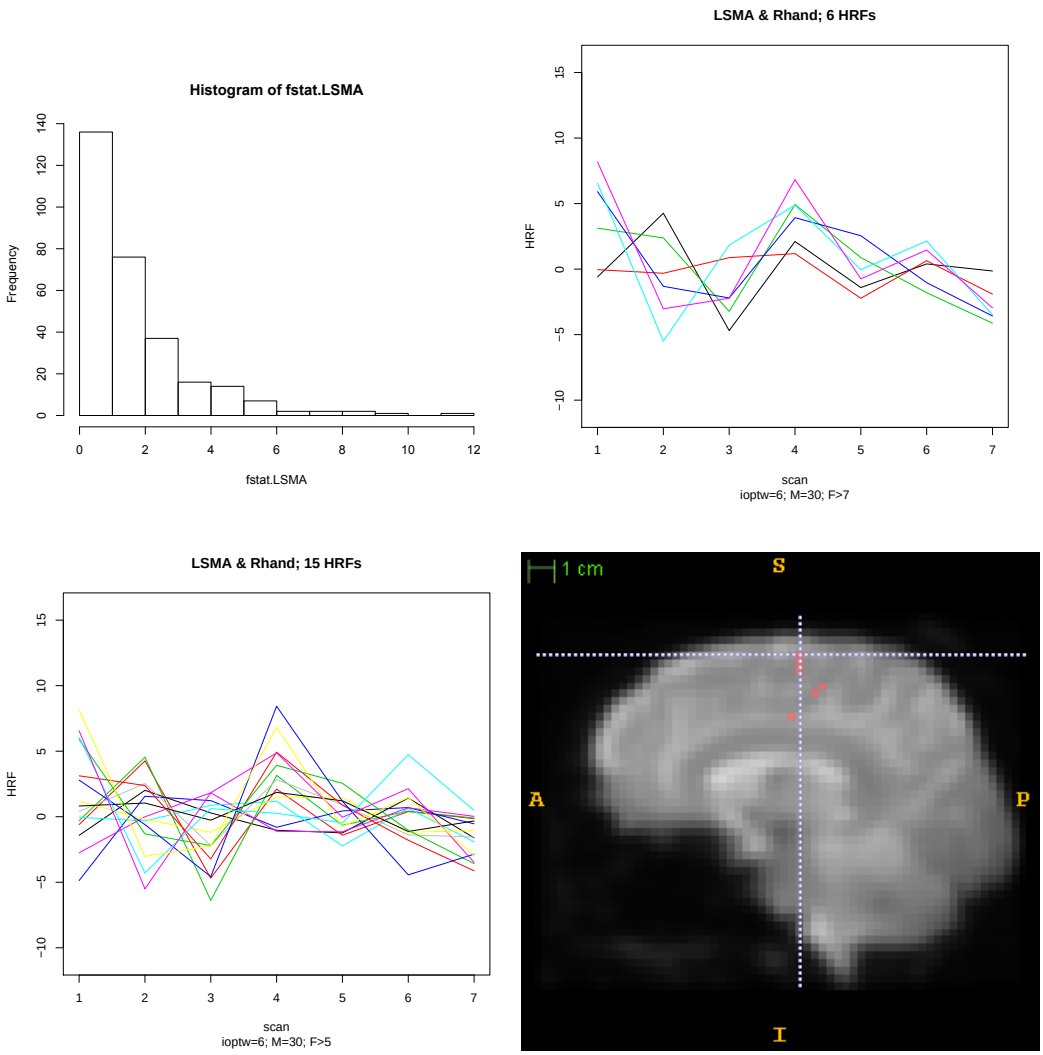


Figure 5.6: TFE in the left supplementary motor area (SMA) from finger-tapping data. (a) shows the histogram for the F-stat in the left SMA. (b) and (c) show the HRF estimates in the activated voxels thresholded at different level as $F > 7$ (b) and $F > 5$ (c) in the left SMA area, and (d) is the sagittal image of the activated voxels with $F > 5$ in the left SMA.

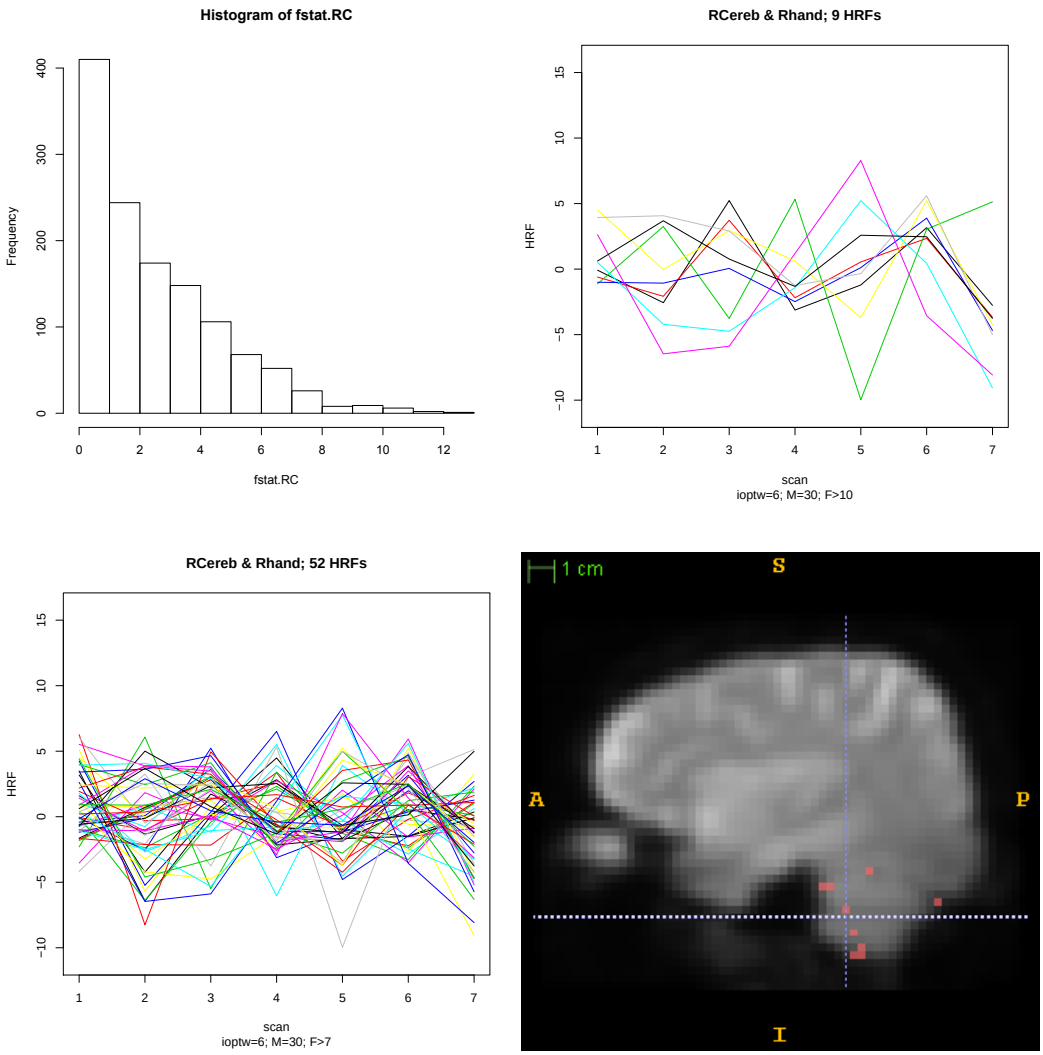


Figure 5.7: TFE in right cerebellum area from finger-tapping data. (a) shows the histogram for the F-stat in right cerebellum. (b) and (c) show the HRF estimates in the activated voxels thresholded at different level as $F > 7$ (b) and $F > 5$ (c) in the right cerebellum, and (d) is the sagittal image of the activated voxels with $F > 5$ in right cerebellum.

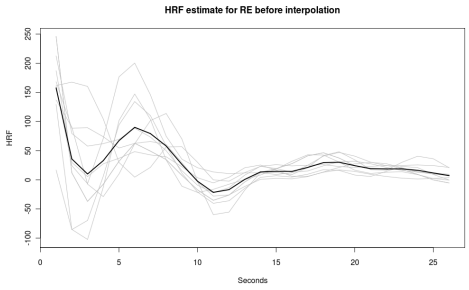


(a) HRF estimate for RE before interpolation

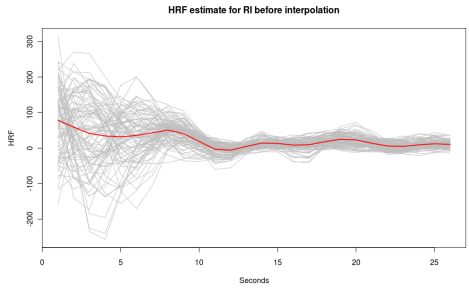


(b) HRF estimate for RI before interpolation

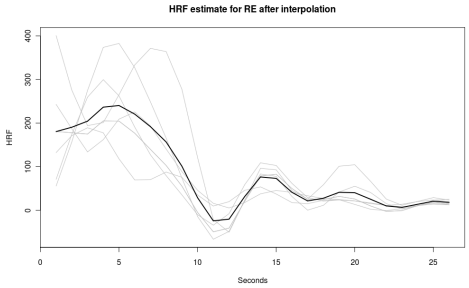


(c) HRF estimate for RE after interpolation

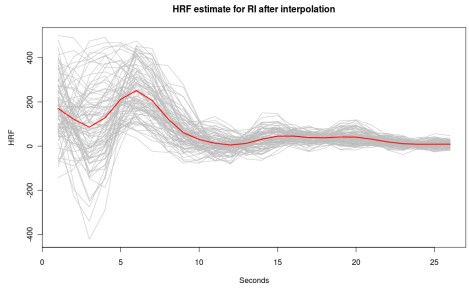


(d) HRF estimate for RI after interpolation

Figure 5.8: The HRF estimates in the activated region of left PMC. The gray line is the HRF estimates from single activated voxels, and the black (RE) and red (RI) lines are the average of the gray HRFs from the activation region. The upper row shows the HRF estimates from the raw time series with incorrect stimulus function. The bottom row shows the HRF estimates from the interpreted time series with correct stimulus function. Notice the significant improvements with the interpolation includes the lower initial value and higher peak amplitudes.

we actually miss $x(3) = 1, x(5) = 1, \ldots$, which leads to the inaccurate estimate of hemodynamic response for a single event.

The way we choose to solve the TR issue is interpolation. In the finger-tapping data set, the event presents for one second, and then we interpolated the preprocessed time series into second basis time series, that is,

$$\begin{array}{ccccccccc} x(1), & x(2), & x(3), & x(4), & x(5), & x(6), & x(7), & \ldots \\ y(1), & y^*(2), & y^*(3), & y(4), & y^*(5), & y^*(6), & y(7), & \ldots \end{array}$$

where $y^*(t)$ is the predicted response at time $t$. There are various interpolating method, and we used the cubic smoothing spline. Simulations have been for the

interpolation strategy we proposed here. After interpolation, the HRF estimates are even smoother and more accurate.

Figure 5.8 shows the HRF estimates before and after the interpolation. We know that the HRF estimates before interpolation are not accurate since the input stimulus function is not the right one. Comparing Figure 5.8a and 5.8b, we see smaller number of activated voxels in right external than internal. Both kinds of HRF have a high initial value in time 0, which is doubted for carrying the missed events. Figure 5.8c and 5.8d give the HRF estimates after implementing the interpolation step. The estimated HRFs start from a lower value, then go up, and slide down for resting. It releases the initial high value and comes up a nicer HRF shape. The peaks of HRF even results higher than before interpolation. So we come to the conclusion that the interpolation strategy is a good way to deal with TR issue discussed in the paper.

As HRF estimates from HRF do not require the length of HRF as a *priori*, through the HRF estimate, we also could figure out that the length of HRF is around 20 seconds for RE and 15 seconds for RI.

### 5.2.2 Brain Map

After the thorough exam in region of interest (ROI), we used the same data set to generate the functional brain map according to two types of stimulus: right hand and left hand. So both RE and RI in the previous study belong to the right-hand task, and the left-hand task includes LE and LI. Then the experiment design is the four-block design with the alternate block presence of right and left hand stimulus.

Using the above experimental setting, activation maps are generated by three methods: TFE, SPM, and FSL in Figure 5.9. From the three maps, all of them has detected Left primary motor cortex as the most significant activation region. But TFE gave more activation area than SPM and FSL.

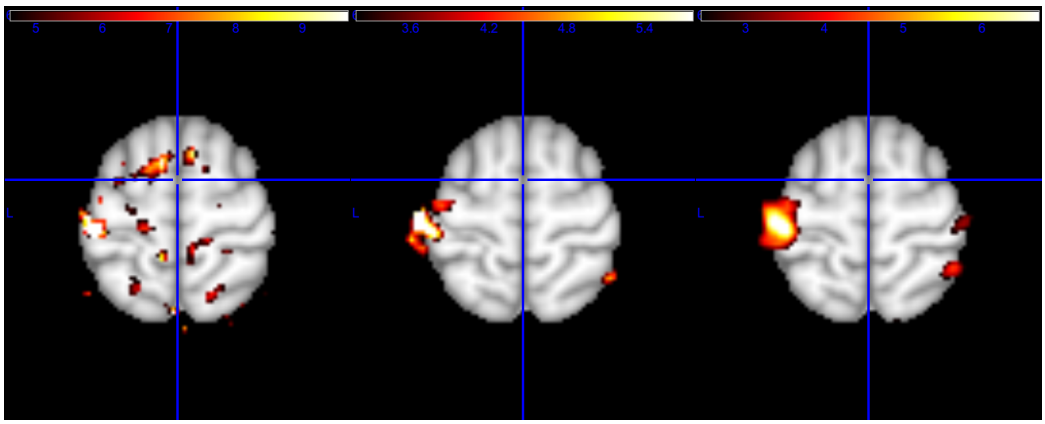


(a) TFE (b) SPM (c) FSL

Figure 5.9: Activation maps of right hand task in the finger tapping data set. The three maps are by TFE, SPM, and FSL respectively at the same slice.

## 5.3 Face Data

The simulation study on face data has been presented in the simulation section with the comparison among several methods, which gave a very positive demonstration on the performance of TFE. Here we present the real data analysis from face data sets (Henson et al., 2002) by using TFE.

It is an event-related experiment design (Figure 4.14a) with four kinds of stimulus: the first and second presentation of famous and non-famous faces (F1, F2, N1, N2). So we regard F1, F2, N1, N2 as four types of stimuli with four HRFs to estimate in the experiment. By using multivariate TFE, HRFs were estimated in the activated voxels after the activation map was generated by testing the hypothesis.

The activation map is first generated by hypothesis testing in TFE. As we show in auditory data, TFE has the ability to spot the activation from single stimulus by using coherence; to deal with multiple stimuli, the corresponding map for each stimulus could also be generated by using partial coherence. Figure 5.10 is the activation map generated by TFE. The activation map is generated by using partial coherence for each stimulus: F1, F2, N1, N2. The hypothesis testing is based on the fundamental

frequency in the experimental design. Thus, the map is actually F statistic brain map. We also provide the activation map generated by SPM (Figure 5.11) for comparison. In general, SPM provide more significant activities than TFE.

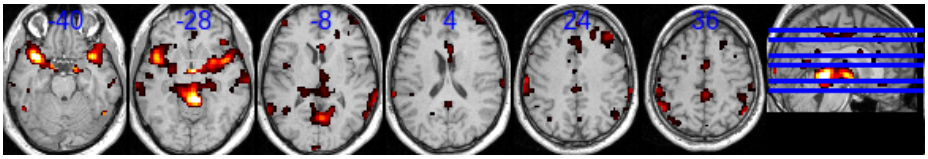


(a) F1 activation

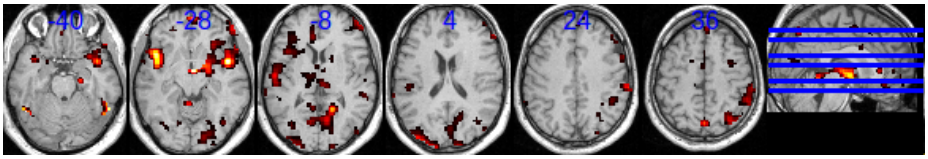


(b) F2 activation

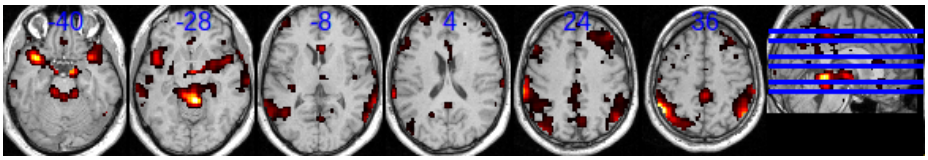


(c) N1 activation

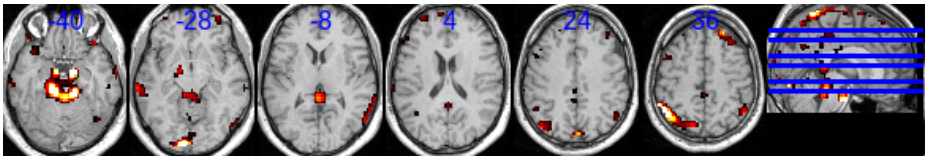


(d) N2 activation

Figure 5.10: The activation map for each stimulus generated by TFE in the face data. (a) First presentation of the famous faces, (b) second presentation of the normal faces (c) second presentation of the famous faces, (d) second presentation of the normal faces.

Then, the HRF estimate from the face data is first conducted in one voxel. The voxel is selected by using the highest t statistic generated in SPM, which denotes the most activated voxel in the brain. Since it has four types of stimulus, so we have four HRFs corresponding to F1, F2, N1, N2 to estimate in this voxel. Additionally we applied two methods, TFE and sFIR, to the voxel time series. Figure 5.12 is the comparison result. The HRF estimates from TFE (Figure 5.12a) give a nice shape of

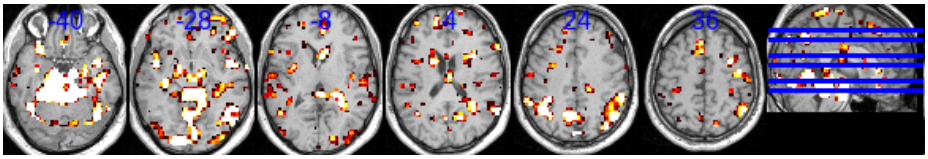


(a) F1 activation

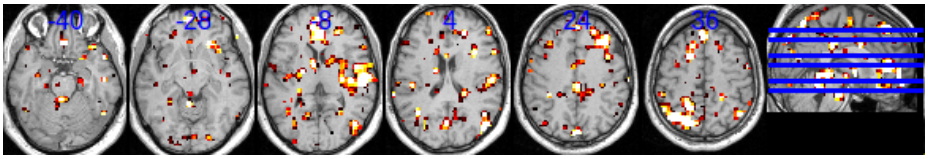


(b) F2 activation

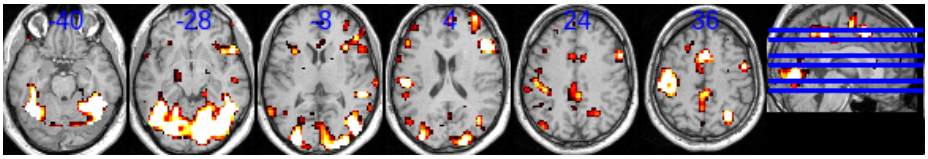


(c) N1 activation

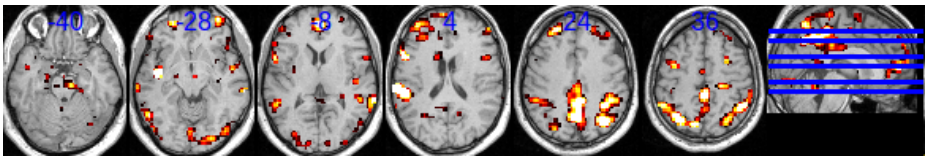


(d) N2 activation

Figure 5.11: The activation map for each stimulus generated by SPM in the face data. The the same types of activation maps as in Figure 5.10, generated by SPM.

HRF which captures the initial peak very well. The HRF estimates from sFIR (Figure 5.12b) have several peaks in the estimates. The possible reason may be due to the aliased HRF. When the events appears in a regular pattern such as the first event and second event always presents in the same inter-trial intervals (ITI), the single HRF estimate may include the second event information which makes the multiple peaks in the result.

## 5.4 Event-Related Visual Data

The data set comes from one control subject under the event-related design 5.13 with pictures showing every 2 seconds. There are four types of pictures included:

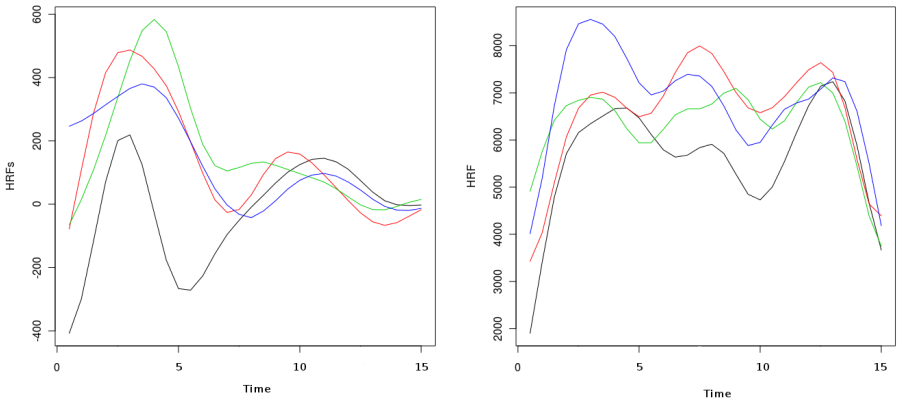


(a) HRF estimates by TFE (b) HRF estimates by sFIR

Figure 5.12: HRF estimates in one voxel. The voxel is selected by using the highest t statistic generated by SPM among the whole brain. TFE gives much better estimation in the tail of HRF than sFIR.

standard, neutral, scary, target circle. The data comes from the paper under review: Hart, Bizzell, Gu, Perkins, Belger (in review) *Fronto-Limbic Changes in Children and Adolescents with Familial High Risk for Schizophrenia.* The standard pictures, regarded as the background instead of stimulus, are the most frequent presentations during the scan session. Thus, three types of stimulus are considered as Neutral, Scary, Target. The whole scanning session included eight runs, and each of them lasts for 4 minutes. TR is 2 seconds. The region of interest (ROI) here is right Amygdala with 38 voxels.

In order to see whether there is activation in Amygdala, we applied both methods, SPM and TFE, to 38 voxels. SPM has t statistic by using the coefficients in the general linear model to detect activation. Figure 5.14 shows no activation detected by SPM. Even though the coefficients are different, the corresponding t statistic is not significant for detecting the activation. Figure 5.15 shows some activation detected by TFE for Neutral and Target stimulus and no activation for Target. The activation is detected by F statistic in TFE by using the task frequency information. For each

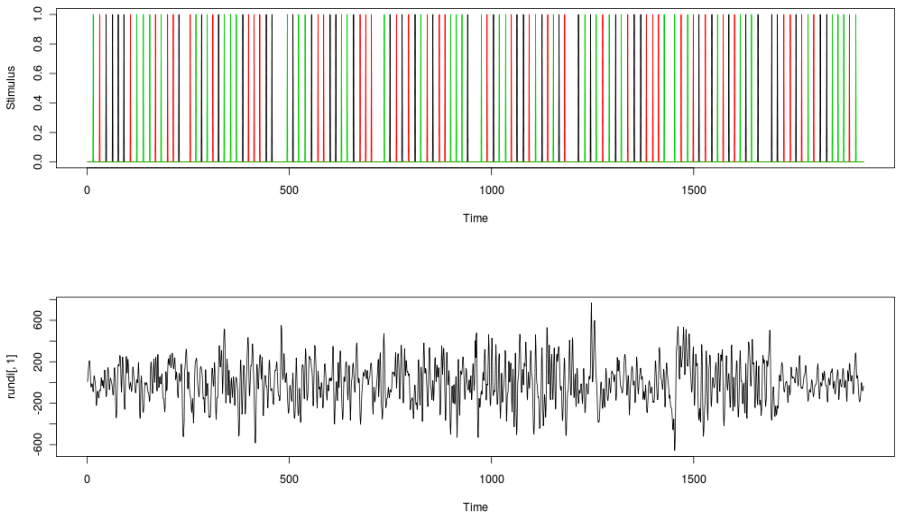


Figure 5.13: Event-related visual data design. The upper graph shows the experimental design with three kinds of events including Neutral (black), Scary (Red), Target (blue). The bottom time series is an example of the fMRI data from one voxel.

single frequency, we used its fundamental frequency and did the hypothesis testing on the frequency to see its activation by voxels. In the 38 voxels, 4 voxels (F values: 7.4, 4.7, 6.3, 4.7) are detected to activate by Neutral and 6 voxels (F values: 5.3, 9.1, 12.5, 7.5, 5.0, 7.5) by Scary. It is confirmed by the researcher exploring the visual fields that Scary evokes more activation than Nautral and also Target has little effect in Amygdala in control subject. Based on the real data, we can see TFE is more sensitive than SPM in detecting the activation based on the frequency information.

The next step is to see the HRF estimates in the activation region. As we already have the activated voxels from TFE, we applied two methods, TFE and sFIR, to estimate HRF in the activated voxels and region. Figure 5.16 shows Neutral HRF estimates by both TFE and sFIR. As they uses the same time series, the HRF estimates can be compared side by side. Both of the HRF estimates have similar shape, but the HRF estimates by TFE have higher amplitude. Figure 5.17 shows Scary HRF estimates by both TFE and sFIR.

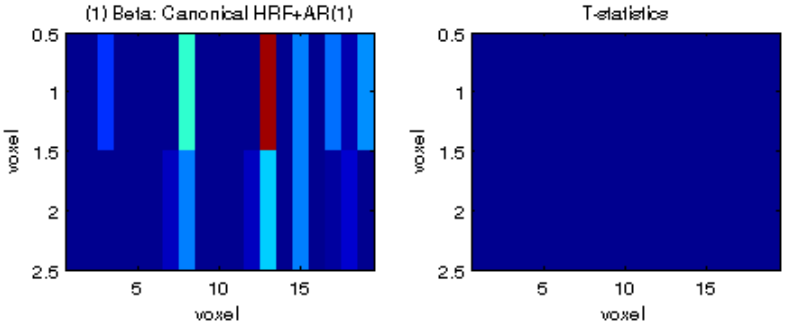


(a) No neutral activation by SPM

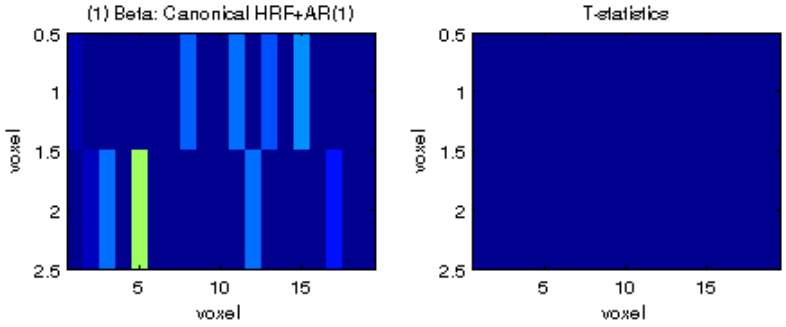


(b) No scary activation by SPM

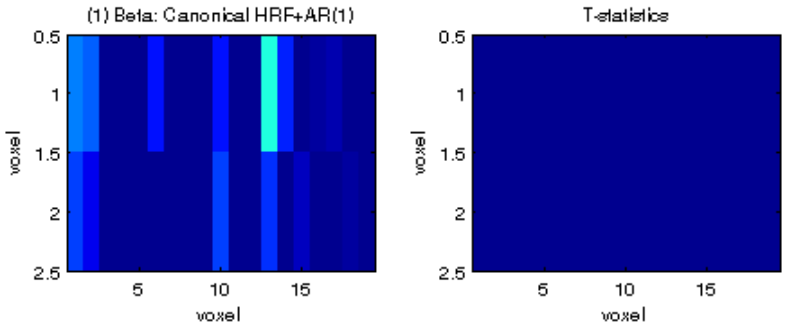


(c) No target activation by SPM

Figure 5.14: The activation detected by SPM in event-related visual data. The value of coefficients in GLM is displayed in $2 \times 19 = 38$ map on the left, and the activation detection is on the right. By thresholding at level 95% of t statistics in SPM, there is no activation detected for either of the three types of stimulus

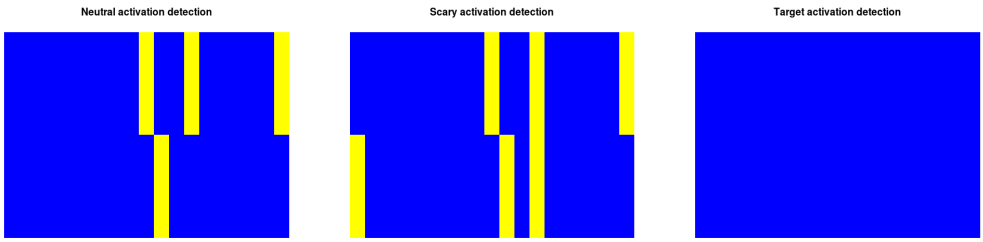


(a) Neutral (b) Scary (c) Target

Figure 5.15: The activation detected by TFE in event-related visual data (the same data as in Figure 5.14). There are activated voxels detected for Neutral and Scary stimulus.

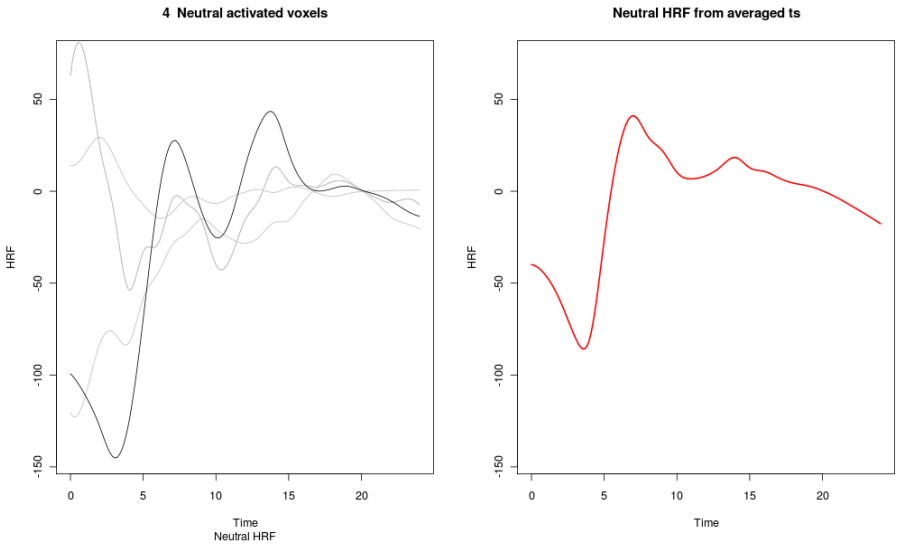


(a) Neutral HRF by TFE

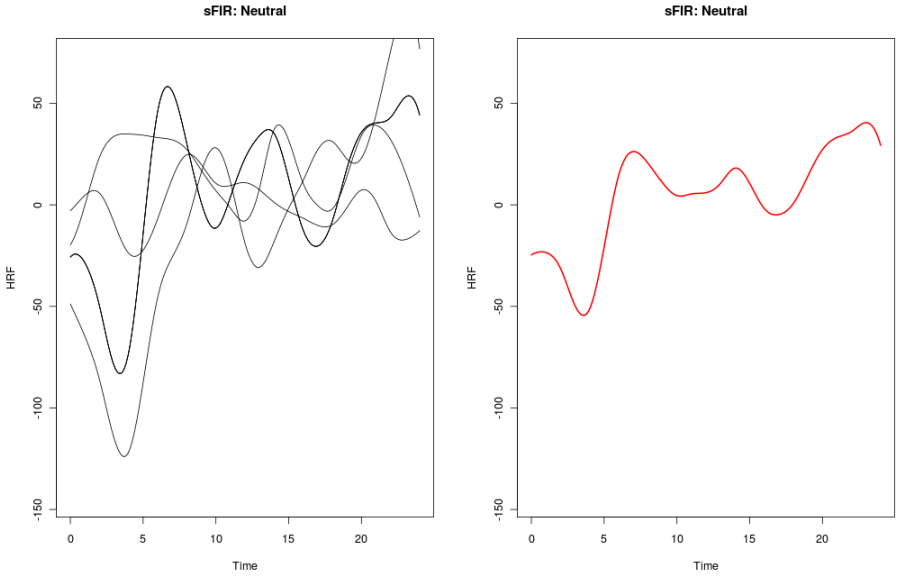


(b) Neutral HRF by sFIR

Figure 5.16: The HRF estimates for the four activated voxels by Neutral stimulus. The upper row is from TFE and the bottom from sFIR. The left graph is the HRF estimates for each voxels, and the right is the HRF estimates by averaging the time series in the four activated voxels. For Neutral stimulus, F-value=7.4, 4.7, 6.3, 4.7 in the four activated voxels. TFE gives smoother estimate in averaged time series than sFIR.

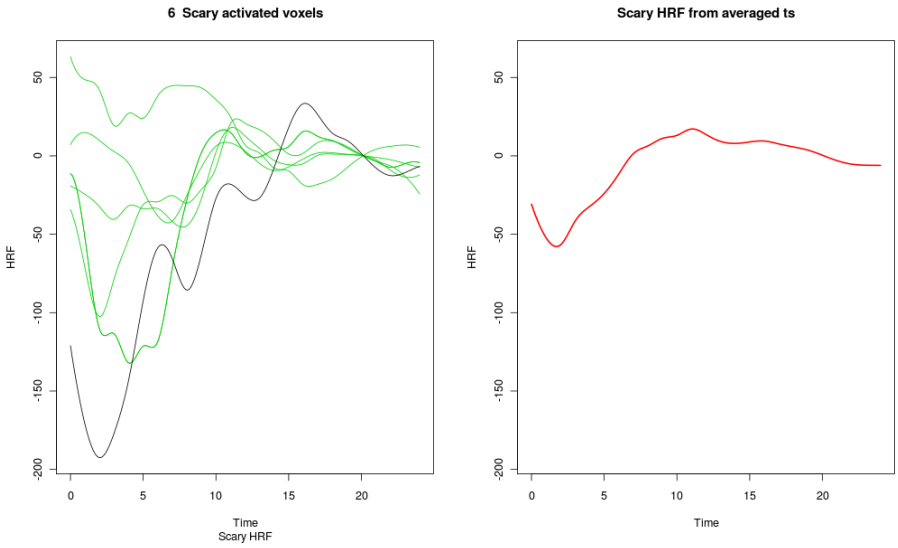


(a) Scary HRF by TFE

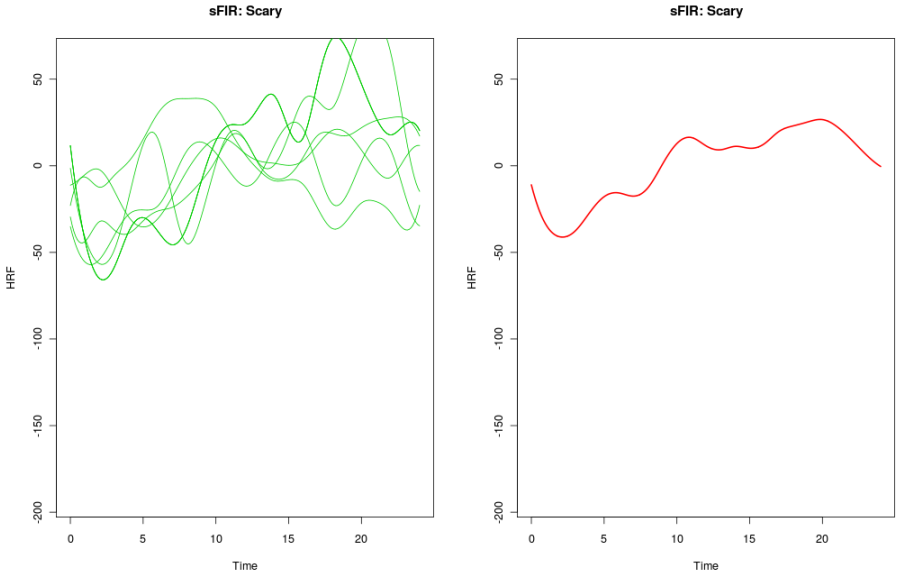


(b) Scary HRF by sFIR

Figure 5.17: The HRF estimates for the six activated voxels by Scary stimulus. The upper row is from TFE and the bottom from sFIR. The left graph is the HRF estimates for each voxels, and the right is the HRF estimates by averaging the time series in the six activated voxels. For Scary stimulus, F-value =5.3, 9.1, 12.5, 7.5, 5.0, 7.5 in the six activated voxels. TFE gives smoother estimate in averaged time series than sFIR.

# Chapter 6

# Sampling Properties

The finite sample performance of our proposed methods has been well illustrated via simulations in Chapter 4 and the real applications in Chapter 5. In this chapter, we derive the asymptotic properties of the TFE method. Here is a brief outline. Section 6.1 starts with the asymptotic normality of the estimator including its expectation and covariance. Section 6.2 derives the hypothesis testing procedure associated with TFE. Section 6.3 shows that the weighted least squares estimator has a smaller variance than the ordinary least squares estimator, hence more efficient.

## 6.1 Sampling Properties of Multiple HRFs Estimation

This section is about the asymptotic distribution of the HRF estimator. We claimed in the previous chapters that the estimated HRF possesses an asymptotic normal distribution. The proof of the asymptotic normality of $\hat{\mathbf{h}}(\cdot)$ is derived from the sampling property of the estimator $\hat{\mathbf{H}}(r)$ in frequency domain. So we will start to establish the sampling properties of $\hat{\mathbf{H}}(r)$.

We first recall the formulation of the HRF estimation problem. Let $Y(t)$ and $\epsilon(t)$, $t = 0, 1, \ldots, T-1$ be real-valued stochastic series and let $\mathbf{X}(t)$, $t = 0, 1, \ldots, T-1$ be an $n$ vector-valued fixed series. Suppose that $\mathbf{h}(u) = (h_1(u), h_2(u), \ldots, h_n(u))$ is a

$1 \times n$ filter. Then the multivariate HRF model we concern with is given by

$$Y(t) = \sum_u \mathbf{h}(u)\mathbf{X}(t-u) + \epsilon(t). \tag{6.1.1}$$

We will assume that the error series, $\epsilon(t)$, is stationary with 0 mean and power spectrum $s_{\epsilon\epsilon}(r)$. This power spectrum is called the error spectrum, which is to measure the extent that the series $Y(t)$ is determinable from the series $X(t)$ by linear filtering.

Recall that the finite Fourier transform of is given by

$$\varphi_{\mathbf{X}}(r) \equiv \varphi_{\mathbf{X}}^{(T)}(r) = \sum_{t=0}^{T-1} \mathbf{X}(t)\exp(-\mathrm{i}rt), \qquad r \in \mathbb{R}.$$

Let $K$ be a positive integer so that $2\pi K/T$ is closest to $r$. From the property of finite Fourier transform and the smoothness of $\mathbf{H}(\cdot)$, we have equation (3.1.4) below

$$\varphi_Y(\frac{2\pi(K+k)}{T}) \doteq \mathbf{H}(r)\varphi_{\mathbf{X}}(\frac{2\pi(K+k)}{T}) + \varphi_\epsilon(\frac{2\pi(K+k)}{T}), \quad k = 0, \pm 1, \ldots, \pm m,$$

where $m$ is suitably chosen.

From the definition of periodogram,

$$\mathbf{I}_{Y\mathbf{X}}(r) = (2\pi T)^{-1}\varphi_Y(r)\overline{\varphi_{\mathbf{X}}(r)}^{\tau}, \qquad \mathbf{I}_{\mathbf{XX}}(r) = (2\pi T)^{-1}\varphi_{\mathbf{X}}(r)\overline{\varphi_{\mathbf{X}}(r)}^{\tau},$$

The window spectrum estimate are given by

$$\hat{\mathbf{s}}_{Y\mathbf{X}}(r) = \sum_{k=1}^{T-1} b^{-1}W(b^{-1}(r - \frac{2\pi k}{T}))\mathbf{I}_{Y\mathbf{X}}(\frac{2\pi k}{T}),$$
$$\hat{\mathbf{s}}_{\mathbf{XX}}(r) = \sum_{k=1}^{T-1} b^{-1}W(b^{-1}(r - \frac{2\pi k}{T}))\mathbf{I}_{\mathbf{XX}}(\frac{2\pi k}{T}),$$

where $W(\cdot)$ is a weight function to be defined later, and $b$ is the smoothing parameter.

We now estimate $\mathbf{H}(r)$ by using (3.1.16)

$$\hat{\mathbf{H}}(r) = \hat{\mathbf{s}}_{Y\mathbf{X}}(r)\hat{\mathbf{s}}_{\mathbf{XX}}(r)^{-1}$$

and $s_{\epsilon\epsilon}(r)$ by

$$\hat{s}_{\epsilon\epsilon}(r) = \frac{bT/\gamma}{bT/\gamma - n}[\hat{s}_{YY}(r) - \hat{\mathbf{s}}_{Y\mathbf{X}}(r)\hat{\mathbf{s}}_{\mathbf{XX}}(r)^{-1}\hat{\mathbf{s}}_{\mathbf{X}Y}(r)].$$

Finally, the estimate of HRF is given by (3.1.17)

$$\hat{\mathbf{h}}(u) = \frac{1}{T}\sum_{t=0}^{T-1}\hat{\mathbf{H}}(\frac{2\pi t}{T})\exp(\mathrm{i}2\pi tu/T).$$

We now describe the weight function $W(\cdot)$ based on the following formulation using a small window function.

**Assumption 6.1.1.** *$w(\alpha)$, $-\infty < \alpha < \infty$, is bounded, even, non-negative, equal to 0 for $|\alpha| > \pi$ and such that*

$$\int_{-\pi}^{\pi} w(\alpha)d\alpha = 1.$$

Set

$$W(\alpha) = \sum_{j=-\infty}^{\infty} w(\alpha + 2\pi j).$$

We see that $W(\cdot)$ is non-negative, symmetric and periodic:

$$W(\alpha + 2\pi) = W(\alpha).$$

Also note that $I_{xy}(0) = 0$. In order to reflect the notion that the weight function should become more concentrated as the sample size $T$ tends to $\infty$, we introduce a

bandwidth parameter $b$. If $b \to 0$ as $T \to \infty$, then for $T$ sufficiently large

$$\int_0^{2\pi} b^{-1} W(b^{-1}\alpha) d\alpha = 1.$$

We will frequently assume that our series satisfy

**Assumption 6.1.2.** *$X(t)$, $t = 0, \pm 1, \ldots$ is uniformly bounded and if $\hat{\mathbf{s}}_{\mathbf{XX}}(r)$ is given by (3.1.15), then there is a finite $K$ such that*

$$\|\hat{\mathbf{s}}_{\mathbf{XX}}(r)\| < K, \qquad \|\hat{\mathbf{s}}_{\mathbf{XX}}(r)^{-1}\| < K$$

*for all $r$ when $T$ is sufficiently large.*

As $\mathbf{X}(t)$ is a strictly stationary $n$ vector-valued series and its span of dependence is small enough that

$$\sum_{u_1,\ldots,u_{k-1}=-\infty}^{\infty} |\mathrm{cum}\{X_{a_1}(u_1), \ldots, X_{a_{k-1}}(u_{k-1})\}| < \infty, \qquad a_1, \ldots, a_{k-1} = 1, \ldots, n$$

where $\mathrm{cum}\{\cdot\}$ is the joint cumulant function of order $k-1$ of the series $\mathbf{X}(t)$ for $k = 2, 3, \ldots$, the dependence of the values of the process is lessen by the following assumption.

**Assumption 6.1.3.** *Given the $n$-vector stationary process $\mathbf{X}(t)$ with components $X_j$, $j = 1, \ldots, n$, there is an $l \geq 0$ with*

$$\sum_{u_1,\ldots,u_{k-1}=-\infty}^{\infty} \{1 + |u_j|^l\} |\mathrm{cum}\{X_{a_1}(u_1), \ldots, X_{a_{k-1}}(u_{k-1})\}| < \infty$$

*for $j = 1, \ldots, k-1$ and $k = 2, 3, \ldots$.*

Finally, the following assumption will ensure the variances of our estimates will be bounded.

**Assumption 6.1.4.** *$\epsilon(t)$ is stationary with 0 mean and the autocovariance function $c_{\epsilon\epsilon}(u), u \in \mathbb{Z}$ satisfies*

$$\sum_{u=-\infty}^{\infty} |u||c_{\epsilon\epsilon}(u)| < \infty.$$

We now proceed to the proof by starting with the sampling properties of $\hat{\mathbf{H}}(r)$.

### 6.1.1 Bias of $\hat{\mathbf{H}}(r)$

Set

$$R(t) = \sum_{u} \mathbf{h}(u)\mathbf{X}(t-u). \tag{6.1.2}$$

The model (6.1.1) then takes the form

$$Y(t) = R(t) + \epsilon(t). \tag{6.1.3}$$

Then the Finite Fourier transform is

$$\varphi_R(r) = \sum_{t=0}^{T-1} R(t) \exp(-\mathrm{i}rt) \tag{6.1.4}$$

The approximate relation between $\varphi_R(\mathrm{r})$ and $\varphi_{\mathbf{X}}(\mathrm{r})$ is given by

**Lemma 6.1.1.** *Suppose that $|\mathbf{X}(t)| \leq M, t = 0, 1, \ldots, T-1$ and that $\Sigma|u||\mathbf{h}(u)| < \infty$. Then*

$$|\varphi_R(r) - \mathbf{H}(r)\varphi_{\mathbf{X}}(r)| \leq 4M \sum_{u} |u||\mathbf{h}(u)| \tag{6.1.5}$$

*Proof.*

$$\begin{aligned}
\varphi_R(r) &= \sum_u \mathbf{h}(u) \left[ \sum_{t=0}^{T-1} \mathbf{X}(t-u) \exp(-\mathrm{i}rt) \right] \\
&= \sum_{u=-\infty}^{0} \mathbf{h}(u) \exp(-\mathrm{i}ru) \left[ \sum_{\nu=0}^{T-1} - \sum_{\nu=0}^{-u-1} + \sum_{\nu=T}^{T-1-u} \right] \mathbf{X}(\nu) \exp(-\mathrm{i}r\nu) \\
&\quad + \sum_{u=1}^{\infty} \mathbf{h}(u) \exp(-\mathrm{i}ru) \left[ \sum_{\nu=0}^{T-1} - \sum_{\nu=-u}^{-1} + \sum_{\nu=T-u}^{T-1} \right] \mathbf{X}(\nu) \exp(-\mathrm{i}r\nu) \\
&= \mathbf{H}(r)\varphi_{\mathbf{X}}(r) + e(r)
\end{aligned}$$

where $|e(r)| < 4M \sum_u |u||\mathbf{h}(u)$ since $|\mathbf{X}(t)| \leq M$. □

In the proofs below we will require the following lemma (Brillinger, 1981, p. 421).

**Lemma 6.1.2.** *Given a* $1 \times M$ *matrix* $\mathbf{P}$ *and an* $r \times M$ *matrix* $\mathbf{Q}$ *we have*

$$||\mathbf{P}\bar{\mathbf{Q}}^{\tau}(\mathbf{Q}\bar{\mathbf{Q}}^{\tau})^{-\mathbf{1}}|| \leq ||\mathbf{P}\bar{\mathbf{P}}^{\tau}||^{1/2}||(\mathbf{Q}\bar{\mathbf{Q}}^{\tau})^{-1}||^{1/2}.$$

*Proof.* We begin by noting the matrix form of Schwarz's inequality

$$\mathbf{P}\bar{\mathbf{P}}^{\tau} \geq \mathbf{P}\bar{\mathbf{Q}}^{\tau}(\mathbf{Q}\bar{\mathbf{Q}}^{\tau})^{-\mathbf{1}}\mathbf{Q}\bar{\mathbf{P}}^{\tau}.$$

This implies

$$||\mathbf{P}\hat{\mathbf{P}}^{\tau}|| \geq ||\mathbf{P}\bar{\mathbf{Q}}^{\tau}(\mathbf{Q}\bar{\mathbf{Q}}^{\tau})^{-\mathbf{1}}\mathbf{Q}\bar{\mathbf{P}}^{\tau}|| \geq ||\mathbf{P}\bar{\mathbf{Q}}^{\tau}(\mathbf{Q}\bar{\mathbf{Q}}^{\tau})^{-\mathbf{1/2}}||^2.$$

Hence,

$$||\mathbf{P}\bar{\mathbf{Q}}^{\tau}(\mathbf{Q}\bar{\mathbf{Q}}^{\tau})^{-\mathbf{1}}|| \leq ||\mathbf{P}\bar{\mathbf{Q}}^{\tau}(\mathbf{Q}\bar{\mathbf{Q}}^{\tau})^{-\mathbf{1/2}}|| \cdot ||(\mathbf{Q}\bar{\mathbf{Q}}^{\tau})^{-\mathbf{1/2}}|| \leq ||\mathbf{P}\bar{\mathbf{P}}^{\tau}||^{1/2}||(\mathbf{Q}\bar{\mathbf{Q}}^{\tau})^{-1}||^{1/2}.$$

□

**Theorem 6.1.1.** *Let $\epsilon(t)$, $t = 0, \pm 1, \ldots$ satisfy Assumption 6.1.3, $\mathbf{X}(t)$, $t = 0, \pm, \ldots$ satisfy certain Assumption 6.1.2. Let $Y(t)$, $t = 0, \pm 1, \ldots$ be given by (6.1.1) where $\mathbf{h}(u)$ satisfies $\Sigma |u||\mathbf{h}(u)| < \infty$. $W(\alpha)$ is defined in (6.1). Let $\mathbf{H}(r)$ be given by (3.1.16). Then*

$$\begin{aligned} E\hat{\mathbf{H}}(r) &= \left\{ \sum_{k=1}^{T-1} b^{-1} W(b^{-1}(r - \frac{2\pi k}{T})) \mathbf{H}(\frac{2\pi k}{T}) \mathbf{I}_{XX}(\frac{2\pi k}{T}) \right\} \\ &\quad \times \left\{ \sum_{k=1}^{T-1} b^{-1} W(b^{-1}(r - \frac{2\pi k}{T})) \mathbf{I}_{XX}(\frac{2\pi k}{T}) \right\}^{-1} + \mathrm{O}(T^{-1/2}) \\ &= \mathbf{H}(r) + \mathrm{O}(b^{-1}) + \mathrm{O}(T^{-1/2}), \end{aligned}$$

*where the error terms are uniform in $r$.*

*Proof.* Since $E\epsilon(t) = 0$, we have

$$\hat{\mathbf{H}}(r) = \hat{\mathbf{s}}_{R\mathbf{X}}(r) \hat{\mathbf{s}}_{\mathbf{XX}}(r)^{-1}.$$

By Lemma 6.1.1, $\varphi_R(r) = \mathbf{H}(r)\varphi_{\mathbf{X}}(r) + e(r)$. Thus

$$\begin{aligned} \hat{\mathbf{s}}_{R\mathbf{X}}(r) &= \sum_{k=1}^{T-1} b^{-1} W(b^{-1}(r - \frac{2\pi k}{T}))(2\pi T)^{-1} \left[ \mathbf{H}(r)\varphi_{\mathbf{X}}(\frac{2\pi k}{T}) + e(r) \right] \overline{\varphi_{\mathbf{X}}(\frac{2\pi k}{T})^{\tau}} \\ &= \sum_{k=1}^{T-1} b^{-1} W(b^{-1}(r - \frac{2\pi k}{T})) \mathbf{H}(\frac{2\pi k}{T}) \mathbf{I}_{XX}(\frac{2\pi k}{T}) + \mathbf{G}, \end{aligned}$$

where $\mathbf{G} = \sum_{k=1}^{T-1} b^{-1} W(b^{-1}(r - \frac{2\pi k}{T})) \mathbf{H}(\frac{2\pi k}{T}) e(r) \overline{\varphi_{\mathbf{X}}(\frac{2\pi k}{T})^{\tau}}$. Hence,

$$\begin{aligned} E\hat{\mathbf{H}}(r) &= E\hat{\mathbf{s}}_{Y\mathbf{X}}(r) \hat{\mathbf{s}}_{\mathbf{XX}}(r)^{-1} \\ &= \hat{\mathbf{s}}_{R\mathbf{X}}(r) \hat{\mathbf{s}}_{\mathbf{XX}}(r)^{-1} \end{aligned}$$

$$= \left\{ \sum_{k=1}^{T-1} b^{-1} W(b^{-1}(r - \frac{2\pi k}{T})) \mathbf{H}(\frac{2\pi k}{T}) \mathbf{I}_{XX}(\frac{2\pi k}{T}) \right\}$$
$$\times \left\{ \sum_{k=1}^{T-1} b^{-1} W(b^{-1}(r - \frac{2\pi k}{T})) \mathbf{I}_{XX}(\frac{2\pi k}{T}) \right\}^{-1} + \mathbf{G} \cdot \hat{\mathbf{s}}_{\mathbf{XX}}(r)^{-1} \qquad (6.1.6)$$

By Lemma 6.1.2,

$$||\mathbf{G} \cdot \hat{\mathbf{s}}_{\mathbf{XX}}(r)^{-1}|| \leq \left\{ \sum_{k=1}^{T-1} b^{-1} W(b^{-1}(r - \frac{2\pi k}{T}))(2\pi T)^{-1} |e(\frac{2\pi k}{T})|^2 \right\}^{1/2}$$
$$\times \left|\left| \left\{ \sum_{k=1}^{T-1} b^{-1} W(b^{-1}(r - \frac{2\pi k}{T})) \mathbf{I}_{XX}(\frac{2\pi k}{T}) \right\}^{-1} \right|\right|^{1/2}$$
$$\leq K T^{-1/2} ||\mathbf{s}_{\mathbf{XX}}(r)||^{1/2} \qquad (6.1.7)$$

where $K$ is finite coming from the fact that $e(r)$ is bounded (Lemma 6.1.1).

According to Taylor expansion, $\mathbf{H}(\frac{2\pi k}{T}) = \mathbf{H}(r) + \mathrm{O}(|r - \frac{2\pi l}{T}|^{-1})$. The region in which $W(\cdot)$ is nonzero is $|r - (2\pi k/T)| \leq b^{-1}\pi$. Thus

$$\mathbf{H}(\frac{2\pi k}{T}) = \mathbf{H}(r) + \mathrm{O}(b^{-1}). \qquad (6.1.8)$$

The desired result follows from (6.1.6) – (6.1.8). This completes the proof of Theorem 6.1.1. □

Turning to the case of $\hat{s}_{\epsilon\epsilon}(r)$, our estimate of the error spectrum, we need to prove it is asymptotically unbiased estimate of $s_{\epsilon\epsilon}(r)$. Define

$$\hat{s}^*_{\epsilon\epsilon}(r) = 2\pi T^{-1} \sum_{k=1}^{T-1} b^{-1} W(b^{-1}(r - \frac{2\pi k}{T}))(2\pi T)^{-1} \left| \varphi_\epsilon(\frac{2\pi k}{T}) \right|^2, \qquad (6.1.9)$$

where $\varphi_\epsilon(r) = \sum_{t=0}^{T-1} \epsilon(t) \exp(-\mathrm{i}rt)$. Also we set

$$\hat{\mathbf{s}}_{\mathbf{X}\epsilon}(r) = 2\pi T^{-1} \sum_{k=1}^{T-1} b^{-1} W(b^{-1}(r - \frac{2\pi k}{T}))(2\pi T)^{-1} \varphi_{\mathbf{X}}(\frac{2\pi k}{T}) \overline{\varphi_\epsilon(\frac{2\pi k}{T})}. \tag{6.1.10}$$

We use $[\mathbf{s}_{\mathbf{X}\epsilon}(r)]_j$ to denote the $j$th entry of $\mathbf{s}_{\mathbf{X}\epsilon}(r)$.

Before we give the asymptotical property of $\hat{s}_{\epsilon\epsilon}(r)$, we need the following lemmas.

**Lemma 6.1.3.** *If a function $g(x)$ has finite total variation, $V$, on $[0, 1]$, then*

$$\left| \int_0^1 g(x)dx - \frac{1}{n} \sum_{k=1}^{n} g(\frac{k}{n}) \right| \leq \frac{V}{n}.$$

*Proof.* See (Brillinger, 1981, p. 415). □

**Lemma 6.1.4.** *Under the conditions of Theorem 6.1.1,*

$$\mathrm{cov}\{[\hat{\mathbf{s}}_{\epsilon\mathbf{X}}(r_1)]_j, [\hat{\mathbf{s}}_{\epsilon\mathbf{X}}(r_2)]_k\} = \mathrm{O}(bT^{-1}) \tag{6.1.11}$$

$$\mathrm{cov}\{[\hat{\mathbf{s}}_{\epsilon\mathbf{X}}(r_1)]_j, \hat{s}^*_{\epsilon\epsilon}(r_2)\} = \mathrm{O}(T^{-3/2}) \tag{6.1.12}$$

$$\mathrm{cov}\{\hat{s}^*_{\epsilon\epsilon}(r_1), \hat{s}^*_{\epsilon\epsilon}(r_2)\} = \mathrm{O}(bT^{-1}). \tag{6.1.13}$$

*Proof.* First, we claim

$$\sum_{k=1}^{T-1} b^{-1} W(b^{-1}(r - \frac{2\pi k}{T})) \left[ \varphi_{\mathbf{X}}(\frac{2\pi k}{T}) \right]_j = \mathrm{O}(T^{3/2})$$

which can be verified by Assumption 6.1.2 and by

$$\begin{aligned} &\left| 2\pi T^{-1} \sum_k b^{-1} W(b^{-1}(r - \frac{2\pi k}{T})) \left[ \varphi_{\mathbf{X}}(\frac{2\pi k}{T}) \right]_j \right| \\ &\leq \left\{ 2\pi T^{-1} \sum_k b^{-1} W(b^{-1}(r - \frac{2\pi k}{T})) \left| \left[ \varphi_{\mathbf{X}}(\frac{2\pi k}{T}) \right]_j \right|^2 \right\}^{1/2} \end{aligned}$$

$$\leq (2\pi T)^{1/2}||\hat{\mathbf{s}}_{\mathbf{XX}}(r)||^{1/2}.$$

Now

$$\begin{aligned}
&\operatorname{cov}\{[\hat{\mathbf{s}}_{\epsilon\mathbf{X}}(r_1)]_j, [\hat{\mathbf{s}}_{\epsilon\mathbf{X}}(r_2)]_k\} \\
&= (2\pi T^{-1})^2 \sum_l \sum_m b^{-1}W(b^{-1}(r_1 - \frac{2\pi l}{T}))b^{-1}W(b^{-1}(r_1 - \frac{2\pi m}{T}))(2\pi T)^{-2} \\
&\quad \times \left[\varphi_{\mathbf{X}}(\frac{2\pi l}{T})\right]_j \left[\varphi_{\mathbf{X}}(\frac{2\pi m}{T})\right]_k \varphi_\epsilon(\frac{2\pi l}{T})\overline{\varphi_\epsilon(\frac{2\pi m}{T})} \\
&= T^{-4} \sum_l \sum_m b^{-1}W(b^{-1}(r_1 - \frac{2\pi l}{T}))b^{-1}W(b^{-1}(r_1 - \frac{2\pi m}{T})) \\
&\quad \times \left[\varphi_{\mathbf{X}}(\frac{2\pi l}{T})\right]_j \left[\varphi_{\mathbf{X}}(\frac{2\pi m}{T})\right]_k \cdot \mathrm{O}(1) \\
&= \mathrm{O}(T^{-4}bT^3) = \mathrm{O}(bT^{-1})
\end{aligned}$$

which verifies (6.1.11). By the same argument, (6.1.12) and (6.1.13) can be verified using the fact that $s_{\epsilon\epsilon}(r)$ has a uniformly bounded derivative and the fact that the support of $W(r)$ is $|r| \leq b^{-1}\pi$. □

**Lemma 6.1.5.** *$R(t) = \sum_u \mathbf{h}(u)\mathbf{X}(t-u)$. Under the assumptions of Theorem 6.1.1,*

$$\hat{\mathbf{s}}_{R\mathbf{X}}(r) = \hat{\mathbf{H}}(r)\hat{\mathbf{s}}_{\mathbf{XX}}(r) + \mathrm{O}(b^{-1}) + \mathrm{O}(T^{-1/2}) \tag{6.1.14}$$

$$\hat{\mathbf{s}}_{Y\mathbf{X}}(r) = \hat{\mathbf{s}}_{R\mathbf{X}}(r) + \hat{\mathbf{s}}_{\epsilon\mathbf{X}}(r) \tag{6.1.15}$$

$$\hat{s}^*_{RR}(r) = \hat{\mathbf{H}}(\mathbf{r})\hat{\mathbf{s}}_{\mathbf{XX}}(r)\overline{\hat{\mathbf{H}}(r)}^{\tau} + \mathrm{O}(b^{-1}) + \mathrm{O}(T^{-1/2}) \tag{6.1.16}$$

$$\hat{\mathbf{s}}_{\epsilon\mathbf{X}}(r)\hat{\mathbf{s}}_{\mathbf{XX}}(r)^{-1}\hat{\mathbf{s}}_{\mathbf{X}\epsilon}(r) = \mathrm{O}(\sum_j |[\hat{\mathbf{s}}_{\mathbf{X}\epsilon}(r)]_j|^2) \tag{6.1.17}$$

$$\begin{aligned}
\hat{s}_{\epsilon\epsilon}(r) &= \hat{s}^*_{\epsilon\epsilon}(r) - \hat{\mathbf{s}}_{\epsilon\mathbf{X}}(r)\hat{\mathbf{s}}_{\mathbf{XX}}(r)^{-1}\hat{\mathbf{s}}_{\mathbf{X}\epsilon}(r) + \mathrm{O}(b^{-1}) + \mathrm{O}(T^{-1/2}) \\
&\quad + \hat{s}^*_{R\epsilon}(r) - \hat{\mathbf{H}}(r)\hat{\mathbf{s}}_{\mathbf{X}\epsilon}(r) + \hat{s}^*_{\epsilon R}(r) - \hat{\mathbf{s}}_{\epsilon\mathbf{X}}(r)\overline{\hat{\mathbf{H}}(r)}^{\tau} \\
&= \hat{s}^*_{\epsilon\epsilon}(r) + \mathrm{O}(\sum_j |[\hat{\mathbf{s}}_{\mathbf{X}\epsilon}(r)]_j|^2) + \mathrm{O}(b^{-1}) + \mathrm{O}(T^{-1/2})
\end{aligned}$$

$$+ \hat{s}^*_{R\epsilon}(r) - \hat{\mathbf{H}}(r)\hat{\mathbf{s}}_{\mathbf{X}\epsilon}(r) + \hat{s}^*_{\epsilon R}(r) - \hat{\mathbf{s}}_{\epsilon\mathbf{X}}(r)\overline{\hat{\mathbf{H}}(r)}^{\tau}. \quad (6.1.18)$$

*Proof.* (6.1.14) has been derived in the proof of Theorem 6.1.1.

(6.1.15) can be easily derived from the definition of $R(t)$.

From Lemma 6.1.1,

$$\begin{aligned}
\hat{s}_{RR} &= 2\pi T^{-1}\sum_k b^{-1}W(b^{-1}(r-\frac{2\pi k}{T}))(2\pi T)^{-1}\varphi_R(\frac{2\pi k}{T})\overline{\varphi_R(\frac{2\pi k}{T})} \\
&= 2\pi T^{-1}\sum_k b^{-1}W(b^{-1}(r-\frac{2\pi k}{T}))(2\pi T)^{-1}\left\{\hat{\mathbf{H}}(\frac{2\pi k}{T})\varphi_{\mathbf{X}}(\frac{2\pi k}{T})+\mathrm{O}(1)\right\} \\
&\quad\times\overline{\left\{\hat{\mathbf{H}}(\frac{2\pi k}{T})\varphi_{\mathbf{X}}(\frac{2\pi k}{T})+\mathrm{O}(1)\right\}}.
\end{aligned}$$

It follows from $\hat{\mathbf{H}}(r) = \hat{\mathbf{H}}(2\pi k/T) + \mathrm{O}(b^{-1})$ and Schwarz's inequality that (6.1.16) could be proved.

We know $||\hat{\mathbf{s}}_{\mathbf{XX}}||$ is bounded by Assumption 6.1.2, then we have

$$\begin{aligned}
||\hat{\mathbf{s}}_{\epsilon\mathbf{X}}(r)\hat{\mathbf{s}}_{\mathbf{XX}}(r)^{-1}\hat{\mathbf{s}}_{\mathbf{X}\epsilon}(r)|| &\le K\cdot\mathrm{tr}\{\hat{\mathbf{s}}_{\epsilon\mathbf{X}}(r)\hat{\mathbf{s}}_{\mathbf{X}\epsilon}(r)\hat{\mathbf{s}}_{\mathbf{XX}}(r)^{-1}\} \\
&\le L\cdot\mathrm{tr}\{\hat{\mathbf{s}}_{\epsilon\mathbf{X}}(r)\hat{\mathbf{s}}_{\mathbf{X}\epsilon}(r)\},
\end{aligned}$$

where $K$ and $L$ are finite. Thus (6.1.17) is verified.

Now

$$\begin{aligned}
\hat{s}_{\epsilon\epsilon}(r) &= \frac{bT/\gamma}{bT/\gamma - r}[\hat{s}_{YY}(r) - \hat{\mathbf{s}}_{Y\mathbf{X}}(r)\hat{\mathbf{s}}_{\mathbf{XX}}(r)^{-1}\hat{\mathbf{s}}_{\mathbf{X}Y}(r)] \\
&= \hat{s}_{RR}(r) - \hat{s}_{R\epsilon}(r) + \hat{s}_{\epsilon R}(r) + \hat{s}^*_{\epsilon\epsilon}(r) \\
&\quad - \{\hat{\mathbf{s}}_{R\mathbf{X}}(r) + \hat{\mathbf{s}}_{\epsilon\mathbf{X}}(r)\}\hat{\mathbf{s}}_{\mathbf{XX}}(r)^{-1}\{\hat{\mathbf{s}}_{\mathbf{X}R}(r) + \hat{\mathbf{s}}_{\mathbf{X}\epsilon}(r)\}.
\end{aligned}$$

The result of (6.1.18) follows from (6.1.14) - (6.1.17). □

**Theorem 6.1.2.** *Under the conditions of Theorem 6.1.1,*

$$E\hat{s}_{\epsilon\epsilon}(r) = s_{\epsilon\epsilon}(r) + \mathrm{O}(b^{-1}) + \mathrm{O}(bT^{-1}) + \mathrm{O}(T^{-1/2}).$$

*Proof.* From Lemma 6.1.5 and (6.1.9), we see that

$$\begin{aligned} E\hat{s}_{\epsilon\epsilon}(r) &= E\hat{s}^*_{\epsilon\epsilon}(r) + \mathrm{O}(\sum_j |E[\mathbf{s}_{\mathbf{X}\epsilon}(r)]_j|^2) + \mathrm{O}(b^{-1}) + \mathrm{O}(T^{-1/2}) \\ &= E\hat{s}^*_{\epsilon\epsilon}(r) + \mathrm{O}(bT^{-1}) + \mathrm{O}(b^{-1}) + \mathrm{O}(T^{-1/2}). \end{aligned}$$

Here the discrete Fourier Transform of $\epsilon$ leads to the discrete version $\hat{s}^*_{\epsilon\epsilon}(r)$. By using Lemma 6.1.3 and the sampling property of the unbiased estimate $\hat{s}^*_{\epsilon\epsilon}(r)$,

$$\begin{aligned} E\hat{s}^*_{\epsilon\epsilon}(r) &= 2\pi T^{-1} \sum_{k=1}^{T-1} b^{-1} W(b^{-1}(r - \frac{2\pi k}{T})) s_{\epsilon\epsilon}(\frac{2\pi k}{T})) + \mathrm{O}(T^{-1}) \\ &= s_{\epsilon\epsilon}(r) + \mathrm{O}(b^{-1}) + \mathrm{O}(bT^{-1}). \end{aligned}$$

Therefore, the statement is true. □

This tells us that under the conditions of Theorem 6.1.1 and if $b \to \infty, b^{-1}T \to \infty$ as $T \to \infty$, $\hat{s}_{\epsilon\epsilon}(r)$ is an asymptotically unbiased estimate of $s_{\epsilon\epsilon}(r)$.

### 6.1.2 Covariance of $\hat{\mathbf{H}}(r)$

We now examine the second order properties of $\hat{\mathbf{H}}(r)$.

**Theorem 6.1.3.** *Let $\epsilon(t)$, $t = 0, \pm 1, \ldots$ satisfy Assumption 6.1.3 and have mean 0, $\mathbf{X}(t)$, $t = 0, \pm 1, \ldots$ satisfy Assumption 6.1.2. Let $Y(t)$, $t = 0, \pm 1, \ldots$ be given by (6.1.1) where $\mathbf{h}(u)$ satisfies $\Sigma |u||\mathbf{h}(u)| < \infty$. $W(\alpha)$ is defined in (6.1). Let $\mathbf{H}(r)$ is*

*given by (3.1.16). If* $b \to 0$ *as* $T \to \infty$*, then*

$$\mathrm{cov}(\hat{\mathbf{H}}(r_1)^\tau, \hat{\mathbf{H}}(r_2)^\tau) = \eta(r_1 - r_2) b T^{-1} 2\pi \int W(\alpha)^2 d\alpha \hat{\mathbf{s}}_{\mathbf{xx}}(r_1)^{-1} \hat{\mathbf{g}}_{\mathbf{xx}}(r_1) \hat{\mathbf{s}}_{\mathbf{xx}}(r_1)^{-1} s_{\epsilon\epsilon}(r_1) + \mathrm{O}(T^{-1}), \tag{6.1.19}$$

*where* $\eta(0) = 1$ *and* $\eta(r) = 0$ *for* $r \neq 0$*, and*

$$\hat{\mathbf{g}}_{\mathbf{xx}}(r) = \{\sum_{k \neq 0} b^{-2} W(b^{-1}(r - \frac{2\pi k}{T}))^2 \mathbf{I}_{\mathbf{xx}}(\frac{2\pi k}{T})\} \{\int_0^{2\pi} W(\alpha)^2 d\alpha\}^{-1}.$$

*In the case that* $W(\cdot)$ *is uniform window, the expression of (6.1.19) has the form*

$$\eta(r_1 - r_2) b T^{-1} \hat{\mathbf{s}}_{\mathbf{xx}}(r_1)^{-1} s_{\epsilon\epsilon}(r_1) 2\pi \int W(\alpha)^2 d\alpha + \mathrm{O}(T^{-1}). \tag{6.1.20}$$

*Proof.* By using

$$\sum_{k=1}^{T-1} b^{-1} W(b^{-1}(r - \frac{2\pi k}{T})) \left[\varphi_{\mathbf{x}}(\frac{2\pi k}{T})\right]_j = \mathrm{O}(T^{3/2}),$$

$$\begin{aligned}
&\mathrm{cov}(\hat{\mathbf{H}}(r_1)^\tau, \hat{\mathbf{H}}(r_2)^\tau) \\
=&\hat{\mathbf{s}}_{\mathbf{xx}}(r_1)^{-1} \mathrm{cov}\{[\hat{\mathbf{s}}_{\mathbf{x}\epsilon}(r_1)]_j, [\hat{\mathbf{s}}_{\mathbf{x}\epsilon}(r_2)]_k\} \hat{\mathbf{s}}_{\mathbf{xx}}(r_2)^{-1} \\
=&\hat{\mathbf{s}}_{\mathbf{xx}}(r_1)^{-1} \times \sum_{j,k \in \{1,\ldots,T-1\}} [(2\pi T^{-1})^2 b^{-2} W(b^{-1}(r_1 - \frac{2\pi j}{T})) W(b^{-1}(r_2 - \frac{2\pi k}{T}))(2\pi T)^{-2} \\
&\overline{\varphi_{\mathbf{x}}(\frac{2\pi j}{T})} E(\varphi_\epsilon(\frac{2\pi j}{T})^\tau \overline{\varphi_\epsilon(\frac{2\pi k}{T})}) \varphi_{\mathbf{x}}(\frac{2\pi k}{T})^\tau] \times \hat{\mathbf{s}}_{\mathbf{xx}}(r_2)^{-1} \\
=&\hat{\mathbf{s}}_{\mathbf{xx}}(r_1)^{-1} \times (\sum_{j=k} + \sum_{j \neq k}) [(2\pi T^{-1})^2 b^{-2} W(b^{-1}(r_1 - \frac{2\pi j}{T})) W(b^{-1}(r_2 - \frac{2\pi k}{T}))(2\pi T)^{-2}
\end{aligned}$$

$$\overline{\varphi_{\mathbf{X}}(\frac{2\pi j}{T})}E(\varphi_\epsilon(\frac{2\pi j}{T})^\tau\overline{\varphi_\epsilon(\frac{2\pi k}{T})})\varphi_{\mathbf{X}}(\frac{2\pi k}{T})^\tau] \times \hat{\mathbf{s}}_{\mathbf{XX}}(r_2)^{-1}$$

$$=\hat{\mathbf{s}}_{\mathbf{XX}}(r_1)^{-1}\times$$

$$\left\{\sum_{k=1}^{T}(2\pi T^{-1})^2b^{-2}W(b^{-1}(r_1-\frac{2\pi k}{T}))W(b^{-1}(r_2-\frac{2\pi k}{T}))\mathbf{I}_{\mathbf{XX}}(\frac{2\pi k}{T})\left(s_{\epsilon\epsilon}(\frac{2\pi k}{T})+\mathrm{O}(T^{-1})\right)\right\}$$

$$\times \hat{\mathbf{s}}_{\mathbf{XX}}(r_2)^{-1}+\hat{\mathbf{s}}_{\mathbf{XX}}(r_1)^{-1}\times$$

$$\left\{\sum_{k\neq j}(2\pi T^{-1})^2b^{-2}W(b^{-1}(r_1-\frac{2\pi j}{T}))W(b^{-1}(r_2-\frac{2\pi k}{T}))(2\pi T)^{-2}\overline{\varphi_{\mathbf{X}}(\frac{2\pi j}{T})}\varphi_{\mathbf{X}}(\frac{2\pi k}{T})^\tau\cdot\mathrm{O}(1)\right\}$$

$$\times \hat{\mathbf{s}}_{\mathbf{XX}}(r_2)^{-1}$$

$$=\hat{\mathbf{s}}_{\mathbf{XX}}(r_1)^{-1}\times\left\{\sum_{k=1}^{T}(2\pi T^{-1})^2b^{-2}W(b^{-1}(r_1-\frac{2\pi k}{T}))W(b^{-1}(r_2-\frac{2\pi k}{T}))\mathbf{I}_{\mathbf{XX}}(\frac{2\pi k}{T})s_{\epsilon\epsilon}(\frac{2\pi k}{T})\right\}$$

$$\times \hat{\mathbf{s}}_{\mathbf{XX}}(r_2)^{-1}+\mathrm{O}(T^{-1})$$

$$=s_{\epsilon\epsilon}(r_1)\cdot b\cdot\hat{\mathbf{s}}_{\mathbf{XX}}(r_1)^{-1}\times\left\{\sum_{k=1}^{T}(2\pi T^{-1})^2b^{-2}W(b^{-1}(r_1-\frac{2\pi k}{T}))W(b^{-1}(r_2-\frac{2\pi k}{T}))\mathbf{I}_{\mathbf{XX}}(\frac{2\pi k}{T})\right\}$$

$$\times \hat{\mathbf{s}}_{\mathbf{XX}}(r_2)^{-1}+\mathrm{O}(T^{-1})$$

If $r_1=r_2$, the above expression could be written as

$$b(2\pi T^{-1})^2\hat{\mathbf{s}}_{\mathbf{XX}}(r_1)^{-1}\left\{\sum_{k=1}^{T-1}b^{-2}W(b^{-1}(r_1-\frac{2\pi k}{T}))^2\mathbf{I}_{\mathbf{XX}}(\frac{2\pi k}{T})\right\}\hat{\mathbf{s}}_{\mathbf{XX}}(r_1)^{-1}s_{\epsilon\epsilon}(r_1).$$

If $r_1\neq r_2$, the first part of the expression is $\mathrm{O}(T^{-1})$ by using the same strategy as we did to the second part. Define function $\eta(r_1-r_2)=1$ if $r_1=r_2$, 0 if $r_1\neq r_2$.

Thus by substituting $\hat{\mathbf{g}}_{\mathbf{XX}}$, the result follows. □

### 6.1.3 Normality of $\hat{\mathbf{H}}(r)$

The asymptotic distribution of $\hat{\mathbf{H}}(r)$ will be discussed in this section.

**Theorem 6.1.4.** *Let $\epsilon(t)$, $t=0,\pm1,\ldots$ satisfy Assumption 6.1.3 and have mean*

*0,* $\mathbf{X}(t)$*,* $t = 0, \pm, \ldots$ *satisfy Assumption 6.1.2. Let* $Y(t)$*,* $t = 0, \pm 1, \ldots$ *be given by (6.1.1) where* $\mathbf{h}(u)$ *satisfies* $\Sigma|u||\mathbf{h}(u)| < \infty$*.* $W(\alpha)$ *is defined in (6.1). Let* $\mathbf{H}(r)$ *is given by (3.1.16). If* $b \to 0$ *as* $T \to \infty$*, then* $\hat{\mathbf{H}}(r)^\tau$ *is asymptotically*

$$N_r^C(E\hat{\mathbf{H}}(r)^\tau, b^{-1}T^{-1}2\pi \int W(\alpha)^2 d\alpha \hat{\mathbf{s}}_{\mathbf{XX}}(r)^{-1}\hat{\mathbf{g}}_{\mathbf{XX}}(r)\hat{\mathbf{s}}_{\mathbf{XX}}(r)^{-1}s_{\epsilon\epsilon}(r)) \tag{6.1.21}$$

*if* $r \neq 0 \ (mod\ \pi)$*.*

*Proof.* We prove the normality by evaluating joint cumulants of order greater than 2 of $\hat{\mathbf{H}}(r)$ and proving that these joint cumulants tend to 0.

Let $M > 2$ and $m_1, \ldots, m_M \in \{1, 2, \ldots, n\}$

$$\begin{aligned}
&\mathrm{cum}\{[\hat{\mathbf{H}}(r_1)]_{m_1}, \ldots, [\hat{\mathbf{H}}(r_M)]_{m_M}\} \\
=&K \cdot \mathrm{cum}\{[\hat{\mathbf{s}}_{\epsilon\mathbf{X}}(r_1)]_{m_1}, \ldots, [\hat{\mathbf{s}}_{\epsilon\mathbf{X}}(r_M)]_{m_M}\} \\
=&K \cdot (2\pi T^{-1})^M \sum_{q_1} \cdots \sum_{q_M} b^{-M} W(b^{-1}(r_1 - \frac{2\pi q_1}{T})) \cdots W(b^{-1}(r_M - \frac{2\pi q_M}{T})) \\
&\times (2\pi T)^{-M} \left[\varphi_{\mathbf{X}}(\frac{2\pi q_1}{T})\right]_{m_1} \cdots \left[\varphi_{\mathbf{X}}(\frac{2\pi q_M}{T})\right]_{m_M} \times \mathrm{cum}\left\{\overline{\varphi_\epsilon(\frac{2\pi q_1}{T})}, \ldots, \overline{\varphi_\epsilon(\frac{2\pi q_M}{T})}\right\} \\
=&\mathrm{O}(T^{-2M} b T^{3M/2}) \\
=&\mathrm{O}(bT^{-M/2}).
\end{aligned}$$

The cumulants of order greater than two tend to 0 as $T \to \infty$.

From Theorem 6.1.1 and Theorem 6.1.3, the asymptotical normality of $\hat{\mathbf{H}}(r)$ holds (Rosenblatt, 1959). □

### 6.1.4 Normality of $\hat{\mathbf{h}}(\cdot)$

As an estimate of HRF $\mathbf{h}(u)$ in (3.1.17) we consider

$$\hat{\mathbf{h}}(u) = P_T^{-1} \sum_{p=0}^{P_T-1} \hat{\mathbf{H}}(\frac{2\pi p}{P_T}) \exp(\frac{\mathrm{i}2\pi p u}{P_T}). \tag{6.1.22}$$

where $P_T$ is a sequence of positive integers tending to $\infty$ with $T$. Finally comes the asymptotic distribution of HRF estimator $\hat{\mathbf{h}}(u)$.

**Theorem 6.1.5.** *Let $\epsilon(t)$, $t = 0, \pm 1, \ldots$ satisfy Assumption 6.1.3 and have mean 0, $\mathbf{X}(t)$, $t = 0, \pm 1, \ldots$ satisfy Assumption 6.1.2. Let $Y(t)$, $t = 0, \pm 1, \ldots$ be given by (6.1.1) where $\mathbf{h}(u)$ satisfies $\Sigma |u||\mathbf{h}(u)| < \infty$. $W(\alpha)$ is defined in (6.1). Let $\hat{\mathbf{h}}(u)$ be given by (6.1.22), then*

$$E\hat{\mathbf{h}}(u) = \mathbf{h}(u) + \sum_{k \neq 0} \mathbf{h}(u + kP_T) + \mathrm{O}(b) + \mathrm{O}(T^{-1/2}) \tag{6.1.23}$$

*In particular, $\hat{\mathbf{h}}(u)$ is asymptotically unbiased. Furthermore, $\hat{\mathbf{h}}(u_1), \ldots, \hat{\mathbf{h}}(u_d)$ are asymptotically normal with mean $\mathbf{h}(u_1), \ldots, \mathbf{h}(u_d)$ and covariance structure*

$$cov(\hat{\mathbf{h}}(u), \hat{\mathbf{h}}(v)) = \frac{1}{P_T b T} 2\pi \int W(\alpha)^2 d\alpha \Lambda(u, v) + \mathrm{O}(T^{-1}), \tag{6.1.24}$$

*where*

$$\Lambda(u, v) = P_T^{-1} \sum_{p=0}^{P_T-1} \exp(\frac{\mathrm{i}2\pi(u - v)}{P_T}) s_{\epsilon\epsilon}(\frac{2\pi p}{P_T}) \hat{\mathbf{s}}_{\mathbf{XX}}(r)^{-1} \hat{\mathbf{g}}_{\mathbf{XX}}(r) \hat{\mathbf{s}}_{\mathbf{XX}}(r)^{-1}. \tag{6.1.25}$$

*Proof.* As the definition of (6.1.22) and the Theorem (6.1.1) show,

$$\begin{aligned}
E\hat{\mathbf{h}}(u) =& P_T^{-1} \sum_{p=0}^{P_T-1} E(\hat{\mathbf{H}})(\frac{2\pi p}{P_T}) \exp(\frac{\mathrm{i}2\pi pu}{P_T}) \\
=& P_T^{-1} \sum_{p=0}^{P_T-1} \{\mathbf{H}(\frac{2\pi p}{P_T}) + \mathrm{O}(b^{-1}) + \mathrm{O}(T^{-1/2})\} \exp(\frac{\mathrm{i}2\pi pu}{P_T}) \\
=& \mathbf{h}(u) + \sum_{k\neq 0} \mathbf{h}(u + kP_T) + \mathrm{O}(b) + \mathrm{O}(T^{-1/2}).
\end{aligned}$$

The last equal sign is derived by

$$\begin{aligned}
& \mathbf{h}(u) + \sum_{k\neq 0} \mathbf{h}(u + kP_T) \\
=& (2\pi)^{-1} \int_0^{2\pi} \mathbf{H}(\lambda) \exp(\mathrm{i}u\lambda) d\lambda + \sum_{k\neq 0} (2\pi)^{-1} \int_0^{2\pi} \mathbf{H}(\lambda) \exp(\mathrm{i}(u + kP_T)\lambda) d\lambda \\
=& (2\pi)^{-1} \int_0^{2\pi} \mathbf{H}(\lambda) [\exp(\mathrm{i}u\lambda) + \sum_{k\neq 0} \exp(\mathrm{i}(u + kP_T)\lambda)] d\lambda \\
=& \int_0^{1} \mathbf{H}(2\pi\lambda) [\exp(\mathrm{i}u2\pi\lambda) + \sum_{k\neq 0} \exp(\mathrm{i}(u + kP_T)2\pi\lambda)] d\lambda \\
=& \int_0^{1} \mathbf{H}(2\pi\lambda) \exp(\mathrm{i}u2\pi\lambda) [1 + \sum_{k\neq 0} \exp(\mathrm{i}kP_T 2\pi\lambda)] d\lambda \\
=& P_T^{-1} \sum_{p=0}^{P_T-1} \mathbf{H}(\frac{2\pi p}{P_T}) \exp(\frac{\mathrm{i}2\pi pu}{P_T}) [1 + \sum_{k\neq 0} \exp(\mathrm{i}k2\pi p)] \\
=& P_T^{-1} \sum_{p=0}^{P_T-1} \mathbf{H}(\frac{2\pi p}{P_T}) \exp(\frac{\mathrm{i}2\pi pu}{P_T}).
\end{aligned}$$

Thus, $\hat{\mathbf{h}}(u)$ is asymptotically unbiased. From the normality of $\hat{\mathbf{H}}(r)$, the normality of $\hat{\mathbf{h}}(u)$ can be obtained. □

## 6.2 Properties of Hypothesis Testing Procedure

In the testing section, we have multiple hypothesis tests: testing the linearity, testing the effect from a specific stimulus, detecting the activation, and testing the difference among HRFs. The asymptotic distributions for $\hat{\mathbf{H}}(r)$ and $\hat{\mathbf{h}}(u)$ have been derived in Section 6.1, which are given respectively in Theorem (6.1.4) and (6.1.5). To verify the $F$ statistic in hypothesis testing, we start from the basis of least square and linear regression theory in complex-valued random variables and parameters.

**Theorem 6.2.1.** *Let*

$$\mathbf{Y} = \mathbf{aX} + \epsilon \tag{6.2.1}$$

*where $\epsilon$ is a $1 \times n$ matrix of complex-valued random variables with $E\epsilon = 0$, $E\epsilon^{\tau}\epsilon = 0$, $E\overline{\epsilon}^{\tau}\epsilon = \sigma^2\mathbf{I}$. $\mathbf{a}$ is a $1 \times k$ matrix of unknown complex-valued parameters, $\mathbf{X}$ is a $k \times n$ matrix of known complex-valued entries. Then*

$$(\mathbf{Y} - \mathbf{aX})\overline{(\mathbf{Y} - \mathbf{aX})}^{\tau} \tag{6.2.2}$$

*is minimized, for choice of $\mathbf{a}$, by $\hat{\mathbf{a}} = \mathbf{Y}\overline{\mathbf{X}}^{\tau}(\mathbf{X}\overline{\mathbf{X}}^{\tau})^{-\mathbf{1}}$ if $\mathbf{X}\overline{\mathbf{X}}^{\tau}$ is nonsingular. The minimum achieved is $\mathbf{Y}(\mathbf{I} - \overline{\mathbf{X}}^{\tau}(\mathbf{X}\overline{\mathbf{X}}^{\tau})^{-\mathbf{1}}\mathbf{X})\overline{\mathbf{Y}}^{\tau}$. Also $E\hat{\mathbf{a}} = \mathbf{a}$, the covariance matrix of $\hat{\mathbf{a}}$, is given by $E(\hat{\mathbf{a}} - \mathbf{a})^{\tau}\overline{(\hat{\mathbf{a}} - \mathbf{a})} = \sigma^2(\mathbf{X}\overline{\mathbf{X}}^{\tau})^{-1}$ and if $\hat{\sigma}^2 = \frac{1}{n-k}\mathbf{Y}(\mathbf{I} - \overline{\mathbf{X}}^{\tau}(\mathbf{X}\overline{\mathbf{X}}^{\tau})^{-\mathbf{1}}\mathbf{X})\overline{\mathbf{Y}}^{\tau}$ then $E\hat{\sigma}^2 = \sigma^2$. In addition, $\hat{\mathbf{a}}$ is the minimum variance linear unbiased estimate of $\mathbf{a}$.*

This is the common theorem in least square and linear regression. With respect to distributional aspects of the above $\hat{\mathbf{a}}$ and $\hat{\sigma}^2$ we have

**Theorem 6.2.2.** *If, in addition to the conditions of Theorem 6.2.1, the component of $\epsilon$ has independent $N_1^C(0, \sigma^2)$ distributions, then $\hat{\mathbf{a}}$ is $N_k^C(\mathbf{a}^{\tau}, \sigma^2(\mathbf{X}\bar{\mathbf{X}}^{\tau})^{-1})$, and $\hat{\sigma}^2$ is $\hat{\sigma}^2\chi^2_{n-k}/(n-k)$ independent of $\hat{\mathbf{a}}$.*

It follows directly from Theorem 6.2.2 that

$$F = [(n-k)\hat{\mathbf{a}}\mathbf{X}\bar{\mathbf{X}}^{\tau}\bar{\hat{\mathbf{a}}}^{\tau}]/[k\mathbf{Y}(\mathbf{I} - \bar{\mathbf{X}}^{\tau}(\mathbf{X}\bar{\mathbf{X}}^{\tau})^{-\mathbf{1}}\mathbf{X})\bar{\mathbf{Y}}^{\tau}] \tag{6.2.3}$$

is noncentral $F$, degrees of freedom $2k$ over $2(n-k)$ and noncentrality parameter $\mathbf{a}\mathbf{X}\bar{\mathbf{X}}^{\tau}\bar{\mathbf{a}}^{\tau}/\sigma^2$. We see that the hypothesis $\mathbf{a} = 0$ may be tested by noting that (6.2.3) has a central $F_{k,n-k}$ distribution when the hypothesis holds. A related statistic is

$$|\hat{R}_{YX}|^2 = \frac{\hat{\mathbf{a}}\mathbf{X}\bar{\mathbf{X}}^{\tau}\bar{\hat{\mathbf{a}}}^{\tau}}{\mathbf{Y}\bar{\mathbf{Y}}^{\tau}} \tag{6.2.4}$$

the squared sample multiple correlation coefficient. It may be seen that $0 \leq \hat{R}^2_{YX} \leq 1$. Also from (6.2.3) we see that

$$\hat{R}^2_{YX} = \frac{Fk/(n-k)}{1 + Fk/(n-k)} \tag{6.2.5}$$

and so its distribution is determinable directly from the noncentral $F$.

As we see, $\hat{\mathbf{H}}(r)$ can be regarded as the coefficient from a complex linear system (3.1.4) as described in Theorem 6.2.1. The hypothesis on testing the linearity (3.2.1) is verified by the equation (6.2.5) and Theorem 6.2.1. To detect the activation (3.2.3), we test whether $\hat{\mathbf{H}}(r) = 0$, which is actually analogous to equation (6.2.3). Under the hypothesis $\hat{\mathbf{H}}(r) = 0$, the equation (6.2.3) follows $F$ distribution with degree of freedom $(2k, 2(n-k))$.

The effect from a specific stimulus (3.2.2) is derived by partial coherence, which measures the linear relation between the single stimulus and the other stimulus group. So the partial coherence is based on certain conditions, and here the unconditional coherence is the coherence we defined before. According to Fisher et al. (1924), the

conditional coherence follows the asymptotic distribution of the unconditional coherence with the parameter $bT/\gamma$ replaced by $bT/\gamma - n$. Thus under the hypothesis of zero partial coherence, the statistic in the effect of a specific stimulus has $F$ distribution with a certain degree of freedom.

The final hypothesis in Chapter 3 tests the difference between HRFs (3.2.11). The procedure was derived in the context of that chapter. According to the asymptotic distributional properties of the HRF-related estimates in the last section, we have already verified and proven the testing procedures.

## 6.3 Sampling Properties of Weighted Least Square

Our simulation studies in Section 4.4 claimed that the WLS estimator has a lower variance than the ordinary least squares (OLS) estimator. We recall the following weighted spectrum estimators:

$$\tilde{\mathbf{s}}_{Y\mathbf{X}}(r) = \sum_{k\neq 0} b^{-1} W(b^{-1}(r - \frac{2\pi k}{T}))\hat{s}_{\epsilon\epsilon}^{-1}(\frac{2\pi k}{T})\hat{\mathbf{s}}_{Y\mathbf{X}}(\frac{2\pi k}{T}), \tag{6.3.1}$$

$$\tilde{\mathbf{s}}_{\mathbf{XX}}(r) = \sum_{k\neq 0} b^{-1} W(b^{-1}(r - \frac{2\pi k}{T}))\hat{s}_{\epsilon\epsilon}^{-1}(\frac{2\pi k}{T})\hat{\mathbf{s}}_{\mathbf{XX}}(\frac{2\pi k}{T}) \tag{6.3.2}$$

and the transfer function estimate

$$\tilde{\mathbf{H}}(r) = \tilde{\mathbf{s}}_{Y\mathbf{X}}(r)\tilde{\mathbf{s}}_{\mathbf{XX}}(r)^{-1}.$$

The difference between OLS and WLS is the weight $\hat{s}_{\epsilon\epsilon}(r)$ given by

$$\hat{s}_{\epsilon\epsilon}(r) = \frac{bT/\gamma}{bT/\gamma - n}[\hat{s}_{YY}(r) - \hat{\mathbf{s}}_{Y\mathbf{X}}(r)\hat{\mathbf{s}}_{\mathbf{XX}}(r)^{-1}\hat{\mathbf{s}}_{\mathbf{X}Y}(r)].$$

If $\mathbf{X}(t)$ has absolutely continuous spectral density and the above equation has all circumflexes removed, $\hat{s}_{\epsilon\epsilon}(r)$ is equal to $s_{\epsilon\epsilon}(r)$. If $s_{\epsilon\epsilon}(r)$ is constant, then the WLS estimator could be the same as the straight OLS estimator. As we notice, in practice $\hat{s}_{\epsilon\epsilon}(r)$ is calculated after estimating $\hat{\mathbf{H}}(r)$ by the use of OLS procedure (Hannan, 1963).

The spectrum $\hat{s}_{Y\mathbf{X}}(r)$ was defined by using periodogram $\mathbf{I}_{Y\mathbf{X}}(r)$ in frequency domain; however, it can also be defined by auto-correlation function $c_{Y\mathbf{X}}(t)$ in time domain when $E\mathbf{X}(t) = 0, EY(t) = 0$ as

$$\begin{aligned}\hat{\mathbf{s}}_{Y\mathbf{X}}(r) &= \sum_{k\neq 0} b^{-1}W(b^{-1}(r - \frac{2\pi k}{T}))\mathbf{I}_{Y\mathbf{X}}(\frac{2\pi k}{T}) \\ &= \frac{1}{2\pi}\sum_{t=-m}^{m} K(\frac{t}{m})\exp(itr)c_{Y\mathbf{X}}(t)\end{aligned}$$

where

$$c_{Y\mathbf{X}}(t) = \frac{1}{n}\sum Y_s\mathbf{X}_{s+t}^{\tau}.$$

Here $K(s)$ is a bounded, even function defined on [-1, 1] and having $K(0) = 1$. We note that if $E\mathbf{X}(t) \neq 0, EY(t) \neq 0$, only $\hat{\mathbf{s}}_{Y\mathbf{X}}(0)$ will be affected. Following Grenander and Rosenblatt (1957), we require that

$$\begin{aligned}\lim_T d_{j,T}^2 = \lim_n \sum_1^T \mathbf{X}_{j,t}^2 = \infty, &\qquad j = 1, \ldots, n; \\ \lim_T \frac{\mathbf{X}_{j,T}^2}{d_{j,T}^2} = 0, &\qquad j = 1, \ldots, n; \\ \lim_T \sum_1^{T-s} \frac{\mathbf{X}_{j,t}\mathbf{X}_{k,t+s}}{d_{j,T}d_{k,T}} = \rho_{jk}(s), &\qquad j, k = 1, \ldots, n; \\ \mathbf{R}(s) = [\rho_{j,k}(s)], &\end{aligned}$$

and we assume that $\mathbf{R}(0)$ is nonsingular. $n$ can be regarded as the number of the stimulus types. Below we discuss only the case of $n = 1$. The following derivation

can be extended to $n > 1$ after carefully defining the vector version of $\mathbf{X}$.

The diagonal matrix with $d_{j,T}$ in the $j$th place in the main diagonal we call $D_T$, that is, $D_T = \text{diag}(d_{1,T}, \ldots, d_{n,T})$. Then

$$\mathbf{R}(s) = \int_{-\pi}^{\pi} \exp(isr) d\mathbf{M}(r), \tag{6.3.3}$$

where $\mathbf{M}(r)$ is a matrix-valued function whose increments are Hermitian non-negative definite.

We hope to find an estimator of $\tilde{\mathbf{h}}(u)$ is asymptotically normal with mean at $\mathbf{h}(u)$ and covariance matrix

$$\left[\frac{1}{2\pi} d_{u,T}^2 \int s_{\epsilon\epsilon}^{-1}(r) d\mathbf{M}_{u,u}(r)\right]^{-1}. \tag{6.3.4}$$

This is a covariance matrix which corresponds to the best linear unbiased estimator (BLUE) (Grenander and Rosenblatt, 1957). $\triangle\, \mathbf{M}(r) = \mathbf{M}(r_1) - \mathbf{M}(r_2)$ is a nonnegative definite matrix for every interval $(r_1, r_2)$.

### 6.3.1 Best Linear Unbiased Estimator (BLUE)

First, we replace $\hat{s}_{\epsilon\epsilon}(r)$ with $s_{\epsilon\epsilon}(r)$ in both equation (6.3.1) and equation (6.3.2). As $s_{\epsilon\epsilon}(r)$ has absolutely convergent Fourier series, we can regard the product $W(b^{-1}(r - \frac{2\pi k}{T}))s_{\epsilon\epsilon}^{-1}(\frac{2\pi k}{T})$ in both equation (6.3.1) and equation (6.3.2) as a new weight function $W^*(b^{-1}(r - \frac{2\pi k}{T}))$. Then following the Theorems 6.1.1 - 6.1.5 in Section 6.1, we can obtain the asymptotic property of estimator $\tilde{\mathbf{h}}(u)$ defined as

$$\tilde{\mathbf{h}}(u) = \frac{1}{T} \sum_{t=0}^{T-1} \tilde{\mathbf{H}}(\frac{2\pi t}{T}) \exp(\text{i}2\pi tu/T). \tag{6.3.5}$$

$\tilde{\mathbf{h}}(u)$ is asymptotically normal with mean vector at $\mathbf{h}(u)$. Next, we need to verify that the asymptotic covariance matrix for $\tilde{\mathbf{h}}(u)$ is (6.3.4).

Since

$$\begin{aligned}\tilde{\mathbf{h}}(u) &= \frac{1}{T}\sum_{t=0}^{T-1}\tilde{\mathbf{H}}(\frac{2\pi t}{T})\exp(\mathrm{i}2\pi tu/T)\\ &= \frac{1}{T}\sum_{t=0}^{T-1}\tilde{\mathbf{s}}_{Y\mathbf{X}}(\frac{2\pi t}{T})\tilde{\mathbf{s}}_{\mathbf{XX}}(\frac{2\pi t}{T})^{-1}\exp(\mathrm{i}2\pi tu/T)\\ &= \frac{1}{T}\sum_{t=0}^{T-1}\left[\tilde{\mathbf{s}}_{R\mathbf{X}}(\frac{2\pi t}{T})+\tilde{\mathbf{s}}_{\epsilon\mathbf{X}}(\frac{2\pi t}{T})\right]\tilde{\mathbf{s}}_{\mathbf{XX}}(\frac{2\pi t}{T})^{-1}\exp(\mathrm{i}2\pi tu/T)\end{aligned}$$

for the covariance matrix, we look only at the part

$$\frac{1}{T}\sum_{t=0}^{T-1}\tilde{\mathbf{s}}_{\epsilon\mathbf{X}}(\frac{2\pi t}{T})\tilde{\mathbf{s}}_{\mathbf{XX}}(\frac{2\pi t}{T})^{-1}\exp(\mathrm{i}2\pi tu/T).$$

Above, we first show that $\tilde{\mathbf{s}}_{\mathbf{XX}}(\frac{2\pi t}{T})$ converges in probability to

$$\frac{1}{2\pi}d_{u,T}^2\int s_{\epsilon\epsilon}^{-1}(r)d\mathbf{M}_{u,u}(r).$$

We have

$$\begin{aligned}\tilde{\mathbf{s}}_{\mathbf{XX}}(\frac{2\pi t}{T}) &= \sum_{k\neq 0}b^{-1}W(b^{-1}(\frac{2\pi t}{T}-\frac{2\pi k}{T}))\hat{s}_{\epsilon\epsilon}^{-1}(\frac{2\pi k}{T})\hat{\mathbf{s}}_{\mathbf{XX}}(\frac{2\pi k}{T})\\ &= \frac{1}{2\pi}\sum_{-\infty}^{\infty}\Delta_j\sum_{k\neq 0}\exp(ij\frac{2\pi k}{T})b^{-1}W(b^{-1}(\frac{2\pi t}{T}-\frac{2\pi k}{T}))\hat{\mathbf{s}}_{\mathbf{XX}}(-\frac{2\pi k}{T})\\ &= \frac{1}{2\pi}\sum_{-\infty}^{\infty}\Delta_j\sum_{k\neq 0}\exp(ij\frac{2\pi k}{T})b^{-1}W(b^{-1}(\frac{2\pi t}{T}-\frac{2\pi k}{T}))\frac{1}{2\pi}\\ &\quad\times\sum_{-m}^{m}K(\frac{t}{m})\exp(-it\frac{2\pi k}{T})c_{Y\mathbf{X}}(t)\end{aligned}$$

where $1/2\pi\sum_{-\infty}^{\infty}\Delta_j\exp(ijr)$ is the Fourier series of $\hat{s}_{\epsilon\epsilon}^{-1}(\frac{2\pi k}{T})$, which is absolutely

convergent Fourier series. The last expression is

$$\frac{1}{2\pi}\sum_{-m}^{m}\Delta_j\frac{1}{2\pi}d_{u,T}^2\hat{\rho}_{u,u}(j)K(\frac{t}{m})$$

where $\hat{\rho}_{u,u}(j)$ is the sample serial correlations of $\mathbf{X}$. We know $\hat{\rho}_{u,u}(j)$ converges boundedly to $\rho_{u,u}(j)$ and $K(j/m)$ converges boundedly to 1, and therefore the above expression converges to

$$(\frac{1}{2\pi})^2\sum_{-\infty}^{\infty}\Delta_j\rho_{u,u}(j)=(\frac{1}{2\pi})^2\sum_{-\infty}^{\infty}\Delta_j\int\exp(ijr)d\mathbf{M}_{u,u}(r)=\frac{1}{2\pi}d_{u,T}^2\int s_{\epsilon\epsilon}^{-1}(r)d\mathbf{M}_{u,u}(r).$$

Second, we will show that $\tilde{\mathbf{s}}_{\epsilon\mathbf{X}}(\frac{2\pi t}{T})$ has asymptotic covariance matrix

$$\frac{1}{2\pi}d_{u,T}^2\int s_{\epsilon\epsilon}^{-1}(r)d\mathbf{M}_{u,u}(r).$$

From

$$\tilde{\mathbf{s}}_{\epsilon\mathbf{X}}(\frac{2\pi t}{T})=\frac{1}{2\pi}\sum_{-\infty}^{\infty}\Delta_j K(\frac{j}{m})\frac{1}{n}\sum_t\epsilon_t\mathbf{X}_{u,t+j},$$

we can see that the variance form for the above expression includes

$$E\left\{\frac{1}{n}\left[\sum_t\epsilon_t(n^{-1/2}d_{u,T})^{-1}\mathbf{X}_{u,t+j}\right]\left[\sum_t\epsilon_t(n^{-1/2}d_{u,T})^{-1}\mathbf{X}_{u,t+k}\right]^{\tau}\right\}\longrightarrow\sum_{s=-\infty}^{\infty}\Gamma_s\rho_{u,u}(s+j-k),$$

which is a bounded convergence. So the variance of $\tilde{\mathbf{s}}_{\epsilon\mathbf{X}}(\frac{2\pi t}{T})$ converges to

$$\begin{aligned}\frac{1}{4\pi^2}\sum_{j=-\infty}^{\infty}\sum_{k=-\infty}^{\infty}\Delta_j\sum_{s=-\infty}^{\infty}&d_{u,T}^2\Gamma_s\rho_{u,u}(s+j-k)\overline{\Delta_k}\\&=\frac{1}{4\pi^2}\sum_{s=-\infty}^{\infty}\left[\sum_{j=-\infty}^{\infty}\sum_{k=-\infty}^{\infty}d_{u,T}^2\Delta_j\Gamma_s\overline{\Delta_k}\rho_{u,u}(s)\right]\\&=\frac{1}{2\pi}\sum_{s=-\infty}^{\infty}\Delta_{-s}d_{u,T}^2\int\exp(isr)d\mathbf{M}_{u,u}(r)\end{aligned}$$

$$= \frac{1}{2\pi} d_{u,T}^2 \int s_{\epsilon\epsilon}^{-1}(r) d\mathbf{M}_{u,u}(r).$$

Thus, from the above derivation, $\tilde{\mathbf{h}}(u)$, by replacing $\hat{s}_{\epsilon\epsilon}$ with $s_{\epsilon\epsilon}$, is asymptotically BLUE.

### 6.3.2 Convergence in Probability

Previously we proved the asymptotic property when replacing $\hat{s}_{\epsilon\epsilon}(r)$ with $s_{\epsilon\epsilon}(r)$. Now we will show that when we replace back $\hat{s}_{\epsilon\epsilon}(r)$, the asymptotic property of $\tilde{\mathbf{h}}(u)$ is still the same.

As we know from Theorem 6.1.2, $\hat{s}_{\epsilon\epsilon}(r)$ is very close to $s_{\epsilon\epsilon}$: for any $r$,

$$E\hat{s}_{\epsilon\epsilon}(r) = s_{\epsilon\epsilon}(r) + \mathrm{O}(b^{-1}) + \mathrm{O}(bT^{-1}) + \mathrm{O}(T^{-1/2}).$$

Thus, we can say $\hat{s}_{\epsilon\epsilon}(r) - s_{\epsilon\epsilon}(r)$ converges in probability to 0:

$$\max_r \|\hat{s}_{\epsilon\epsilon}(r) - s_{\epsilon\epsilon}(r)\| \longrightarrow 0.$$

Then

$$\begin{aligned}
&\|d_{u,T}^{-2} \sum_{k\neq 0} b^{-1} W(b^{-1}(\frac{2\pi t}{T} - \frac{2\pi k}{T})) \left[\hat{s}_{\epsilon\epsilon}^{-1}(\frac{2\pi k}{T}) - s_{\epsilon\epsilon}^{-1}(\frac{2\pi k}{T})\right] \hat{\mathbf{s}}_{\mathbf{XX}}(\frac{2\pi k}{T})\|^2 \\
&\leq \sum_{k\neq 0} \|\hat{s}_{\epsilon\epsilon}^{-1}(\frac{2\pi k}{T}) - s_{\epsilon\epsilon}^{-1}(\frac{2\pi k}{T})\|^2 \sum_{k\neq 0} b^{-1} W(b^{-1}(\frac{2\pi t}{T} - \frac{2\pi k}{T})) \|d_{u,T}^{-2} \hat{\mathbf{s}}_{\mathbf{XX}}(\frac{2\pi k}{T})\|^2 \\
&\leq \sum_{k\neq 0} \|\hat{s}_{\epsilon\epsilon}^{-1}(\frac{2\pi k}{T})\|^2 \|\hat{s}_{\epsilon\epsilon}(\frac{2\pi k}{T}) - s_{\epsilon\epsilon}(\frac{2\pi k}{T})\|^2 \|s_{\epsilon\epsilon}^{-1}(\frac{2\pi k}{T})\|^2 \\
&\qquad \times \sum_{k\neq 0} b^{-1} W(b^{-1}(\frac{2\pi t}{T} - \frac{2\pi k}{T})) \|d_{u,T}^{-2} \hat{\mathbf{s}}_{\mathbf{XX}}(\frac{2\pi k}{T})\|^2
\end{aligned}$$

As $W(\cdot)$ is bounded, the summation of $\|d_{u,T}^{-2} \hat{\mathbf{s}}_{\mathbf{XX}}(\frac{2\pi k}{T})\|^2$ is also bounded. If $\|\hat{\mathbf{s}}_{\epsilon\epsilon}(r)\| \geq$

$a > 0$, then the above expression converges in probability to 0.

Similarly we can also prove that

$$\|d_{u,T}^{-2} \sum_{k \neq 0} b^{-1} W(b^{-1}(\frac{2\pi t}{T} - \frac{2\pi k}{T})) \left[ \hat{s}_{\epsilon\epsilon}^{-1}(\frac{2\pi k}{T}) - s_{\epsilon\epsilon}^{-1}(\frac{2\pi k}{T}) \right] \hat{\mathbf{s}}_{\epsilon\mathbf{X}}(\frac{2\pi k}{T})\|^2$$

converges in probability to 0.

Note that

$$\|d_{u,T}^{-1} \hat{\mathbf{s}}_{\epsilon\mathbf{X}}(\frac{2\pi k}{t})\|^2 = \sum_j K^2(\frac{j}{m}) \frac{c_{\epsilon\mathbf{X}_u}^2(j)}{c_{\mathbf{X}_u\mathbf{X}_u}}.$$

Until now, we proved that $\tilde{\mathbf{h}}(u) - \mathbf{h}(u)$ is asymptotically normal with mean zero and the covariance matrix

$$\left[ \frac{1}{2\pi} d_{u,T}^2 \int s_{\epsilon\epsilon}^{-1}(r) d\mathbf{M}_{u,u}(r) \right]^{-1}$$

which is the covariance matrix from B.L.U.E.

Thus, the WLS estimator is an asymptotically consistent and efficient estimator.

# Chapter 7

# Conclusion

In the dissertation, we proposed a nonparametric frequency-domain method, TFE, to give a consistent and efficient estimator of HRF. First, we extended Bai et al.'s method to a multivariate form in order to estimate multiple HRFs simultaneously using OLS, and we proved the consistency and asymptotic normality of the OLS estimator. Then, we improved the efficiency of OLS by using a WLS estimator in the frequency domain, and further established the consistency and efficiency of the WLS estimator. As the goal of fMRI analysis is to detect brain function, the TFE procedure provides the opportunity to test the hypothesis concerning brain activation detection and to test the validation of the linearity assumption inherited from the convolution model. Furthermore, TFE is able to compare the difference among multiple HRFs estimated simultaneously in one experimental design. For practical usage, TFE adapts to all kinds of experimental designs, and it does not depend on the pre-specified HRF length support.

There are also some developments along the application of TFE in simulations and data analyses. As we use a smoothed spectrum in TFE, we also developed a data-driven bandwidth selection method, MCV, to estimate a proper smoothing parameter for the smoothed spectrum. Second, a practical problem concerning the mismatched repetition time and acquisition time was addressed and solved by properly using TFE with interpolation.

Customized HRFs for each voxel improve activation detection in two aspects. First, it may increase detection sensitivity. In the event-related visual data from Chapter 5, we compared the brain detection results from both SPM and TFE. SPM does not detect any activation, but TFE detects activation under the Neutral and Scary stimuli, which are supposed to have an emotional effect in the amygdala. The reason SPM cannot detect activation is probably because of its incorrectly specified canonical HRF for this region. Second, customized HRFs for each voxel may reduce the detection noise. In the auditory data from Chapter 5, when we compared the activation maps from both SPM and TFE, we found that TFE captured the activation areas without giving much noise in the surrounding areas. In brief, the activation detection is more accurate considering the variation of HRFs across brain.

The estimated shape of HRF also provides some information about brain activation. First, the amplitude of the peak is an indicator of the intensity of neural activation. In our convolution model, we use the convolution of stimulus function and HRF without coefficients as the predictor of fMRI signal; in GLM, the model has coefficients to represent the intensity of activation. Thus, the peak of the estimated HRF from TFE can be used to compare the activation intensity by using the hypothesis-testing method from TFE that we developed. Second, the length of HRF also reveals how long the metabolic activity is evoked by the stimulus. In most HRF estimation methods (Goutte et al., 2000; Lindquist and Wager, 2007; Genovese, 2000; Ward and Revision, 2000; Zhang et al., 2007), the HRF length is required in order to establish the estimated number of coefficients in the model. Conveniently, we do not require the HRF length support in TFE, which is also beneficial for exploring the length of HRF. Third, depending on the temporal resolution of fMRI, the initial dip may be also captured, since our nonparametric approach does not depend on any distribution family for the estimators.

Our research to date has focused on a single voxel time series. We discussed in the dissertation how to apply TFE to a single time series, that is, a voxel-wise time series. In practice, we know that in a small ROI of the brain, HRFs share similar shape, amplitude, and timing. So if we can spot the right ROI, by averaging the time series in the ROI or weighting the HRF estimates from the voxels, we can raise SNR and increase the signal information contained in the series we analyze. Therefore, the HRF estimates might be improved. This is one example of future research in a brain region level of fMRI analysis.

Also, our research to date has focused on a single subject. We generated the activation map for a single subject and interpreted the result. Actually, most experimental designs are based on groups of subjects. For instance, there is one group of Parkinsons disease subjects, and we are interested in their common activation regions and their corresponding HRFs. Under the framework of TFE, future research can perform a second-level analysis based on the results from a single subject. Such an analysis may find the common features of the group. Another example is to compare two groups of subjects: Parkinsons Disease and Normal (Control group). Comparing groups of HRF in subjects is similar to comparing two groups of HRF curves. However, for TFE built on the frequency domain, it may be a good idea to compare the Fourier transform of HRF on a specific frequency, which simplifies the comparison from function group to point group, that is, from two dimensions to one dimension – yet another research opportunity under the TFE framework.

# Bibliography


Bai, P., Huang, X., and Truong, Y. K. (2009), "Nonparametric Estimation of Hemodynamic Response Function: A Frequency Domain Approach," in *Optimality: The Third Erich L. Lehmann Symposium*, ed. Rojo, J., Institute of Mathematical Statistics, vol. 57 of *IMS Lecture Notes Monograph Series*, pp. 190–215.

Boynton, G., Engel, S., Glover, G., and Heeger, D. (1996), "Linear Systems Analysis of Functional Magnetic Resonance Imaging in Human V1," *Journal of Neuroscience*, 16, 4207–4221.

Brillinger, D. (1981), *Time series*, Holden-Day.

Buckner, R., Bandettini, P., OCraven, K., Savoy, R., Petersen, S., Raichle, M., and Rosen, B. (1996), "Detection of cortical activation during averaged single trials of a cognitive task using functional magnetic resonance imaging," *Proceedings of the National Academy of Sciences of the United States of America*, 93, 14878–14883.

Bullmore, E., Brammer, M., Williams, S., Rabe-Hesketh, S., Janot, N., David, A., Mellers, J., Howard, R., and Sham, P. (1996), "Statistical methods of estimation and inference for functional MR image analysis," *Magnetic Resonance in Medicine*, 35, 261–276.

Casanova, R., Ryali, S., Serences, J., Yang, L., Kraft, R., Laurienti, P., and Maldjian, J. (2008), "The impact of temporal regularization on estimates of the BOLD hemodynamic response function: a comparative analysis," *NeuroImage*, 40, 1606–1618.

Cohen, M. (1997), "Parametric analysis of fMRI data using linear systems methods," *NeuroImage*, 6, 93–103.

Dale, A. and Buckner, R. (1997), "Selective averaging of rapidly presented individual trials using fMRI," *Human Brain Mapping*, 5, 329–340.

Fisher, R. et al. (1924), "On a Distribution Yielding the Error Functions of Several Well Known Statistics." *Proceedings of the International Congress of Mathematics, Toronto*, 2, 805–813.

Friston, K., Fletcher, P., Josephs, O., Holmes, A., Rugg, M., and Turner, R. (1998a), "Event-Related fMRI: Characterizing Differential Responses," *NeuroImage*, 7, 30–40.

Friston, K., Frith, C., Turner, R., and Frackowiak, R. (1995a), "Characterizing evoked hemodynamics with fMRI," *NeuroImage*, 2, 157–165.

Friston, K., Holmes, A., Worsley, K., Poline, J., Frith, C., Frackowiak, R., et al. (1995b), "Statistical parametric maps in functional imaging: a general linear approach," *Hum Brain Mapp*, 2, 189–210.

Friston, K., Jezzard, P., and Turner, R. (1994), "Analysis of functional MRI time-series," *Human Brain Mapping*, 1, 153–171.

Friston, K., Josephs, O., Rees, G., and Turner, R. (1998b), "Nonlinear event-related responses in fMRI," *Magnetic Resonance in Medicine*, 39, 41–52.

Friston, K., Penny, W., Phillips, C., Kiebel, S., Hinton, G., and Ashburner, J. (2002), "Classical and Bayesian inference in neuroimaging: theory," *NeuroImage*, 16, 465–483.

Friston, K., Worsley, K., Frackowiak, R., Mazziotta, J., and Evans, A. (1993), "Assessing the significance of focal activations using their spatial extent," *Human Brain Mapping*, 1, 210–220.

Genovese, C. (2000), "A Bayesian Time-Course Model for Functional Magnetic Resonance Imaging Data," *Journal of the American Statistical Association*, 95, 691–719.

Glover, G. (1999), "Deconvolution of Impulse Response in Event-Related BOLD fMRI1," *NeuroImage*, 9, 416–429.

Gössl, C., Fahrmeir, L., and Auer, D. (2001), "Bayesian Modeling of the Hemodynamic Response Function in BOLD fMRI," *NeuroImage*, 14, 140–148.

Goutte, C., Nielsen, F., and Hansen, K. (2000), "Modeling the hemodynamic response in fMRI using smooth FIR filters," *IEEE Transactions on Medical Imaging*, 19, 1188–1201.

Grenander, U. and Rosenblatt, M. (1957), *Statistical analysis of stationary time series*, Wiley New York.

Hannan, E. (1963), "Regression for time series," *Time series analysis*, 17–37.

Henson, R., Shallice, T., Gorno-Tempini, M., and Dolan, R. (2002), "Face repetition effects in implicit and explicit memory tests as measured by fMRI," *Cerebral Cortex*, 12, 178–186.

Huettel, S., Song, A., and McCarthy, G. (2004), *Functional magnetic resonance imaging*, Sinauer Associates Sunderland, MA.

Hykin, J., Bowtell, R., Glover, P., Coxon, R., Blumhardt, L., and Mansfield, P. (1995), "Investigation of the linearity of functional activation signal changes in the brain using echo planar imaging (EPI) at 3.0 T," in *Proceedings of the SMR and ESMRB, Joint Meeting*, p. 795.

Jacobs, J., Hawco, C., Kobayashi, E., Boor, R., LeVan, P., Stephani, U., Siniatchkin, M., and Gotman, J. (2008), "Variability of the hemodynamic response as a function of age and frequency of epileptic discharge in children with epilepsy," *NeuroImage*, 40, 601–614.

Josephs, O., Turner, R., and Friston, K. (1997), "Event-Related fMRI," *Human Brain Mapping*, 5, 243–248.

Kruggel, F. and von Cramon, D. (1999), "Modeling the hemodynamic response in single-trial functional MRI experiments," *Magnetic Resonance in Medicine*, 42, 787–797.

Lange, N. and Zeger, S. (1997), "Non-linear Fourier Time Series Analysis for Human Brain Mapping by Functional Magnetic Resonance Imaging," *Journal of the Royal Statistical Society: Series C (Applied Statistics)*, 46, 1–29.

Lewis, M., Slagle, C., Smith, A., Truong, Y., Bai, P., McKeown, M., Mailman, R., Belger, A., and Huang, X. (2007), "Task specific influences of Parkinson's disease on the striato-thalamo-cortical and cerebello-thalamo-cortical motor circuitries," *Neuroscience*, 147, 224–235.

Lindquist, M. (2008), "The statistical analysis of fmri data," *Statistical Science*, 23, 439–464.

Lindquist, M., Meng Loh, J., Atlas, L., and Wager, T. (2009), "Modeling the hemodynamic response function in fmri: Efficiency, bias and mis-modeling," *NeuroImage*, 45, 187–198.

Lindquist, M. and Wager, T. (2007), "Validity and power in hemodynamic response modeling: A comparison study and a new approach," *Human Brain Mapping*, 28, 764–784.

Lu, Y., Bagshaw, A., Grova, C., Kobayashi, E., Dubeau, F., and Gotman, J. (2006), "Using voxel-specific hemodynamic response function in EEG-fMRI data analysis," *NeuroImage*, 32, 238–247.

Lu, Y., Grova, C., Kobayashi, E., Dubeau, F., and Gotman, J. (2007), "Using voxel-specific hemodynamic response function in EEG-fMRI data analysis: An estimation and detection model," *NeuroImage*, 34, 195–203.

Makni, S., Beckmann, C., Smith, S., and Woolrich, M. (2008), "Bayesian deconvolution fMRI data using bilinear dynamical systems," *NeuroImage*, 42, 1381–1396.

Marchini, J. and Ripley, B. (2000), "A New Statistical Approach to Detecting Significant Activation in Functional MRI," *NeuroImage*, 12, 366–380.

Mitra, P., Ogawa, S., Hu, X., and Ugurbil, K. (1997), "The nature of spatiotemporal changes in cerebral hemodynamics as manifested in functional magnetic resonance imaging," *Magnetic Resonance in Medicine*, 37, 511–518.

Mumford, J. and Nichols, T. (2006), "Modeling and inference of multisubject fMRI data," *IEEE Engineering in Medicine and Biology Magazine*, 25, 42–51.

Rajapakse, J., Kruggel, F., Maisog, J., and Von Cramon, D. (1998), "Modeling hemodynamic response for analysis of functional MRI time-series," *Human Brain Mapping*, 6, 283–300.

Richter, W., Ugurbil, K., Georgopoulos, A., and Kim, S. (1997), "Time-resolved fMRI of mental rotation," *NeuroReport*, 8, 3697–3702.

Rosenblatt, M. (1959), *Statistical analysis of stochastic processes with stationary residuals*, Wiley, New York.

Smith, S., Jenkinson, M., Woolrich, M., Beckmann, C., Behrens, T., Johansen-Berg, H., Bannister, P., De Luca, M., Drobnjak, I., Flitney, D., et al. (2004), "Advances in functional and structural MR image analysis and implementation as FSL," *NeuroImage*, 23, 208–219.

Steffener, J., Tabert, M., and Stern, Y. (2009), "Investigating Hemodynamic Response Variability at the Group Level using Basis Functions," *NeuroImage*, 47, 56–56.

Vazquez, A. and Noll, D. (1998), "Nonlinear aspects of the BOLD response in functional MRI," *NeuroImage*, 7, 108–118.

Ward, B. and Revision, L. (2000), "Deconvolution analysis of fMRI time series data," *AFNI 3dDeconvolve Documentation, Medical College of Wisconsin*.

Wink, A., Hoogduin, H., and Roerdink, J. (2008), "Data-driven haemodynamic response function extraction using Fourier-wavelet regularised deconvolution," *BMC Medical Imaging*, 8, 7.

Woolrich, M., Jbabdi, S., Patenaude, B., Chappell, M., Makni, S., Behrens, T., Beckmann, C., Jenkinson, M., and Smith, S. (2009), "Bayesian analysis of neuroimaging data in FSL," *NeuroImage*, 45, 173–186.

Woolrich, M., Jenkinson, M., Brady, J., and Smith, S. (2004), "Fully Bayesian spatiotemporal modeling of fMRI data," *IEEE Transactions on Medical Imaging*, 23, 213–231.

Zarahn, E. (2000), "Testing for neural responses during temporal components of trials with BOLD fMRI," *NeuroImage*, 11, 783–796.

Zhang, C., Jiang, Y., and Yu, T. (2007), "A comparative study of one-level and two-level semiparametric estimation of hemodynamic response function for fMRI data," *Statistics in Medicine*, 26, 3845–3861.

Zhang, C., Lu, Y., Johnstone, T., Oakes, T., and Davidson, R. (2008), "Efficient modeling and inference for event-related fMRI data," *Computational Statistics & Data Analysis*, 52, 4859–4871.